

ABSTRACT

KENNEDY, EMESE AGNES. Swing-up and Stabilization of a Single Inverted Pendulum: Real-Time Implementation. (Under the direction of Hien Tran.)

The single inverted pendulum (SIP) system is a classic example of a nonlinear under-actuated system. Despite its simple structure, it is among the most difficult systems to control and is considered as one of the most popular benchmarks of nonlinear control theory. In the past fifty years many nonlinear methods have been proposed for the swing-up and stabilization of a self-erecting inverted pendulum, however, most of these techniques are too complex and impractical for real-time implementation.

In the first part of this dissertation, the successful real-time implementation of a nonlinear controller for the stabilization of the pendulum is discussed. The controller is based on the power series approximation to the Hamilton Jacobi Bellman (HJB) equation. The derivation of the controller is based on work that can be found in the literature, but the controller has not been used for the stabilization of an inverted pendulum before. It performs similarly to the traditional linear quadratic regulator (LQR), but has some important advantages. First, the method can stabilize the pendulum for a wider range of initial starting angle. Additionally, it can also be used with state dependent weighting matrices, Q and R , whereas the LQR problem can only handle constant values for these matrices. The use of state-dependent weighting matrices for the stabilization of an inverted pendulum in real-time has been discussed in the literature before, but only with controls that use a State Dependent Riccati Equation (SDRE) approach. The benefit of the control presented in this thesis over the SDRE controls is that it is computationally less intense and does not require the solution of complicated matrix equations at every time step. However, the control method presented cannot be used to swing-up the pendulum whereas some of the controls using the online solution of the SDRE can.

The second part of the dissertation focuses on the swing-up of the inverted pendulum. The most common and efficient method for the swing-up of the pendulum uses an energy based approach. This method was originally proposed by Astrom and Furuta in 1996, and it was first implemented for the swing-up of a rotary pendulum in 1999. Later, the controller was modified and implemented on a cart pendulum system taking the finite length of the track into account. However, most of the existing swing-up controllers are based on a simplified model for the SIP system, and the effects of friction are frequently disregarded. In this thesis, we present a new energy-based swing-up controller that was derived using a more complex dynamical model for the SIP system. We also consider the effects of viscous damping, and incorporate physical restrictions like the maximum deliverable voltage by the amplifier, the capacity of the DC motor that drives the cart, and the finite track length.

© Copyright 2015 by Emese Agnes Kennedy

All Rights Reserved

Swing-up and Stabilization of a Single Inverted Pendulum: Real-Time Implementation

by
Emese Agnes Kennedy

A dissertation submitted to the Graduate Faculty of
North Carolina State University
in partial fulfillment of the
requirements for the Degree of
Doctor of Philosophy

Applied Mathematics

Raleigh, North Carolina

2015

APPROVED BY:

Stephen Campbell

Ralph Smith

Kazufumi Ito

Hien Tran
Chair of Advisory Committee

DEDICATION

To my friends and family who helped me persevere.

BIOGRAPHY

The author was born in Budapest, Hungary, and lived in Thailand for three years where she completed high school at the International School of Bangkok. She graduated summa cum laude with Honors in Mathematics from Skidmore College in Saratoga Springs, NY, with a dual degree in Mathematics and Dance, and a minor in Computer Science. Thanks to the influence of great teachers and mentors she became interested in studying mathematics, particularly after one of her professors, Dr. Rachel Roe-Dale, asked her to participate in an undergraduate summer research program.

After finishing college, the author moved to Raleigh, NC to pursue a doctorate in Applied Mathematics at North Carolina State University. She received a MS degree in Applied Mathematics from NC State in 2013. Thanks to working with Dr. Ralph Smith during her first year of graduate school, the author was hired as the lab technician for the Center for Research in Scientific Computation (CRSC) at NC State. The position helped her gain valuable hands-on experience with real-time mathematical models used during several physical and biological experiments. Some of these included horizontal and vertical vibrating beams, heat transfer, real-time blood pressure monitoring, and traveling waves. More importantly, this position allowed her the possibility of completing dissertation work with Dr. Hien Tran on the inverted pendulum.

While she enjoys working on real life mathematical applications, the author has a passion for teaching. She has taught several undergraduate mathematics classes during her graduate years, and has received two teaching awards from the University Graduate Student Association at NC State. In addition, she has completed the Certificate of Accomplishment in Teaching program. Thanks to Dr. Alina Duca, Emese became involved with teaching Calculus for Elementary Education, an inquiry based learning course developed with NSF support specifically for pre-service elementary teachers. She has also had the opportunity to regularly assist a research team led by Dr. Karen Keene in the Mathematics Education Department, which studies the mathematical sophistication of undergraduate students, and works on developing better ways students can be supported as they study mathematical concepts.

Emese has accepted a Visiting Assistant Professor position at Muhlenberg College in Allentown, PA. She hopes to continue teaching while also exploring more real-life applications of mathematics.

ACKNOWLEDGEMENTS

I would first like to thank my advisor, Dr. Hien Tran for believing in me and helping me achieve my goals. He has always been very supportive of me and allowed me to pursue my passion for teaching on top of my research. I would like to thank my committee members: Dr. Stephen Campbell, who has provided me with support and guidance since my first day at NC State; Dr. Ralph Smith, who has had a great influence on my graduate career since my first year, and who gave me the opportunity to work for the CRSC and connected me with Dr. Tran; and Dr. Kazufumi Ito, who agreed to serve on my committee and give me advice even before getting to know me.

I would like to thank Dr. Alina Duca and Dr. Karen Keene for letting me get involved with CELTIC, and for being wonderful mentors who truly helped me become a better teacher.

I wouldn't have made it to graduate school without the great support and preparation I received from the math professors at Skidmore, who have become like a second family to me. I would especially like to thank Dr. Rachel Roe-Dale who pushed me to pursue a doctorate in applied math, and who has been an amazing teacher, mentor, and friend. Dr. David Vella also deserves special thanks for all his support and for being the first person who allowed me to teach a math class.

I would like to thank my friends and family for supporting me throughout my graduate journey, and for helping me get through some really difficult times.

I would like to thank my wife, Katie, for all her support and encouragement, and for keeping me sane and helping me survive.

Finally, I would like to thank the Mathematics Department and the Center for Research in Scientific Computation at NC State for financially supporting my graduate career.

TABLE OF CONTENTS

LIST OF TABLES	vii
LIST OF FIGURES	viii
Chapter 1 Introduction	1
1.1 Applications	2
1.2 Review of Existing Control Methods	2
1.3 Dissertation Outline	5
Chapter 2 System Dynamics	6
2.1 System Representation and Notations	6
2.2 Equations of Motion	7
2.2.1 Lagrange's Method	7
2.2.1.1 Potential Energy	7
2.2.1.2 Kinetic Energy	7
2.2.1.3 Lagrange's Equations	9
2.2.2 Converting to Voltage Input	10
2.3 Model Calibration	12
Chapter 3 Stabilization Control	14
3.1 Problem Statement	14
3.2 Power Series Based Controller	15
3.2.1 Power Series Approximation	16
3.2.2 Constant Matrix B	19
3.2.2.1 Simulation Results: Constant B vs. State-Dependent B	19
3.2.3 Incorporation of a State-Dependent Weighting Matrix	20
3.3 Stability Analysis	22
3.4 Real-Time Implementation	28
3.4.1 Apparatus	28
3.4.2 Design Specifications	28
3.5 Experimental Results	29
3.5.1 Constant Weighting Matrices	29
3.5.2 State-Dependent Weighting Matrix	39
3.5.3 Disturbance Rejection	42
Chapter 4 Swing-up Control	48
4.1 Energy-based Controller	48
4.1.1 Pendulum's Energy	48
4.1.2 Converting to Voltage Input	49
4.1.3 Lyapunov Stability Condition	50
4.1.4 Simulation Results	52
4.1.5 Experimental Results	53
4.2 More Robust Swing-up Controller	56

4.2.1	Modified Lyapunov Function	56
4.2.2	Simulation Results	58
4.3	Incorporating Viscous Damping at the Pendulum Axis	61
4.4	Simulation Results	63
4.5	Experimental Results	63
4.6	Summary of Swing-up Controllers	64
Chapter 5	Closing Remarks	67
5.1	General Conclusion	67
5.2	Future Work	67
REFERENCES	69
APPENDICES	76
Appendix A	Model Parameters	77
A.1	Nomenclature	77
A.2	Model Parameter Values	80
Appendix B	MATLAB Code	81
B.1	Code to Setup Parameters for the Simulink Diagrams	81
B.2	Simulink Diagrams for Model Calibration	86
B.3	Simulink Diagrams for Stabilization Simulation	90
B.4	Simulink Diagrams and Code for Stabilizing Control	92
B.5	Simulink Diagrams for Swing-up Control	94

LIST OF TABLES

Table 3.1	Summary of stabilization state response with different weighting matrices.	31
Table 3.2	Summary of control effort with different weighting matrices.	31
Table 3.3	Summary of stabilization state response and control effort for the power series based controller with state-dependent Q vs. controllers with $Q = \text{diag}(800, 150, 1, 1)$	40
Table 3.4	Summary of stabilization state response and control effort with 1.5° pulse disturbance.	42

LIST OF FIGURES

Figure 1.1	Inverted pendulum like systems.	2
Figure 2.1	Diagram of the SIP mounted on a cart.	6
Figure 2.2	DC Motor Electric Circuit	11
Figure 2.3	Comparison of real-time data with simulated model response with and without friction.	13
Figure 3.1	Stabilization controller with state-dependent B given by (3.24) versus controller with constant B given by (3.32)	21
Figure 3.2	Stabilization simulation results for the power series based controller with various initial angles, and $x_0 = 0, \dot{\alpha}_0 = 0, \dot{x}_0 = 0$	23
Figure 3.3	Stabilization simulation results for the LQR controller with various initial angles, and $x_0 = 0, \dot{\alpha}_0 = 0, \dot{x}_0 = 0$	24
Figure 3.4	Stability region estimate for both the power series based controller and the LQR controller for various initial pendulum angles and angular velocities with zero initial cart position and cart velocity.	25
Figure 3.5	Stability region estimate for both the power series based controller and the LQR controller for various initial pendulum angles and cart positions with zero initial cart velocity and angular velocity.	25
Figure 3.6	Stability region estimate for both the power series based controller and the LQR controller for various initial cart positions and cart velocities with zero initial pendulum angle and angular velocity.	26
Figure 3.7	Stability region estimate for the power series based controller for various initial pendulum angles, angular velocities, and cart velocities with zero initial cart position.	26
Figure 3.8	Stability region estimate for the LQR controller for various initial pendulum angles, angular velocities, and cart velocities with zero initial cart position.	27
Figure 3.9	Stability region estimate for the power series based controller for various initial cart positions, pendulum angles, and angular velocities with zero initial cart velocity.	27
Figure 3.10	Stability region estimate for the LQR controller for various initial cart positions, pendulum angles, and angular velocities with zero initial cart velocity.	28
Figure 3.11	Single inverted pendulum mounted on a Quanser IP02 servo plant.	29
Figure 3.12	Diagram of experimental setup.	29
Figure 3.13	Cart position with power series based controller vs. LQR: $Q = \text{diag}(0.75, 4, 0, 0)$ and $R = 0.0003$	32
Figure 3.14	Pendulum's angle with power series based controller vs. LQR: $Q = \text{diag}(0.75, 4, 0, 0)$ and $R = 0.0003$	32
Figure 3.15	Cart velocity with power series based controller vs. LQR: $Q = \text{diag}(0.75, 4, 0, 0)$ and $R = 0.0003$	33

Figure 3.16	Pendulum's angular velocity with power series based controller vs. LQR: $Q = \text{diag}(0.75, 4, 0, 0)$ and $R = 0.0003$	33
Figure 3.17	Control effort with power series based controller vs. LQR: $Q = \text{diag}(0.75, 4, 0, 0)$ and $R = 0.0003$	34
Figure 3.18	Cart position with power series based controller vs. LQR: $Q = \text{diag}(5, 50, 0, 0)$ and $R = 0.002$	34
Figure 3.19	Pendulum's angle with power series based controller vs. LQR: $Q = \text{diag}(5, 50, 0, 0)$ and $R = 0.002$	35
Figure 3.20	Cart velocity with power series based controller vs. LQR: $Q = \text{diag}(5, 50, 0, 0)$ and $R = 0.002$	35
Figure 3.21	Pendulum's angular velocity with power series based controller vs. LQR: $Q = \text{diag}(5, 50, 0, 0)$ and $R = 0.002$	36
Figure 3.22	Control effort with power series based controller vs. LQR: $Q = \text{diag}(5, 50, 0, 0)$ and $R = 0.002$	36
Figure 3.23	Cart position with power series based controller vs. LQR: $Q = \text{diag}(800, 150, 1, 1)$ and $R = 0.1$	37
Figure 3.24	Pendulum's angle with power series based controller vs. LQR: $Q = \text{diag}(800, 150, 1, 1)$ and $R = 0.1$	37
Figure 3.25	Cart velocity with power series based controller vs. LQR: $Q = \text{diag}(800, 150, 1, 1)$ and $R = 0.1$	38
Figure 3.26	Pendulum's angular velocity with power series based controller vs. LQR: $Q = \text{diag}(800, 150, 1, 1)$ and $R = 0.1$	38
Figure 3.27	Control effort with power series based controller vs. LQR: $Q = \text{diag}(800, 150, 1, 1)$ and $R = 0.1$	39
Figure 3.28	Control Effort with power series based controller: $Q = \text{diag}(800 + 5x^2, 150 + 2\alpha^2, 1 + \dot{x}^2, 1 + \dot{\alpha}^2)$ and $R = 0.1$ $ V_m < 1.82$ Volts, $ V_m _{\text{avg}} = 0.358$ Volts, $\int_0^{30} V_m dt = 10.73$	40
Figure 3.29	State response with power series based controller: $Q = \text{diag}(800 + 5x^2, 150 + 2\alpha^2, 1 + \dot{x}^2, 1 + \dot{\alpha}^2)$ and $R = 0.1$	41
Figure 3.30	Cart position response to 1.5° disturbance.	43
Figure 3.31	Pendulum's angle response to 1.5° disturbance.	44
Figure 3.32	Cart velocity response to 1.5° disturbance.	45
Figure 3.33	Pendulum angular velocity response to 1.5° disturbance.	46
Figure 3.34	Control effort with 1.5° disturbance.	47
Figure 4.1	Diagram representing how $\text{sg}(X)$ is defined. The arrows indicate the direction of the cart's displacement, while the number line indicates the cart's position.	51
Figure 4.2	Simulated state response and control effort for the energy based swing up controller given by equation (4.17) with $\beta = 4$ and $\eta = 0.9$	54
Figure 4.3	Experimental state response and control effort for the energy based swing up controller given in equation (4.17) with $\beta = 4$ and $\eta = 0.9$	55
Figure 4.4	Simulated state response and control effort for the more robust swing up controller given by equation (4.28).	60

Figure 4.5	Simulated state response and control effort for the more robust swing up controller including viscous damping at the pendulum axis.	65
Figure 4.6	Experimental state response and control effort for the energy based swing up controller given in equation (4.42) with $\beta_1 = 4.8$, $\beta_2 = 0.6$, $\beta_3 = 0.0115$, and $\eta = 0.6$	66
Figure B.1	Main Simulink diagram used for model calibration. The SIP + IP02: Actual Plant block that communicates with the apparatus and captures the value of the states in real-time was provided by Quanser. The SIP EOM with Friction subsystem computes the simulated state response based on the nonlinear equations of motion with friction given by equations (2.33) and (2.34). The details of the subsystem are given in Figures B.2-B.4. The SIP EOM with No Friction subsystem is the same as the subsystem with friction, but the friction coefficients are ignored (i.e. $B_{eq} = 0$ and $B_p = 0$).	86
Figure B.2	SIP EOM Simulink subsystem used in the Simulink diagram given in B.1.	87
Figure B.3	x_ddot EOM subsystem used in the Simulink diagram given in B.2.	88
Figure B.4	α_ddot EOM subsystem used in the Simulink diagram given in B.3.	89
Figure B.5	Main Simulink diagram used for stabilization simulation to compare the performance of the control laws given by (3.24) and (3.32). The stabilizing control is computed inside a Matlab function with the command $-inv(R) * BX(u(1), u(2), u(3), u(4))' * (P * u + inv(A0' - P * B * inv(R) * B') * (0.5 * P * B2(u(1), u(2), u(3), u(4)) * inv(R) * B' * P * u + 0.5 * P * B * inv(R) * B2(u(1), u(2), u(3), u(4))' * P * u - P * f3(u(1), u(2), u(3), u(4))))$ (state-dependent B) or $-inv(R) * B' * P * u + inv(R) * B' * inv(A0' - P * B * inv(R) * B') * P * f3(u(1), u(2), u(3), u(4))$ (constant B). The input, u , for the block is the state vector, X . The SIP EOM with Friction subsystem computes the simulated state response based on the nonlinear equations of motion with friction given by equations (2.33) and (2.34). The details of the subsystem are given in Figures B.2-B.4	90
Figure B.6	Main Simulink diagram used for stabilization simulation. The stabilizing control is computed inside a Matlab function with the command $-inv(R) * B' * P * u + inv(R) * B' * inv(A0' - P * B * inv(R) * B') * P * f3(u(1), u(2), u(3), u(4))$ (constant Q) or $-inv(R) * B0' * P * u + inv(R) * B' * inv(A0' - P * B * inv(R) * B') * (P * f3(u(1), u(2), u(3), u(4)) + 0.5 * [5 * u(1)^2, 0, 0, 0; 0, 2 * u(2)^2, 0, 0; 0, 0, u(3)^2, 0; 0, 0, 0, u(4)^2] * u)$ (state-dependent Q). The input, u , for the block is the state vector, X . The SIP EOM with Friction subsystem computes the simulated state response based on the nonlinear equations of motion with friction given by equations (2.33) and (2.34). The details of the subsystem are given in Figures B.2-B.4	91
Figure B.7	Main Simulink diagram to run real-time stabilization. The SIP + IP02: Actual Plant block that communicates with the apparatus was provided by Quanser. The stabilizing control is computed inside an Embedded Matlab function block. The code inside the block is provided in Figures B.8 (constant Q) and B.9 (state-dependent Q).	92

Figure B.8	Code inside Embedded Matlab function block in the Simulink diagram to compute stabilizing control with constant Q based on power series expansion.	92
Figure B.9	Code inside Embedded Matlab function block in the Simulink diagram to compute stabilizing control with state-dependent Q based on power series expansion.	93
Figure B.10	Scopes subsystem to record and plot states.	93
Figure B.11	Main Simulink diagram to run real-time swing-up. The SIP + IP02: Actual Plant block that communicates with the apparatus was provided by Quanser. The Mode Switching Strategy block that checks the angle of the pendulum and switches from the swing-up controller to the stabilizing controller, was also provided by Quanser. The details of the Swing-up Control subsystem block are given in Figure B.12 for the controller in (4.17), Figure B.15 for the controller in (4.28), and Figure B.16 for the controller in (4.42)	94
Figure B.12	Simulink subsystem used to compute energy based swing-up controller in (4.17). The details of the Compute sg subsystem block are given in Figure B.13, and the details of the Pendulum Energy subsystem block are given in Figure B.14.	95
Figure B.13	Simulink subsystem that computes sg.	96
Figure B.14	Simulink subsystem that computes the pendulum's energy.	96
Figure B.15	Simulink subsystem used to compute more robust swing-up controller in (4.28). The details of the Compute sg subsystem block are given in Figure B.13, and the details of the Pendulum Energy subsystem block are given in Figure B.14.	97
Figure B.16	Simulink subsystem used to compute swing-up controller with viscous damping term in (4.42). The details of the Compute sg subsystem block are given in Figure B.13, and the details of the Pendulum Energy subsystem block are given in Figure B.14.	98

Chapter 1

Introduction

At some point in our lives almost all of us have attempted to balance a broomstick on the palm of our hand, or seen someone try to. The broomstick can be thought of as an inverted pendulum with the difference being that the broomstick is free to move in a three-dimensional space while a pendulum, in this study, is mounted on a cart and can only move in a linear plane. Just like the broomstick, an inverted pendulum is a highly unstable system. Force and proper control must be appropriately applied to keep the pendulum balanced and upright.

In 1990 the International Federation of Automatic Control (IFAC) Theory Committee published a set of real world control problems that can be used to compare the benefits of new and existing control methods, called benchmark problems. One of these is the control of an inverted pendulum [23]. Despite its simple structure, the inverted pendulum is among the most difficult systems to control. This difficulty arises because the equations of motion governing the system are inherently nonlinear and because the upright position is an unstable equilibrium. Furthermore, the system is under-actuated as it has two degrees of freedom, one for the cart's horizontal motion and one for the pendulum's angular motion, but only the cart's position is actuated, while the pendulum's angular motion is indirectly controlled.

In a laboratory setting, there are two main types of Single Inverted Pendulum (SIP) systems: the rotary pendulum system, and the pendulum on a cart system. The controllers for these two systems are similar, but they have different actuator dynamics. The largest difference between the two systems is that the pendulum on a cart system has a finite track length that needs to be taken into account, especially during swing-up. This dissertation only focuses on the controllers for a cart pendulum system.

The SIP control problem is composed of two tasks: the first task is to swing-up the pendulum from its downward hanging position, and the second task is to stabilize the pendulum around the vertical upright position. These two tasks are usually accomplished using two separate controllers, however, there are a few existing control methodologies that can handle both tasks

without having to switch controllers [15]. The control methods presented in this dissertation accomplish the two tasks separately.

1.1 Applications

As its shape and dynamics resemble many different real world systems, the inverted pendulum has numerous applications. One of the earliest uses of an inverted pendulum was in 1844 by James Forbes in the design of a seismometer. Forbes used the fact that the upright equilibrium of the pendulum is unstable and thus very sensitive to disturbances [24]. Some other applications of the inverted pendulum include the stabilization of ships and rockets, the design of earthquake resistant buildings, and robotic arms. The inverted pendulum is also considered as an adequate model of a human standing still [76]. Figure 1.1 gives an illustration of some inverted pendulum like systems.

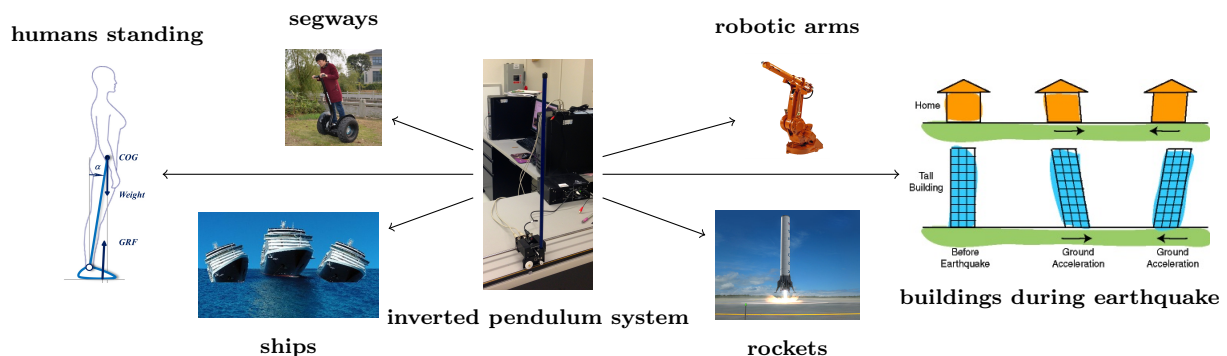


Figure 1.1: Inverted pendulum like systems.

1.2 Review of Existing Control Methods

Because of its popularity and numerous applications, there are many existing control methods for the inverted pendulum. However, many of the published controllers have only been tested in simulations and not in real-time experiments. Comparing experimental results with published work of others, the simulation results are often different from the real-time results. This is because almost all simulations use a simplified model to represent the dynamics of the inverted pendulum. Furthermore, most of the simulations ignore the effects of friction, and often fail to incorporate some physical restrictions like the maximum deliverable voltage by the amplifier, the capacity of the DC motor that drives the cart, and the finite track length.

Below is a summary of the most popular control methods that have been implemented for an inverted pendulum, and a short discussion of the advantages and disadvantages of each method. Most of the cited references were compiled based on an extensive survey by Boubaker [15].

Fuzzy Logic and Neural Network Controllers are discussed in references [2, 78, 80]. These controllers have a simple structure and don't require lengthy computations. They are very popular methods for both the swing-up and the stabilization of the pendulum, however, the presentation of these methods often lack the specification of the stability conditions.

Proportional-Integral-Derivative (PID) Adaptive Control is discussed in references [10, 19, 56]. This method is good for stabilizing the pendulum, but requires frequent tuning. Chang et al. discusses the implementation of a self-tuning PID controller using a Lyapunov approach in [19], but only simulation results are presented without discussion of real-time experiments.

Energy-Based Control is one of the most popular and efficient methods for swinging-up the pendulum. The global stability conditions of this approach are well proven using Lyapunov techniques. An energy based method was originally proposed by Astrom and Furuta in 1996 at the 13th IFAC World Congress [8]. Their revised paper that included the implementation of their method on a rotary pendulum was published in 2000 [9]. Later, the method was adapted for a cart-pendulum system by Angeli in [3], but without taking the finite length of the track into account. References [21, 49, 73, 83] also discuss the use of energy based controllers for the pendulum on a cart system. Control methods that consider the length of the track are presented in [20, 37].

Hybrid Control methods based on the energy approach that accomplish both the swing-up and the stabilization of the pendulum without switching controllers are presented in [4, 7, 6, 30, 74].

Sliding Mode Control is a powerful and robust control method that can be used for many practical systems that are not under actuated. In [71] a modified Van der Pol oscillator is implemented for both the swing-up and the stabilization of the pendulum, but with some performance issues. Namely, the fast switching in the implemented controller causes undesirable chattering. In [60] an aggressive sliding mode control law is presented for both the swing-up and the stabilization along with results of numerical simulations for the cart pendulum system, and real-time experimental results for the rotary pendulum system.

Linear Quadratic Regulator (LQR) is simple and easy to implement control method that performs reasonably well for stabilizing the inverted pendulum. However, the performance of the method greatly depends on the selection of the weighting matrices, Q and R , in

the cost functional. In a recent publication, Trimpe et al. proposed a self-tuning LQR approach using stochastic optimization, but the method has only been implemented in simulations and not in real-time experiments [77].

Linear Quadratic Gaussian (LQG) is a controller that combines LQR with a Kalman Filter to improve disturbance rejection. This method was implemented by Eide et al. in [25] during the balance of an inverted pendulum mobile robot, however, they found that the LQR produced better response when compared to the LQG approach.

Approximate Linearization is a method of finding a nonlinear change of coordinates for a nonlinear system to construct a linear approximation of the plant dynamics accurate to second or higher order. Starting with the work of Krener [41, 42, 43], many variants of this approach have been suggested [38, 40]. The algorithm presented in [41] was implemented for the stabilization of a rotary pendulum by Sugie and Fujimoto [75]. They showed through experiments that the method enlarges the stability region. Using the ideas in [42] and [40], Ohsumi and Izumikawa implemented in real-time a control method that can be used for both the swing-up and stabilization of an inverted pendulum on a cart [57]. Based on Krener’s approach, Guzzella and Isidori developed a simpler and more direct method to calculate the quantities involved [31]. This algorithm was implemented for the stabilization of a cart-pendulum system by Renou and Saydy [69]. Their simulation and experimental results show a slight improvement in the system’s transient response, but a reduced region of stability when compared to the LQR control method. In [39], Ingram et al. present the successful real-time implementation of a modified approach using an algorithm designed for feedback linearizable systems. Their technique works for both the swing-up and stabilization of an inverted pendulum on a cart. They consider both the finite track length, and the restriction on the maximum voltage input, but they do not take the effects of friction into account.

State-Dependent Riccati Equation (SDRE) based controller has been used for the stabilization of the pendulum in simulations in [37, 72]. In [22], Dang and Lewis present the successful real-time implementation of a SDRE based controller for both the swing-up and the stabilization. The drawback of this method is that it is computationally very intense as it requires the solution of complicated state-dependent Riccati equations at every time step.

Most of the control methods discussed above ignore the effects of friction. There is a limited number of publications that consider friction in the development of the model for the inverted pendulum. Campbell et al. have studied the use of different friction models during real-time

implementation for the stabilization of the pendulum [18, 17]. They have also showed that disregarding friction produces oscillatory behavior during stabilization.

1.3 Dissertation Outline

In the past sixty years many nonlinear methods have been proposed for the swing-up and stabilization of a single inverted pendulum, however, many of these techniques are too complex and impractical for real-time implementation [15]. This dissertation focuses on the real-time implementation of practical control methods for both the swing-up and the stabilization of an inverted pendulum.

In Chapter 2, the dynamics of the inverted pendulum system are discussed, including modeling conventions and the derivation of the nonlinear equations of motion.

Chapter 3 focuses on the adaptation of a power series approximation based control method for the stabilization of the pendulum. This control method was first proposed by Garrard in [26, 27, 28], but it has not been implemented for an inverted pendulum before. The controller performs similarly to the traditional linear quadratic regulator, but has some important advantages. One of the advantages is that the method can stabilize the pendulum for a wider range of initial starting angle. It can also be used with state dependent weighting matrices whereas the LQR problem can only handle constant values for Q and R . The use of a state-dependent matrix, Q , is also discussed in this chapter. We present both simulation and real-time experimental results implemented in MATLAB Simulink.

In Chapter 4, we use the technique originally proposed by Astrom and Furuta [8, 9] to derive a modified energy based swing-up controller using Lyapunov functions. During the derivation, all effort has been made to use a more complex dynamical model for the SIP system than the simplified model that is most commonly used. We consider the electrodynamics of the DC motor that drives the cart, and incorporate viscous damping friction as seen at the motor pinion. Furthermore, we use a new method to account for the limitation of having a cart-pendulum system with a finite track length. Two modifications to the controller are also discussed to make the method more appropriate for real-time implementation. One of the modifications improves robustness using a modified Lyapunov function for the derivation, while the other one incorporates viscous damping as seen at the pendulum axis. We present both simulation and real-time experimental results implemented in MATLAB Simulink.

Finally, Chapter 5 provides some concluding remarks and ideas for future work.

Chapter 2

System Dynamics

2.1 System Representation and Notations

Figure 2.1 shows a diagram of the Single Inverted Pendulum (SIP) mounted on a cart. The nomenclature corresponding to the system is given in Appendix A.1. The positive sense of rotation is defined to be counterclockwise, when facing the cart. The perfectly vertical upward pointing position of the inverted pendulum corresponds to the zero angle. The positive direction of the cart's displacement is to the right when facing the cart, as indicated by the Cartesian frame of coordinates presented in Figure 2.1.

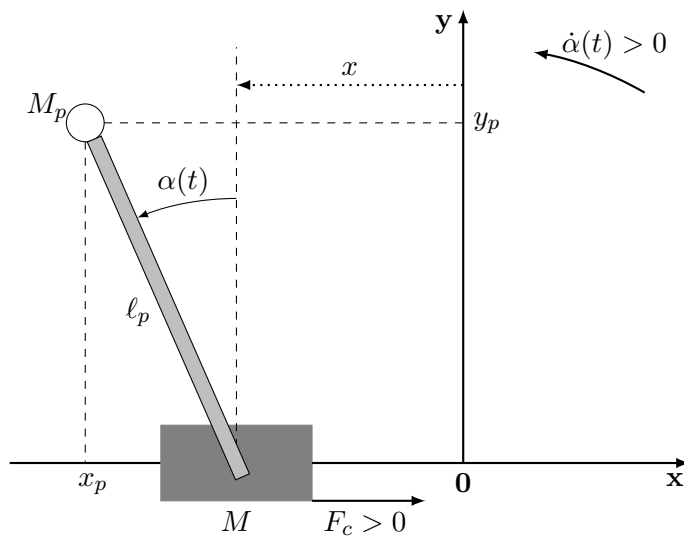


Figure 2.1: Diagram of the SIP mounted on a cart.

2.2 Equations of Motion

2.2.1 Lagrange's Method

We will use Lagrange's energy method to derive the dynamic model of the system. In this approach, we consider the driving force, F_c , generated by the DC motor acting on the cart through the motor pinion as the single input. To carry out Lagrange's method, first we need to determine the Lagrangian of the system through the calculation of the system's total potential and kinetic energies.

2.2.1.1 Potential Energy

The total potential energy, \mathcal{V}_T , in a system is given by the amount of energy that the system has due to some kind of work being, or having been, done to it. It is usually caused by its vertical displacement (gravitational potential energy) from normality or by a spring-related sort of displacement (elastic potential energy). For the SIP system, the potential energy is only due to gravity. Since the cart's linear motion is horizontal with no vertical displacement, the total potential energy is fully described by the pendulum's gravitational potential energy,

$$\mathcal{V}_T = M_p g y_p = M_p g \ell_p \cos(\alpha(t)). \quad (2.1)$$

2.2.1.2 Kinetic Energy

Next, we will determine the system's total kinetic energy, \mathcal{K}_T . The kinetic energy measures the amount of energy in a system due to its motion. For the SIP system, the total kinetic energy is given by the sum of the translational and rotational kinetic energies of both the cart and its mounted inverted pendulum.

The translational kinetic energy of the motorized cart, \mathcal{K}_{ct} , is

$$\mathcal{K}_{ct} = \frac{1}{2} M \dot{x}(t)^2. \quad (2.2)$$

The cart's rotational kinetic energy, \mathcal{K}_{cr} , is due to the movement of the DC motor's output shaft, and is given by

$$\mathcal{K}_{cr} = \frac{1}{2} J_m \omega_m^2. \quad (2.3)$$

Using the DC motor and planetary gear head technical specification sheets provided in [63] we can express the motor shaft angular velocity, ω_m , in terms of the angular velocity of the motor pinion, ω , as

$$\omega_m = K_g \omega. \quad (2.4)$$

By considering the rack and pinion and the gearbox mechanism, we can rewrite (2.4) in terms of the cart's velocity as

$$K_g \omega = \frac{K_g \dot{x}(t)}{r_{mp}}. \quad (2.5)$$

Substituting equations (2.4) and (2.5) into (2.3), we can express the rotational kinetic energy of the cart as

$$\mathcal{K}_{cr} = \frac{J_m K_g^2 \dot{x}(t)^2}{2r_{mp}^2}. \quad (2.6)$$

The mass of the single inverted pendulum is assumed to be concentrated at its Center Of Gravity (COG), and the pendulum's COG's velocity, v_{COG} is given by

$$v_{COG} = \sqrt{\dot{x}_p(t)^2 + \dot{y}_p(t)^2}. \quad (2.7)$$

According to the reference frame definition presented in Figure 2.1, the absolute Cartesian coordinates of the pendulum's center of gravity are

$$x_p(t) = x(t) - \ell_p \sin(\alpha(t)) \quad \text{and} \quad y_p(t) = \ell_p \cos(\alpha(t)). \quad (2.8)$$

After differentiating (2.8), we can rewrite (2.7) as

$$v_{COG} = \sqrt{\dot{x}(t)^2 - 2\ell_p \cos(\alpha(t))\dot{x}(t)\dot{\alpha}(t) + \ell_p^2 \dot{\alpha}(t)^2} \quad (2.9)$$

Therefore, the pendulum's transitional kinetic energy, \mathcal{K}_{pt} , can be expressed as a function of its center of gravity's linear velocity,

$$\mathcal{K}_{pt} = \frac{1}{2} M_p v_{COG}^2 = \frac{1}{2} M_p (\dot{x}(t)^2 - 2\ell_p \cos(\alpha(t))\dot{x}(t)\dot{\alpha}(t) + \ell_p^2 \dot{\alpha}(t)^2). \quad (2.10)$$

Furthermore, the pendulum's rotational kinetic energy, \mathcal{K}_{pr} , at its COG is given by

$$\mathcal{K}_{pr} = \frac{1}{2} I_p \dot{\alpha}(t)^2, \quad (2.11)$$

where the pendulum's moment of inertia at its COG, I_p is

$$I_p = \int_{-\ell_p}^{\ell_p} r^2 \frac{M_p}{2\ell_p} dr = \frac{1}{3} M_p \ell_p^2. \quad (2.12)$$

Therefore, the total kinetic energy, \mathcal{K}_T , of the system is the sum of the four individual kinetic energies given by Equations (2.2), (2.6), (2.10), and (2.11). After rearranging and simplifying,

the system's total kinetic energy, can be written as

$$\mathcal{K}_T = \frac{1}{2} \left(M + M_p + \frac{J_m K_g^2}{r_{mp}^2} \right) \dot{x}(t)^2 - M_p \ell_p \cos(\alpha(t)) \dot{x}(t) \dot{\alpha}(t) + \frac{2}{3} M_p \ell_p^2 \dot{\alpha}(t)^2. \quad (2.13)$$

2.2.1.3 Lagrange's Equations

The Lagrangian, \mathcal{L} , is given by the difference of the total kinetic energy and the total potential energy,

$$\mathcal{L} = \mathcal{K}_T - \mathcal{V}_T. \quad (2.14)$$

Substituting (2.1) and (2.13) into (2.14) yields

$$\mathcal{L} = \frac{1}{2} \left(M + M_p + \frac{J_m K_g^2}{r_{mp}^2} \right) \dot{x}(t)^2 - M_p \ell_p \cos(\alpha(t)) \dot{x}(t) \dot{\alpha}(t) + \frac{2}{3} M_p \ell_p^2 \dot{\alpha}(t)^2 - M_p g \ell_p \cos(\alpha(t)). \quad (2.15)$$

By definition, the two Lagrange's equations for our system are

$$\frac{\partial^2}{\partial t \partial \dot{x}} \mathcal{L} - \frac{\partial}{\partial x} \mathcal{L} = F_c - B_{eq} \dot{x}(t) \quad (2.16)$$

and

$$\frac{\partial^2}{\partial t \partial \dot{\alpha}} \mathcal{L} - \frac{\partial}{\partial \alpha} \mathcal{L} = -B_p \dot{\alpha}(t), \quad (2.17)$$

where B_{eq} is the equivalent viscous damping coefficient as seen at the motor pinion, and B_p is the equivalent viscous damping coefficient as seen at the pendulum axis [67]. Thus, equations (2.16) and (2.17) account for friction in the form of equivalent viscous damping, however, it should be noted that in the development of the current model the (nonlinear) Coulomb friction applied to the cart, and the force on the cart due to the pendulum's action have been neglected. Using (2.15), the left-hand side of (2.16) can be expressed as

$$\begin{aligned} \frac{\partial^2}{\partial t \partial \dot{x}} \mathcal{L} - \frac{\partial}{\partial x} \mathcal{L} &= \frac{\partial}{\partial t} \left(\left(M + M_p + \frac{J_m K_g^2}{r_{mp}^2} \right) \dot{x}(t) - M_p \ell_p \cos(\alpha(t)) \dot{\alpha}(t) \right) \\ &= \left(M + M_p + \frac{J_m K_g^2}{r_{mp}^2} \right) \ddot{x}(t) + M_p \ell_p \sin(\alpha(t)) \dot{\alpha}(t)^2 - M_p \ell_p \cos(\alpha(t)) \ddot{\alpha}(t). \end{aligned} \quad (2.18)$$

(2.19)

Similarly, the left-hand side of (2.17) can be written as

$$\frac{\partial^2}{\partial t \partial \dot{\alpha}} \mathcal{L} - \frac{\partial}{\partial \alpha} \mathcal{L} = \frac{\partial}{\partial t} \left(-M_p \ell_p \cos(\alpha(t)) \dot{x}(t) + \frac{4}{3} M_p \ell_p^2 \dot{\alpha}(t) \right) - M_p \ell_p g \sin(\alpha(t)) \quad (2.20)$$

$$= -M_p \ell_p \cos(\alpha(t)) \ddot{x}(t) + \frac{4}{3} M_p \ell_p^2 \ddot{\alpha}(t) - M_p \ell_p g \sin(\alpha(t)). \quad (2.21)$$

Then, using (2.19) in equation (2.16) gives

$$\left(M + M_p + \frac{J_m K_g^2}{r_{mp}^2} \right) \ddot{x}(t) + M_p \ell_p \sin(\alpha(t)) \dot{\alpha}(t)^2 - M_p \ell_p \cos(\alpha(t)) \ddot{\alpha}(t) = F_c - B_{eq} \dot{x}(t), \quad (2.22)$$

and using (2.21) in equation (2.17) gives

$$-M_p \ell_p \cos(\alpha(t)) \ddot{x}(t) + \frac{4}{3} M_p \ell_p^2 \ddot{\alpha}(t) - M_p \ell_p g \sin(\alpha(t)) = -B_p \dot{\alpha}(t). \quad (2.23)$$

Solving Equations (2.22) and (2.23) for the second-order time derivatives of x and α results in the two nonlinear equations

$$\begin{aligned} \ddot{x}(t) = & -\frac{3r_{mp}^2 B_p \cos(\alpha(t)) \dot{\alpha}(t)}{\ell_p D(\alpha)} - \frac{4M_p \ell_p r_{mp}^2 \sin(\alpha(t)) \dot{\alpha}(t)^2}{D(\alpha)} - \frac{4r_{mp}^2 B_{eq} \dot{x}(t)}{D(\alpha)} \\ & + \frac{3M_p r_{mp}^2 g \cos(\alpha(t)) \sin(\alpha(t))}{D(\alpha)} + \frac{4r_{mp}^2 F_c}{D(\alpha)} \end{aligned} \quad (2.24)$$

and

$$\begin{aligned} \ddot{\alpha}(t) = & -\frac{3(Mr_{mp}^2 + M_p r_{mp}^2 + J_m K_g^2) B_p \dot{\alpha}(t)}{M_p \ell_p^2 D(\alpha)} - \frac{3M_p r_{mp}^2 \cos(\alpha(t)) \sin(\alpha(t)) \dot{\alpha}(t)^2}{D(\alpha)} \\ & - \frac{3r_{mp}^2 B_{eq} \cos(\alpha(t)) \dot{x}}{\ell_p D(\alpha)} + \frac{3(Mr_{mp}^2 + M_p r_{mp}^2 + J_m K_g^2) g \sin(\alpha(t))}{\ell_p D(\alpha)} + \frac{3r_{mp}^2 \cos(\alpha(t)) F_c}{\ell_p D(\alpha)}, \end{aligned} \quad (2.25)$$

where $D(\alpha) = 4Mr_{mp}^2 + M_p r_{mp}^2 + 4J_m K_g^2 + 3M_p r_{mp}^2 \sin^2(\alpha(t))$. Equations (2.24) and (2.25) represent the Equations Of Motion (EOM) of the SIP system.

2.2.2 Converting to Voltage Input

In our real-time implementation the system's input is equal to the cart's DC motor voltage, V_m , so we must convert the driving force generated by the DC motor acting on the cart through the motor pinion to voltage input. To do this, we will use the electrical schematic of the armature

circuit of a standard DC motor given in Figure 2.2. The driving force, F_c can be expressed as

$$F_c = \frac{K_g T_m}{r_{mp}}. \quad (2.26)$$

By Kirchhoff's voltage law, the directed sum of the electrical potential differences around any

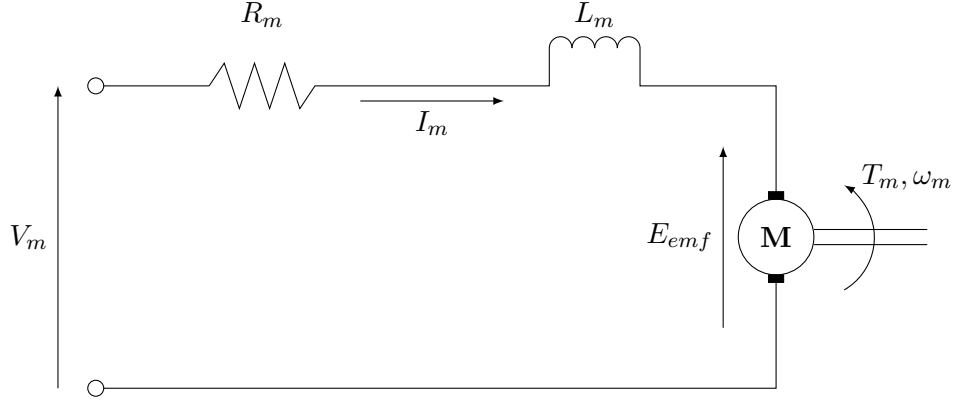


Figure 2.2: DC Motor Electric Circuit

closed circuit is zero, which means that for our system

$$V_m - R_m I_m - L_m \left(\frac{d}{dt} I_m \right) - E_{emf} = 0. \quad (2.27)$$

Since $L_m \ll R_m$, we can disregard the motor inductance and obtain

$$I_m = \frac{V_m - E_{emf}}{R_m}. \quad (2.28)$$

The back-electromotive-force (EMF) voltage created by the the motor is proportional to the motor shaft velocity (i. e., $E_{emf} = K_m \omega_m$), so we can rewrite (2.28) as

$$I_m = \frac{V_m - K_m \omega_m}{R_m}, \quad (2.29)$$

where K_m is the back-EMF constant. Furthermore, the torque, T_m , generated by the DC motor can be expressed as

$$T_m = K_t I_m. \quad (2.30)$$

Substituting equations (2.29) and (2.30) into equation (2.26) leads to

$$F_c = \frac{K_g K_t (V_m - K_m \omega_m)}{R_m r_{mp}}. \quad (2.31)$$

Using equations (2.4) and (2.5) in (2.31), and rearranging leads to

$$F_c = -\frac{K_g^2 K_t K_m \dot{x}(t)}{R_m r_{mp}^2} + \frac{K_g K_t V_m}{R_m r_{mp}}. \quad (2.32)$$

Utilizing (2.32) to convert the driving force to voltage input, we can rewrite the EOM given in (2.24) and (2.25) as

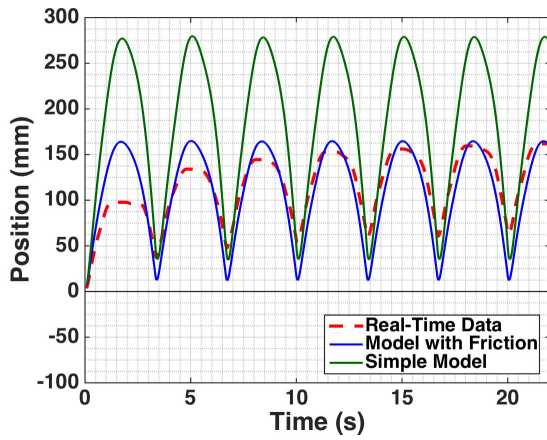
$$\begin{aligned} \ddot{x}(t) = & -\frac{3r_{mp}^2 B_p \cos(\alpha(t)) \dot{\alpha}(t)}{\ell_p D(\alpha)} - \frac{4M_p \ell_p r_{mp}^2 \sin(\alpha(t)) \dot{\alpha}(t)^2}{D(\alpha)} - \frac{4(R_m r_{mp}^2 B_{eq} + K_g^2 K_t K_m) \dot{x}(t)}{R_m D(\alpha)} \\ & + \frac{3M_p r_{mp}^2 g \cos(\alpha(t)) \sin(\alpha(t))}{D(\alpha)} + \frac{4r_{mp} K_g K_t V_m}{R_m D(\alpha)} \end{aligned} \quad (2.33)$$

and

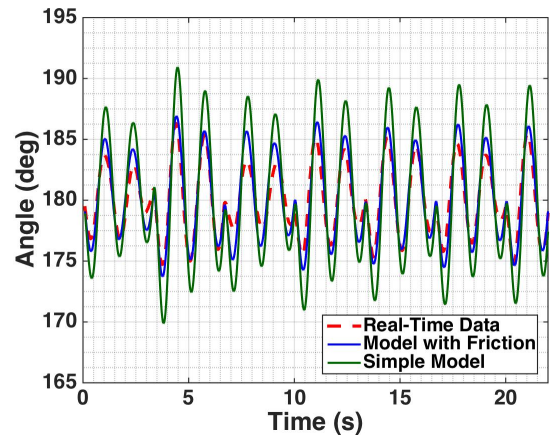
$$\begin{aligned} \ddot{\alpha}(t) = & -\frac{3(Mr_{mp}^2 + M_p r_{mp}^2 + J_m K_g^2) B_p \dot{\alpha}(t)}{M_p \ell_p^2 D(\alpha)} - \frac{3M_p r_{mp}^2 \cos(\alpha(t)) \sin(\alpha(t)) \dot{\alpha}(t)^2}{D(\alpha)} \\ & - \frac{3(R_m r_{mp}^2 B_{eq} + K_g^2 K_t K_m) \cos(\alpha(t)) \dot{x}}{R_m \ell_p D(\alpha)} + \frac{3(Mr_{mp}^2 + M_p r_{mp}^2 + J_m K_g^2) g \sin(\alpha(t))}{\ell_p D(\alpha)} \\ & + \frac{3r_{mp} K_g K_t \cos(\alpha(t)) V_m}{R_m \ell_p D(\alpha)}. \end{aligned} \quad (2.34)$$

2.3 Model Calibration

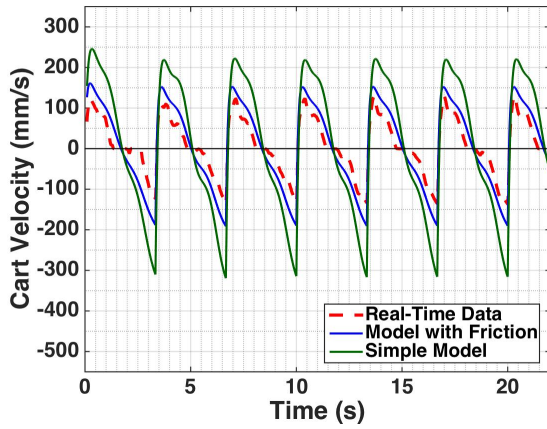
Using the Simulink diagrams in Appendix B.2, we compare the real-time states with the states obtained by our model in response to the same voltage input. The parameter values used during the simulation are given in Appendix A.2. We test the performance of our model both with and without the viscous damping friction terms, B_{eq} and B_p . The voltage input for the experiment is given in Figure 2.3(e), while the states responses are given in Figures 2.3(a)-(d). The experiment clearly indicates that the model with friction simulates state responses that are more similar to the real-time experimental states responses than the state responses generated by the simple model with no friction.



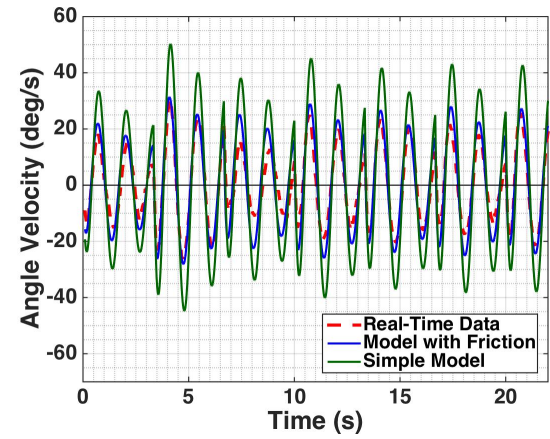
(a) Cart Position



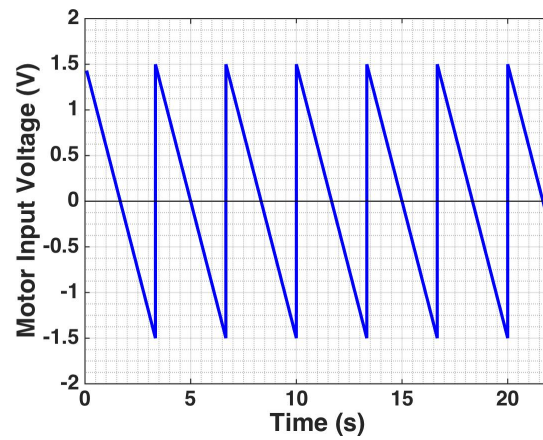
(b) Pendulum Angle



(c) Cart Velocity



(d) Pendulum's Angular Velocity



(e) Input Voltage

Figure 2.3: Comparison of real-time data with simulated model response with and without friction.

Chapter 3

Stabilization Control

3.1 Problem Statement

Based on the Equations of Motion, (2.33) and (2.34), the state-space representation of our system has the form

$$\frac{d}{dt}X(t) = f(X(t)) + B(X(t))u(t) \quad (3.1)$$

where X , the system's state vector is given by $X^T(t) = [x(t), \alpha(t), \dot{x}(t), \dot{\alpha}(t)] = [x_1, x_2, x_3, x_4]$, and the input u is set to equal the input voltage of the cart's DC motor, i.e. $u = V_m$. The nonlinear function $f(X)$ can be expressed as

$$f(X) = \begin{bmatrix} 0 & 0 & 1 & 0 \\ 0 & 0 & 0 & 1 \\ 0 & 0 & a_{33} & a_{34} \\ 0 & 0 & a_{43} & a_{44} \end{bmatrix} \begin{bmatrix} x_1 \\ x_2 \\ x_3 \\ x_4 \end{bmatrix} + \begin{bmatrix} 0 \\ 0 \\ \frac{3M_p r_{mp}^2 g \cos(x_2) \sin(x_2)}{D(x_2)} \\ \frac{3(Mr_{mp}^2 + M_p r_{mp}^2 + J_m K_g^2)g \sin(x_2)}{\ell_p D(x_2)} \end{bmatrix} \quad (3.2)$$

where

$$\begin{aligned} a_{33} &= -\frac{4(R_m r_{mp}^2 B_{eq} + K_g^2 K_t K_m)}{R_m D(x_2)} & a_{34} &= -\frac{3r_{mp}^2 B_p \cos(x_2) + 4M_p \ell_p^2 r_{mp}^2 \sin(x_2)x_4}{\ell_p D(x_2)} \\ a_{43} &= -\frac{3(R_m r_{mp}^2 B_{eq} + K_g^2 K_t K_m) \cos(x_2)}{R_m \ell_p D(x_2)} \\ a_{44} &= -\frac{3(Mr_{mp}^2 + M_p r_{mp}^2 + J_m K_g^2)B_p + 3M_p^2 \ell_p^2 r_{mp}^2 \cos(x_2) \sin(x_2)x_4}{M_p \ell_p^2 D(x_2)} \end{aligned}$$

and $D(x_2) = 4Mr_{mp}^2 + M_p r_{mp}^2 + 4J_m K_g^2 + 3r_{mp}^2 M_p \sin^2(x_2)$. The state-dependent matrix,

$B(X(t))$, in Equation (3.1) is given by

$$B(X(t)) = \begin{bmatrix} 0 \\ 0 \\ \frac{4r_{mp}K_gK_t}{R_mD(x_2)} \\ \frac{3r_{mp}K_gK_t \cos(x_2)}{\ell_p R_mD(x_2)} \end{bmatrix}. \quad (3.3)$$

Now, consider the cost functional

$$J(X_0, u) = \int_0^\infty (X^T Q X + R u^2) dt, \quad (3.4)$$

where Q is a given constant-valued 4×4 symmetric positive-semidefinite matrix and R is a positive scalar. In the case of starting and balancing the inverted pendulum in the upright position, the optimal control problem is to find a state feedback control $u^*(X)$ which minimizes the cost (3.4) for the initial condition $X_0^T = [0, 0, 0, 0]$.

The optimal feedback control for the system in (3.1) with cost (3.4) has the form

$$u^*(X) = -\frac{1}{2}R^{-1}B^T(X)S_X(X), \quad (3.5)$$

where the function S is the solution to the Hamilton-Jacobi-Bellman (HJB) equation

$$S_X^T(X)f(X) - \frac{1}{4}S_X^T(X)B(X)R^{-1}B^T(X)S_X(X) + X^T Q X = 0, \quad (3.6)$$

and S_X represents the Jacobian of S with respect to the states.

3.2 Power Series Based Controller

It is well know that the HJB equation is very difficult to solve analytically. Several efforts have been made to numerically approximate the solution of the HJB equation in order to obtain a usable feedback control. This section describes one of these methods that was adapted for the SIP system based on [14].

3.2.1 Power Series Approximation

As has been done by Garrard and others in references [26, 28, 27], the solution of the HJB equation can be numerically approximated using its power series expansion

$$S(X) = \sum_{n=0}^{\infty} S_n(X), \quad (3.7)$$

where each S_n is a scalar polynomial containing all possible combinations of products of the state elements with a total order of $n+2$. Similarly, the nonlinear function $f(X)$ can be approximated by

$$f(X) = A_0 X + \sum_{n=2}^{\infty} f_n(X), \quad (3.8)$$

where each f_n is a function vector with a scalar polynomial containing all possible combinations of products of the state elements with a total order of n in every row. In our implementation, the power series of f was calculated using the MATLAB function `taylor` from the Symbolic Math Toolbox. Here, A_0 represents the linearization of $f(X)$ around the upright position (i.e. $X^T = [0; 0; 0; 0]$) and is given by

$$A_0 = \begin{bmatrix} 0 & 0 & 1 & 0 \\ 0 & 0 & 0 & 1 \\ 0 & \frac{3M_p r_{mp}^2 g}{D} & -\frac{4(R_m r_{mp}^2 B_{eq} + K_g^2 K_t K_m)}{R_m D} & -\frac{3r_{mp}^2 B_p}{\ell_p D} \\ 0 & \frac{3(Mr_{mp}^2 + M_p r_{mp}^2 + J_m K_g^2)g}{\ell_p D} & -\frac{3(R_m r_{mp}^2 B_{eq} + K_g^2 K_t K_m)}{R_m \ell_p D} & -\frac{3(Mr_{mp}^2 + M_p r_{mp}^2 + J_m K_g^2)B_p}{M_p \ell_p^2 D} \end{bmatrix} \quad (3.9)$$

$$\approx \begin{bmatrix} 0 & 0 & 1 & 0 \\ 0 & 0 & 0 & 1 \\ 0 & 1.4967 & -11.6073 & -0.004821 \\ 0 & 25.6815 & -26.3643 & -0.08273 \end{bmatrix},$$

where $D = 4Mr_{mp}^2 + Mpr_{mp}^2 + 4J_m K_g^2$. Furthermore, the state-dependent matrix, $B(X)$, can be approximated by

$$B(X) = \sum_{n=0}^{\infty} B_n(X), \quad (3.10)$$

where each B_n is a 4×1 vector with a scalar polynomial containing all possible combinations of products of the state elements with a total order of n in every row. In our implementation, the power series of B was calculated using the MATLAB function `taylor` from the Symbolic Math Toolbox. Note that B_0 is the linearization of B around the zero angle (i.e. $x_2 = 0$), and

is given by

$$B = \begin{bmatrix} 0 \\ 0 \\ \frac{4r_{mp}K_gK_t}{R_m(4Mr_{mp}^2+M_pr_{mp}^2+4J_mK_g^2)} \\ \frac{3r_{mp}K_gK_t}{\ell_p R_m(4Mr_{mp}^2+M_pr_{mp}^2+4J_mK_g^2)} \end{bmatrix} \approx \begin{bmatrix} 0 \\ 0 \\ 1.52441 \\ 3.46248 \end{bmatrix}. \quad (3.11)$$

The matrices in (3.9) and (3.11) were evaluated using the parameter values from Appendix A.2.

The expansions (3.7), (3.8), and (3.10) can be substituted into the HJB equation (3.6) to yield

$$\left[\sum_{n=0}^{\infty} (S_n)_X^T \right] \left[A_0 X + \sum_{n=2}^{\infty} f_n \right] - \frac{1}{4} \left[\sum_{n=0}^{\infty} (S_n)_X^T \right] \left[\sum_{n=0}^{\infty} B_n \right] R^{-1} \left[\sum_{n=0}^{\infty} B_n^T \right] \left[\sum_{n=0}^{\infty} (S_n)_X \right] + X^T Q X = 0. \quad (3.12)$$

We can separate out powers of the states to obtain a series of equations,

$$(S_0)_X^T A_0 X - \frac{1}{4} (S_0)_X^T B_0 R^{-1} B_0^T (S_0)_X + X^T Q X = 0, \quad (3.13)$$

$$\begin{aligned} (S_1)_X^T A_0 X - \frac{1}{4} (S_1)_X^T B_0 R^{-1} B_0^T (S_0)_X - \frac{1}{4} (S_0)_X^T B_0 R^{-1} B_0^T (S_1)_X - \frac{1}{4} (S_0)_X^T B_1 R^{-1} B_0^T (S_0)_X \\ - \frac{1}{4} (S_0)_X^T B_0 R^{-1} B_1^T (S_0)_X + (S_0)_X^T f_2(X) = 0 \end{aligned} \quad (3.14)$$

$$(S_n)_X^T A_0 X - \frac{1}{4} \sum_{k=0}^n \sum_{j=0}^{n-k} \sum_{i=0}^{n-k-j} [(S_k)_X^T B_j R^{-1} B_i^T (S_{n-k-j-i})_X] + \sum_{k=0}^{n-1} [(S_k)_X^T f_{n+1-k}(X)] = 0, \quad (3.15)$$

where $n = 2, 3, 4, \dots$. The solution of equation (3.13) is

$$S_0(X) = X^T P X, \quad (3.16)$$

where the symmetric positive-definite matrix, P , solves the Algebraic Riccati Equation (ARE)

$$P A_0 + A_0^T P - P B_0 R^{-1} B_0^T P + Q = 0. \quad (3.17)$$

Note that using (3.16) in (3.5) results in the traditional (LQR) control. The theories for the LQR problem have been well-established, and multiple stable and robust algorithms for solving (3.17) have already been developed and are well documented in the literature and in textbooks [13, 48]. It is possible to solve equations (3.14)-(3.15) for S_n , $n = 1, 2, 3, \dots$, however, this method can get very complicated quickly. In [26], Garrard proposed a very easy method of

finding $(S_1)_X$ and obtaining a quadratic type control. Instead of the polynomial representation, we may use the solution of (3.13) and make the substitution $(S_0)_X = 2PX$ in equation (3.14) to obtain

$$(S_1)_X^T A_0 X - \frac{1}{4}(S_1)_X^T B_0 R^{-1} B_0^T (2PX) - \frac{1}{4}(2X^T P) B_0 R^{-1} B_0^T (S_1)_X - \frac{1}{4}(2X^T P) B_1 R^{-1} B_0^T (2PX) - \frac{1}{4}(2X^T P) B_0 R^{-1} B_1^T (2PX) + (2X^T P) f_2(X) = 0. \quad (3.18)$$

This can be rearranged to yield

$$X^T [A_0^T (S_1)_X - P B_0 R^{-1} B_0^T (S_1)_X - P B_1 R^{-1} B_0^T P X - P B_0 R^{-1} B_1^T P X + 2P f_2(X)] = 0, \quad (3.19)$$

which is satisfied when

$$(S_1)_X = (A_0^T - P B_0 R^{-1} B_0^T)^{-1} (P B_1 R^{-1} B_0^T P X + P B_0 R^{-1} B_1^T P X - 2P f_2(X)). \quad (3.20)$$

Equation (3.30) along with the $(S_0)_X$ term give a quadratic feedback control law of the form

$$u^*(X) = -R^{-1} B_0^T \left[P X + (A_0^T - P B_0 R^{-1} B_0^T)^{-1} \left(\frac{1}{2} P B_1 R^{-1} B_0^T P X + \frac{1}{2} P B_0 R^{-1} B_1^T P X - P f_2(X) \right) \right]. \quad (3.21)$$

The series expansion of $f(X)$ in our case doesn't contain any quadratic terms (i.e. $f_2(X) = 0$), and $B_1 = 0$, so (3.14) is trivially solved by $S_1 = 0$. In this case, by [14], equation (3.15) for $n = 2$ will be of the form

$$(S_2)_X^T A_0 X - \frac{1}{4}(S_2)_X^T B_0 R^{-1} B_0^T (S_0)_X - \frac{1}{4}(S_0)_X^T B_0 R^{-1} B_0^T (S_2)_X - \frac{1}{4}(S_0)_X^T B_2 R^{-1} B_0^T (S_0)_X - \frac{1}{4}(S_0)_X^T B_0 R^{-1} B_2^T (S_0)_X + (S_0)_X^T f_3(X) = 0 \quad (3.22)$$

which is exactly the same form as (3.14) except that S_1 is replaced by S_2 , B_1 is replaced by B_2 , and f_2 is replaced by f_3 . Thus, the solution is comparable to that of (3.14), with

$$(S_2)_X = (A_0^T - P B_0 R^{-1} B_0^T)^{-1} (P B_2 R^{-1} B_0^T P X + P B_0 R^{-1} B_2^T P X - 2P f_3(X)), \quad (3.23)$$

resulting in a feedback control of the form

$$u^*(X) = -R^{-1} B_0^T \left[P X + (A_0^T - P B_0 R^{-1} B_0^T)^{-1} \left(\frac{1}{2} P B_2 R^{-1} B_0^T P X + \frac{1}{2} P B_0 R^{-1} B_2^T P X - P f_3(X) \right) \right]. \quad (3.24)$$

3.2.2 Constant Matrix B

The previously derived control law given by (3.24) can be simplified by replacing the state-dependent matrix $B(X)$ by its linearization, B_0 in the state-space representation of our system given by (3.1). Doing this yields the state-space representation in the form

$$\frac{d}{dt}X(t) = f(X(t)) + B_0 u(t) \quad (3.25a)$$

$$X(0) = X_0. \quad (3.25b)$$

Then, equation (3.12) becomes

$$\left[\sum_{n=0}^{\infty} (S_n)_X^T \right] \left[A_0 X + \sum_{n=2}^{\infty} f_n(X) \right] - \frac{1}{4} \left[\sum_{n=0}^{\infty} (S_n)_X^T \right] B_0 R^{-1} B_0^T \left[\sum_{n=0}^{\infty} (S_n)_X \right] + X^T Q X = 0. \quad (3.26)$$

Separating out powers of the states modifies the system of equations in (3.13)-(3.15) to

$$(S_0)_X^T A_0 X - \frac{1}{4} (S_0)_X^T B_0 R^{-1} B_0^T (S_0)_X + X^T Q X = 0, \quad (3.27)$$

$$(S_1)_X^T A_0 X - \frac{1}{4} (S_1)_X^T B_0 R^{-1} B_0^T (S_0)_X - \frac{1}{4} (S_0)_X^T B_0 R^{-1} B_0^T (S_1)_X + (S_0)_X^T f_2(X) = 0, \quad (3.28)$$

$$(S_n)_X^T A_0 X - \frac{1}{4} \sum_{k=0}^n [(S_k)_X^T B_0 R^{-1} B_0^T (S_{n-k})_X] + \sum_{k=0}^{n-1} [(S_k)_X^T f_{n+1-k}(X)] = 0, \quad (3.29)$$

where $n = 2, 3, 4, \dots$. The solution to (3.28) is

$$(S_1)_X = -2(A_0^T - P B_0 R^{-1} B_0^T)^{-1} P f_2(X), \quad (3.30)$$

which yields the quadratic feedback control law of the form

$$u^*(X) = -R^{-1} B_0^T [P X - (A_0^T - P B_0 R^{-1} B_0^T)^{-1} P f_2(X)]. \quad (3.31)$$

As before, since for our model $f_2(X) = 0$, we replace S_1 by S_2 , and f_2 by f_3 to obtain the control law

$$u^*(X) = -R^{-1} B_0^T [P X - (A_0^T - P B_0 R^{-1} B_0^T)^{-1} P f_3(X)]. \quad (3.32)$$

3.2.2.1 Simulation Results: Constant B vs. State-Dependent B

Using the Simulink diagram provided in Figure B.5, we compare the performance of the control law given by (3.32) with the performance of the control law given by (3.24) in simulation. We start the stabilization simulation with a starting angle $\alpha_0 = 5^\circ$, and after five seconds

we introduce a 10° angular disturbance. The simulation results are given Figure 3.1. It can be seen that the two controllers perform very similarly near the upright position, so in future implementations we will use the simpler controller with constant B given by (3.32).

3.2.3 Incorporation of a State-Dependent Weighting Matrix

The performance of the controller greatly depends on the selection of the constant valued weighting matrices, Q and R , in the cost function (3.4). Finding the right values that will lead to the desired performance requires careful tuning that can be very time consuming. Changing these matrices from constant to state-dependent can not only improve the performance of the controller, but can also shorten the time required for tuning. The above derivation can be adapted to incorporate a state-dependent matrix, $Q(X)$, into the cost function. To do this, first we need to expand $Q(X)$ as a power series

$$Q(X) = \sum_{n=0}^{\infty} Q_n(X), \quad (3.33)$$

where the entries in each Q_n are scalar polynomials containing all possible combinations of products of the state elements with a total order of n . Replacing Q by the power series of $Q(X)$ in equation (3.26) and separating out powers of the states modifies the system of equations in (3.27)-(3.29) to

$$(S_0)_X^T A_0 X - \frac{1}{4} (S_0)_X^T B_0 R^{-1} B_0^T (S_0)_X + X^T Q_0 X = 0, \quad (3.34)$$

$$(S_1)_X^T A_0 X - \frac{1}{4} (S_1)_X^T B_0 R^{-1} B_0^T (S_0)_X - \frac{1}{4} (S_0)_X^T B_0 R^{-1} B_0^T (S_1)_X + (S_0)_X^T f_2(X) + X^T Q_1 X = 0, \quad (3.35)$$

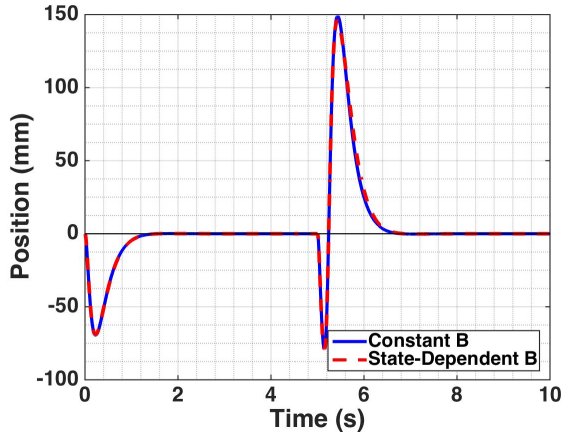
$$(S_n)_X^T A_0 X - \frac{1}{4} \sum_{k=0}^n [(S_k)_X^T B_0 R^{-1} B_0^T (S_{n-k})_X] + \sum_{k=0}^{n-1} [(S_k)_X^T f_{n+1-k}(X)] + X^T Q_n X = 0, \quad (3.36)$$

where $n = 2, 3, 4, \dots$. The solution to (3.35) is

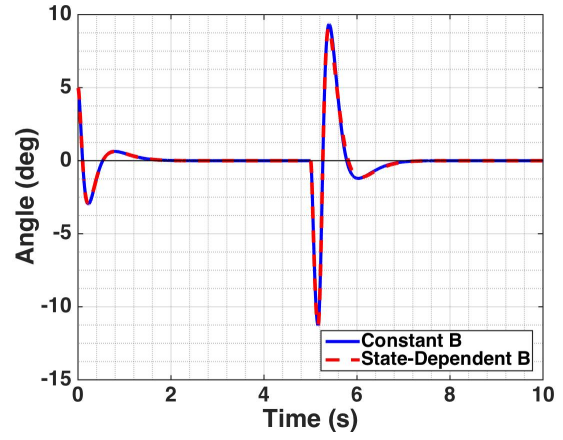
$$(S_1)_X = -(A_0^T - P B_0 R^{-1} B_0^T)^{-1} (2P f_2(X) + Q_1 X), \quad (3.37)$$

which yields the feedback control law

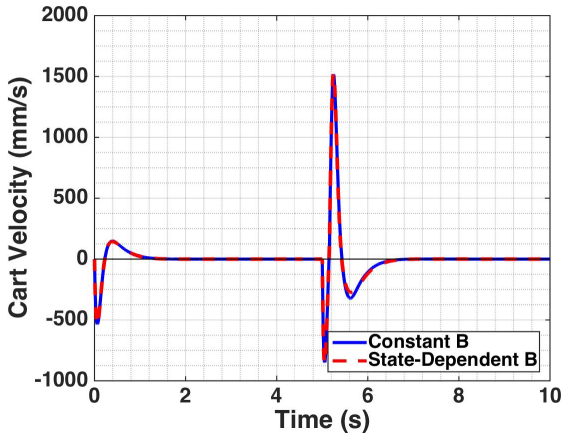
$$u^*(X) = -R^{-1} B_0^T \left[P X - (A_0^T - P B_0 R^{-1} B_0^T)^{-1} \left(P f_2(X) + \frac{1}{2} Q_1 X \right) \right]. \quad (3.38)$$



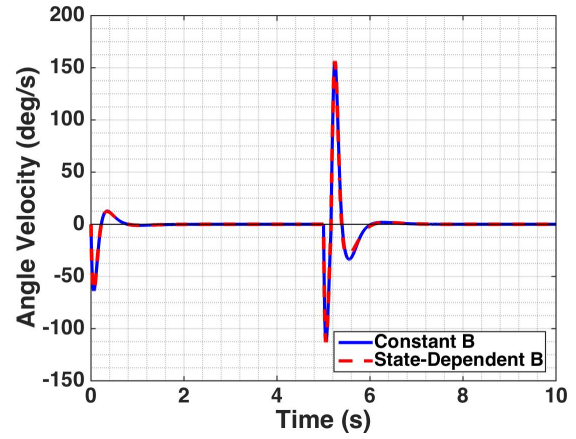
(a) Cart Position



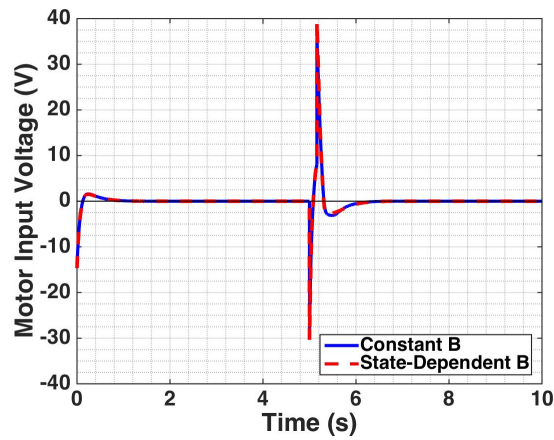
(b) Pendulum Angle



(c) Cart Velocity



(d) Pendulum's Angular Velocity



(e) Input Voltage

Figure 3.1: Stabilization controller with state-dependent B given by (3.24) versus controller with constant B given by (3.32)

Since for our model $f_2(X) = 0$, we will define Q so that $Q_1 = 0$ to make sure that (3.35) can be solved trivially by $S_1 = 0$. As before, in this case we can replace Q_1 by Q_2 , S_1 by S_2 , and f_2 by f_3 to obtain the the control law

$$u^*(X) = -R^{-1}B_0^T \left[PX - (A_0^T - PB_0R^{-1}B_0^T)^{-1} \left(Pf_3(X) + \frac{1}{2}Q_2X \right) \right]. \quad (3.39)$$

3.3 Stability Analysis

Using the Simulink diagram provided in Figure B.6 with various initial states, we can estimate the stability region for both the power series controller and the LQR controller. The parameters in the Simulink diagrams are initialized using the Matlab code provided in Appendix B.1.

First, we only consider different initial pendulum angles and make the other initial states zero. We repeat the simulation several times with different initial angles to find the first angle where each of the controllers is able to stabilize the pendulum. This angle for the power series based controller is $\alpha_0 = 30.85^\circ$, while for the LQR controller it is $\alpha_0 = 23.30^\circ$. Since we have a finite track length, we continue repeating the simulation until we find the first initial angle where each of the controllers is able to stabilize the pendulum and the position of the cart stays within the track (i.e. $|x| < 400$ mm). The first such angle for the power series based controller is $\alpha_0 = 21.08^\circ$, while for the LQR controller it is $\alpha_0 = 18.22^\circ$. The simulated state responses and control effort for these angles of interest are given in Figure 3.2 for the power series based controller and Figure 3.3 for the LQR controller. The red dashed lines in Figures 3.2a and 3.3a indicate the end of the track.

To get a better estimate of the stability region for the power series controller and the LQR controller, we repeat the simulations with various initial conditions for two of the states while keeping the initial condition for the other two states zero. The stability region estimates for initial conditions $-180^\circ \leq \alpha_0 \leq 180^\circ$, $-590^\circ/s \leq \dot{\alpha}_0 \leq 590^\circ/s$, $x_0 = 0$, and $\dot{x}_0 = 0$ are given in Figure 3.4, for initial conditions $-180^\circ \leq \alpha_0 \leq 180^\circ$, $-390 \text{ mm} \leq x_0 \leq 390 \text{ mm}$, $\dot{x}_0 = 0$, and $\dot{\alpha}_0 = 0$ are given in Figure 3.5, and for initial conditions $-390 \text{ mm} \leq x_0 \leq 390 \text{ mm}$, $-1000 \text{ mm/s} \leq \dot{x}_0 \leq 1000 \text{ mm/s}$, $\alpha_0 = 0$, and $\dot{\alpha}_0 = 0$ are given in Figure 3.6. The range on the velocities was selected based on the values possible by the apparatus we use for real-time implementation, while the range on the cart's position was selected to be within the length of the track. For all three cases, the stability region of the power series controller is bigger than the stability region of the LQR controller.

Finally, we repeat the simulations with various initial conditions for three of the states while keeping the initial condition for the remaining state zero. The stability region estimate for initial conditions $-180^\circ \leq \alpha_0 \leq 180^\circ$, $-590^\circ/s \leq \dot{\alpha}_0 \leq 590^\circ/s$, $-1000 \text{ mm/s} \leq \dot{x}_0 \leq 1000$

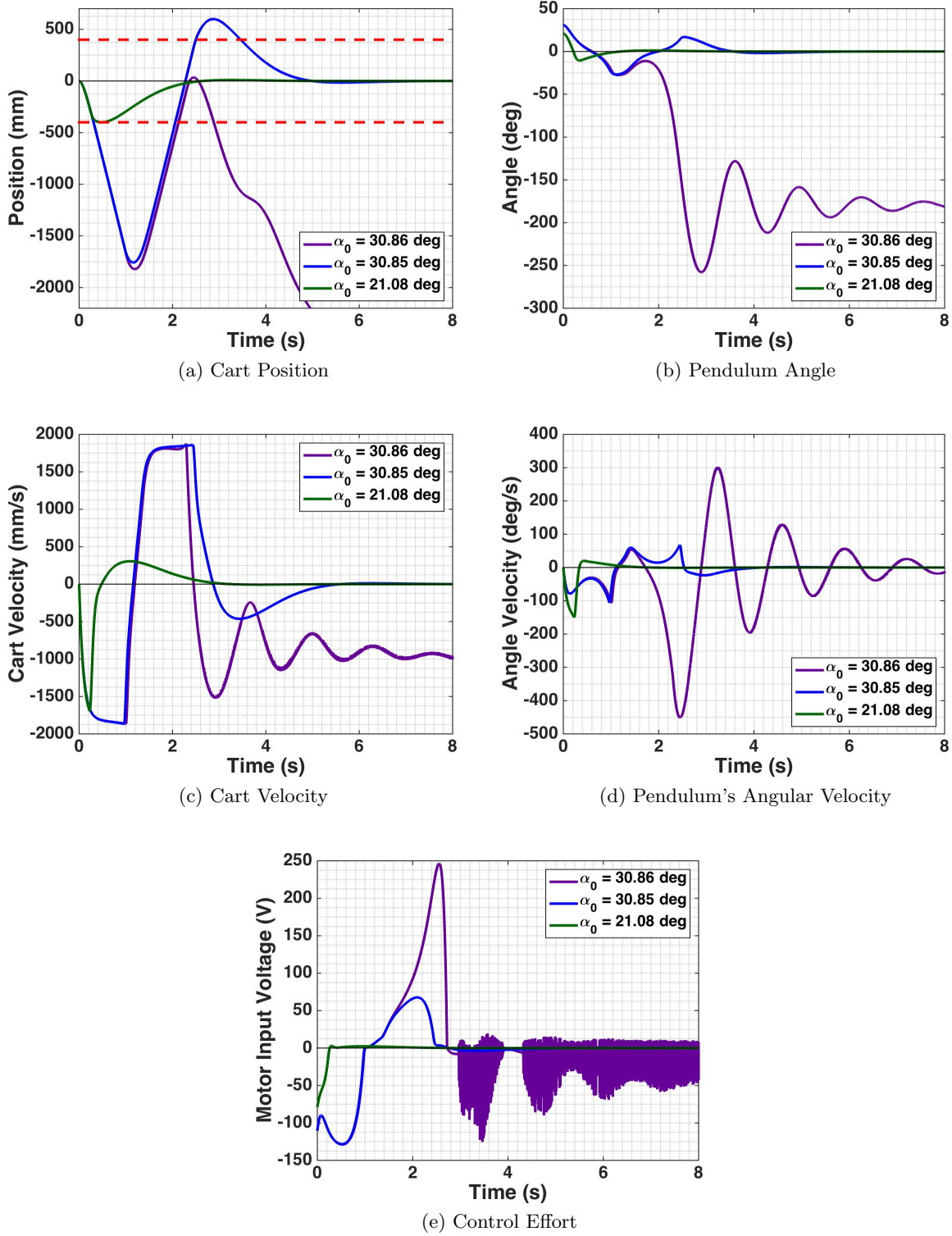
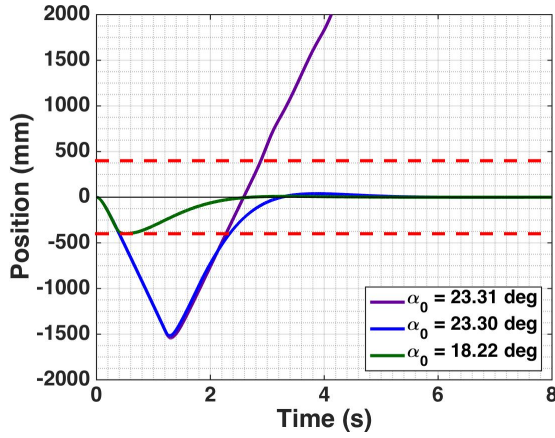
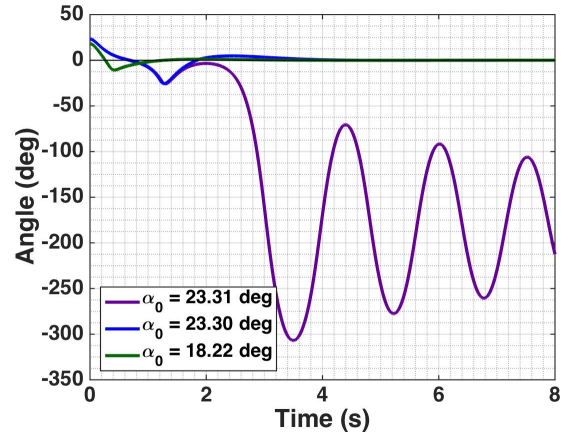


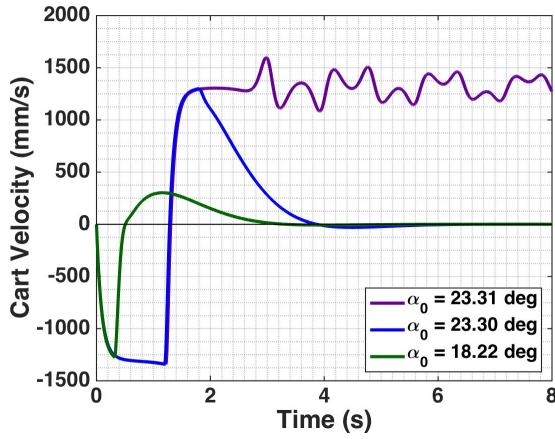
Figure 3.2: Stabilization simulation results for the power series based controller with various initial angles, and $x_0 = 0$, $\dot{\alpha}_0 = 0$, $\dot{x}_0 = 0$.



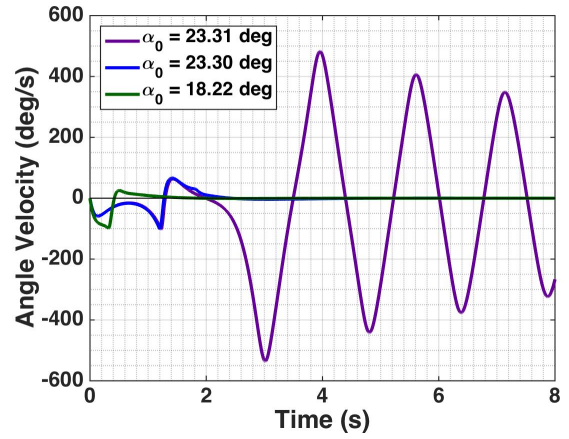
(a) Cart Position



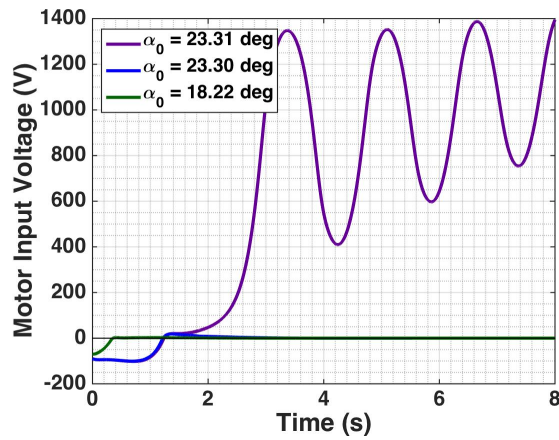
(b) Pendulum Angle



(c) Cart Velocity



(d) Pendulum's Angular Velocity



(e) Control Effort

Figure 3.3: Stabilization simulation results for the LQR controller with various initial angles, and $x_0 = 0, \dot{\alpha}_0 = 0, \dot{x}_0 = 0$.

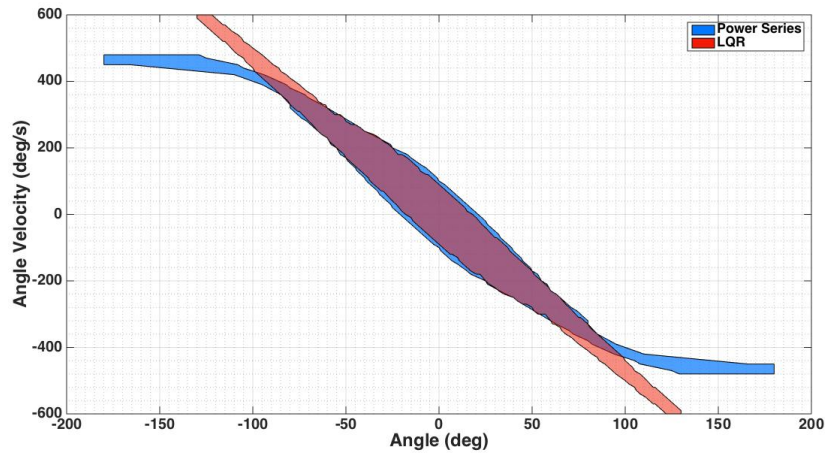


Figure 3.4: Stability region estimate for both the power series based controller and the LQR controller for various initial pendulum angles and angular velocities with zero initial cart position and cart velocity.

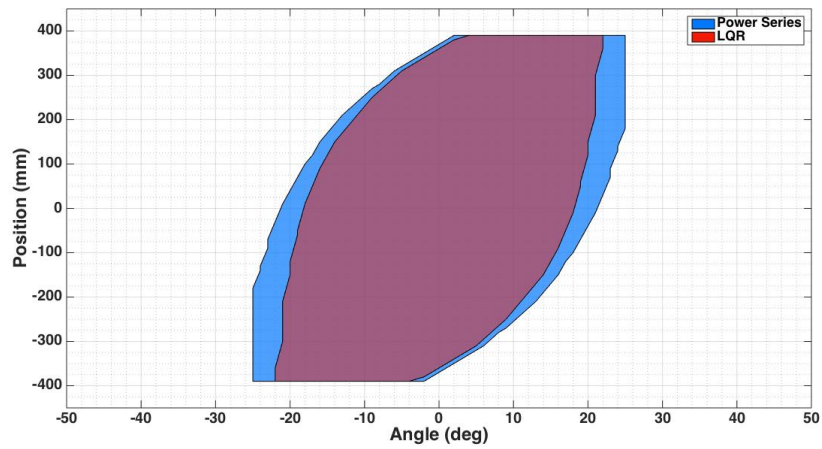


Figure 3.5: Stability region estimate for both the power series based controller and the LQR controller for various initial pendulum angles and cart positions with zero initial cart velocity and angular velocity.

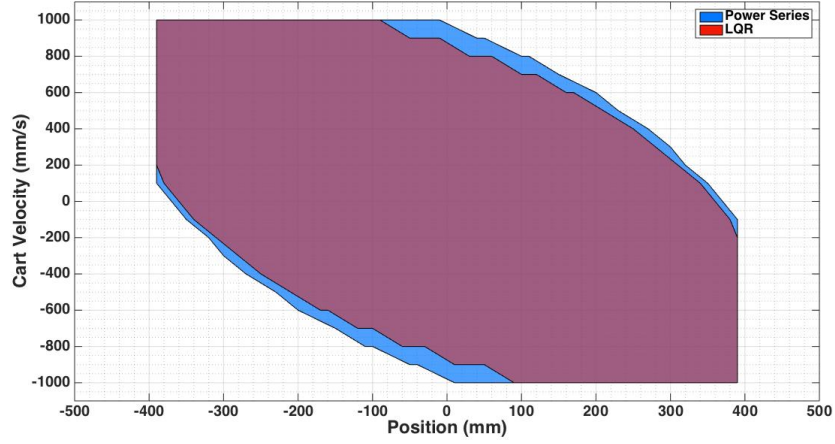


Figure 3.6: Stability region estimate for both the power series based controller and the LQR controller for various initial cart positions and cart velocities with zero initial pendulum angle and angular velocity.

mm/s, and $x_0 = 0$ is given in Figure 3.7 for the power series based controller and in Figure 3.8 for the LQR controller. The stability region estimate for initial conditions $-180^\circ \leq \alpha_0 \leq 180^\circ$, $-590^\circ/s \leq \dot{\alpha}_0 \leq 590^\circ/s$, $-390 \text{ mm} \leq x_0 \leq 390 \text{ mm}$, and $\dot{x}_0 = 0$ is given in Figure 3.9 for the power series based controller and in Figure 3.10 for the LQR controller. The stability region of the power series controller is bigger than the stability region of the LQR controller for both cases.

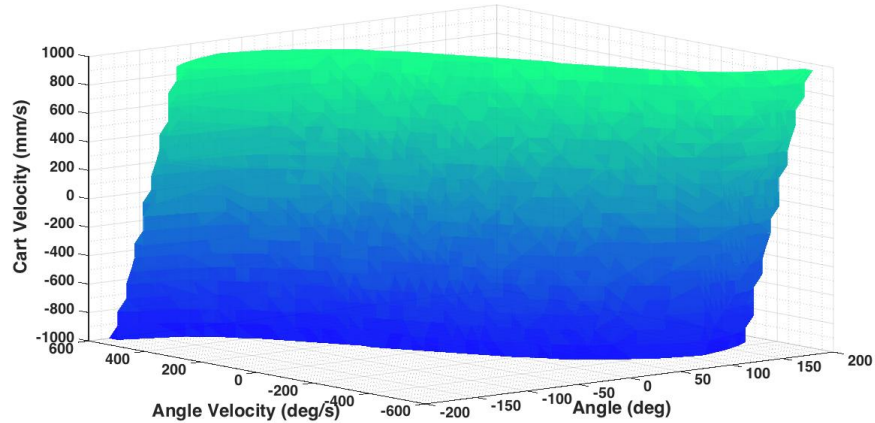


Figure 3.7: Stability region estimate for the power series based controller for various initial pendulum angles, angular velocities, and cart velocities with zero initial cart position.

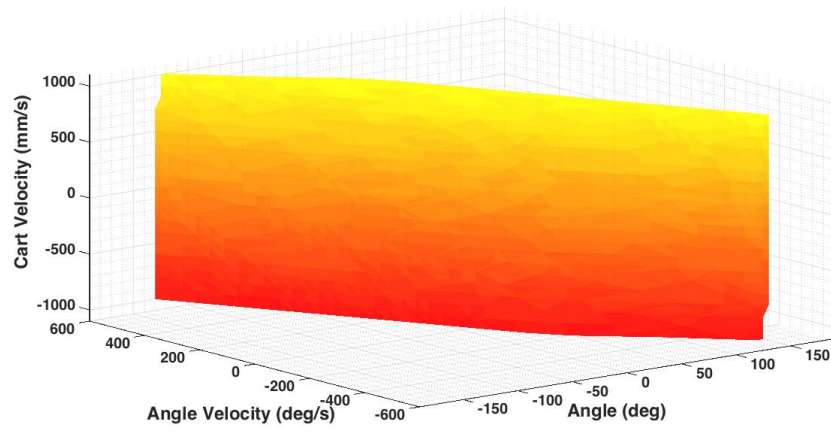


Figure 3.8: Stability region estimate for the LQR controller for various initial pendulum angles, angular velocities, and cart velocities with zero initial cart position.

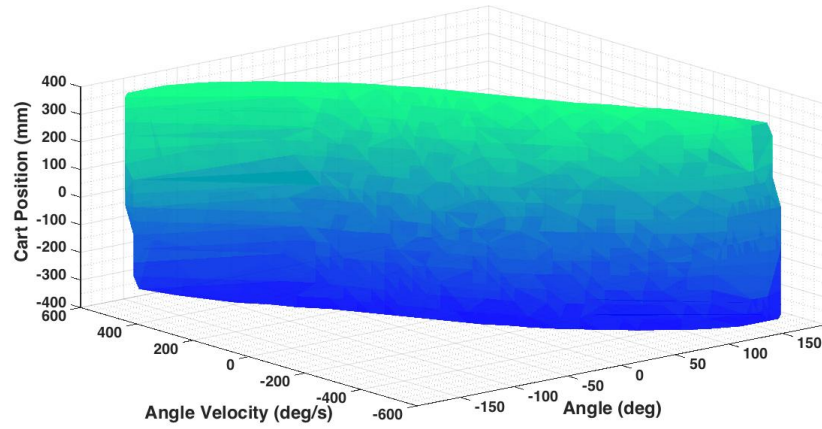


Figure 3.9: Stability region estimate for the power series based controller for various initial cart positions, pendulum angles, and angular velocities with zero initial cart velocity.

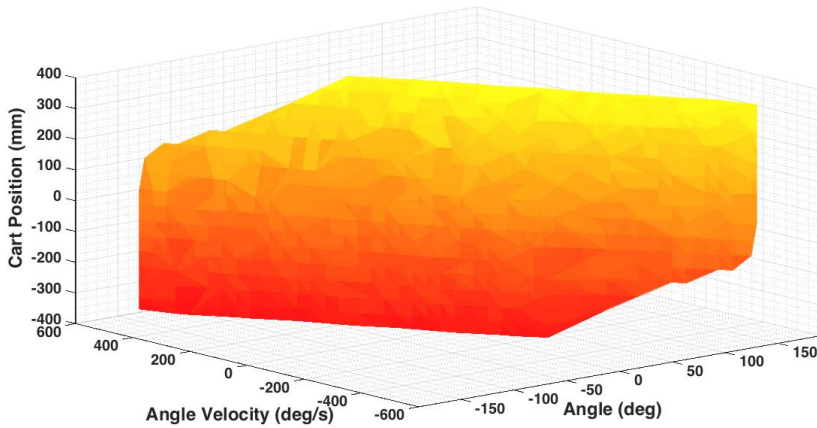


Figure 3.10: Stability region estimate for the LQR controller for various initial cart positions, pendulum angles, and angular velocities with zero initial cart velocity.

3.4 Real-Time Implementation

3.4.1 Apparatus

For our real-time experiments we use apparatus designed and provided by Quanser Consulting Inc. (119 Spy Court Markham, Ontario, L3R 5H6, Canada). This includes a single inverted pendulum mounted on an IP02 servo plant (pictured in Figure 3.11), a VoltPAQ amplifier, and a Q2-USB DAQ control board. The IP02 cart incorporates a Faulhaber Coreless DC Motor (2338S006) coupled with a Faulhaber Planetary Gearhead Series 23/1. The cart is also equipped with a US Digital S1 single-ended optical shaft encoder. The detailed technical specifications can be found in reference [63]. A diagram of our experimental setup is included in Figure 3.12.

3.4.2 Design Specifications

The goal of our real-time experiment is to stabilize the inverted pendulum in the upright position with minimal cart movement and control effort. The weights $Q \geq 0$ and $R > 0$ in the cost functional (3.4) must be chosen so that the system satisfies the following design performance requirements specified:

1. Regulate the pendulum angle around its upright position and never exceed a ± 1 -degree-deflection from it, i.e. $|\alpha| \leq 1.0^\circ$.
2. Minimize the control effort produced, which is proportional to the motor input voltage V_m . The power amplifier should not go into saturation in any case, i.e. $|V_m| \leq 10V$.

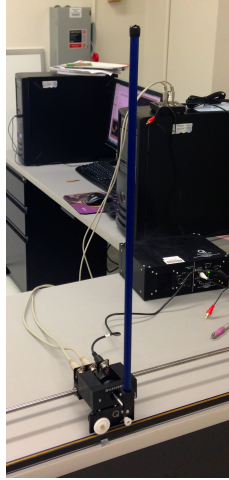


Figure 3.11: Single inverted pendulum mounted on a Quanser IP02 servo plant.

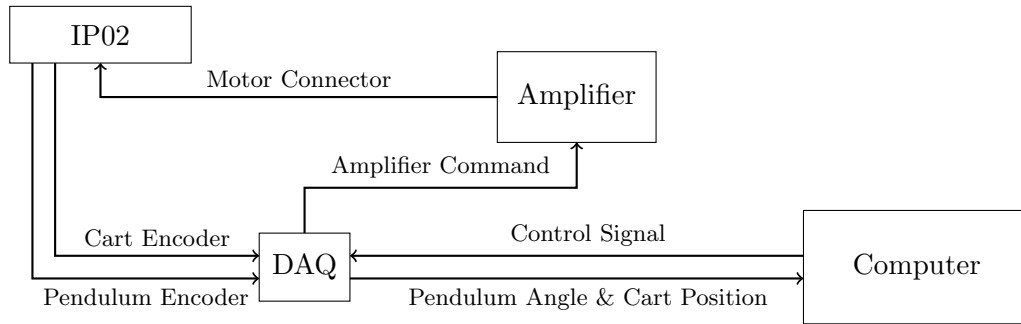


Figure 3.12: Diagram of experimental setup.

3.5 Experimental Results

Our Experimental results were obtained using Simulink in MATLAB and Quanser’s QuArc real-time control software. Our Simulink diagrams are provided in Appendix B.4.

3.5.1 Constant Weighting Matrices

The choice of the weighting matrices has a great effect on the performance of the controller. In order to strongly penalize non-zero positions, the state weight Q must be chosen with large weights on the positions and small weights on the velocities. The value of R needs to be sufficiently large to ensure that the power amplifier doesn’t go into saturation and to prevent excessive cart movement, however, if it is too large then the states might deviate from the zero position too much.

We have tested several different pairs of possible weighting matrices. To find a good com-

bination of values for Q and R , we use the following tuning procedure based on the procedure described by Quanser in [67]:

1. Perform a simulation with a particular choice for Q and R using the Simulink diagrams provided in B.3. Study the resulting state response and control effort required. If the state response and control effort are within the desired ranges then move onto the next step. Otherwise, adjust the values in Q and R , and run the simulation again. To adjust the values consider the following:
 - If the cart’s position deviates too much from the center, then try increasing Q_{11} and/or decreasing Q_{22} .
 - If the pendulum’s angle deviates too much from the upright position, then try increasing Q_{22} , and/or decreasing Q_{11} .
 - If the motor input voltage goes into saturation, try increasing R and/or decreasing Q_{11} together with Q_{22} .
2. If the simulation results are satisfactory, then test the Q and R matrices in real-time using the Simulink diagrams provided in Appendix B.4. Adjust the values of Q and R until the state responses and the required control effort are satisfactory. While adjusting the values, use the considerations from the previous step. If the cart is too “hyperactive” and vibrates excessively, then try increasing R and/or decreasing Q_{11} together with Q_{22} .

Three particular pairs of Q and R matrices were selected using the above procedure, however, within the given considerations these choices are somewhat arbitrary. The first of these choices is $Q = \text{diag}(0.75, 4, 0, 0)$ and $R = 0.0003$, which is the default choice for the LQR controller provided by Quanser in [67]. Notice that for the states only the non-zero cart position and pendulum angle are penalized, and there is no weight on the velocities. The resulting state responses and required control effort for both the power series controller and the LQR controller are presented in Figures 3.13-3.17. Both controllers satisfy the design requirements provided in Section 3.4.2, however, the power series based controller performs slightly better with lower control effort and state responses closer to zero. The second choice for these matrices, $Q = \text{diag}(5, 50, 0, 0)$ and $R = 0.002$, results in an improvement of the performance of both controllers. The corresponding state responses and required control effort are presented in Figures 3.18-3.22. Again, the power series controller yields slightly better results. The third choice, $Q = \text{diag}(800, 150, 1, 1)$ and $R = 0.1$, also includes penalties on the velocities, however it results in worse performance for both control methods. The corresponding state responses and required control effort are presented in Figures 3.23-3.27. Both methods still satisfy the design conditions, but the LQR controller for this case slightly outperforms the power series controller. Tables 3.1

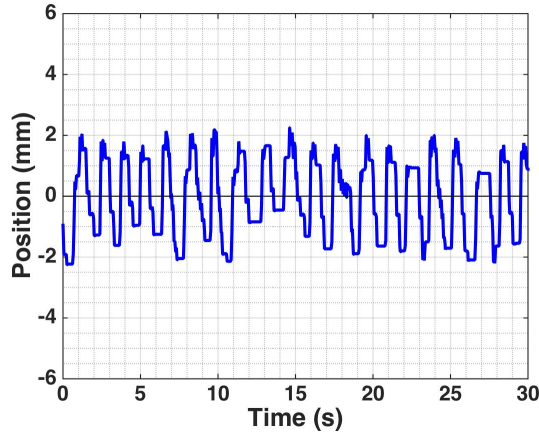
and 3.2 provide a summary of the analysis of the state responses and the control effort for these three pairs of weighting matrices.

Table 3.1: Summary of stabilization state response with different weighting matrices.

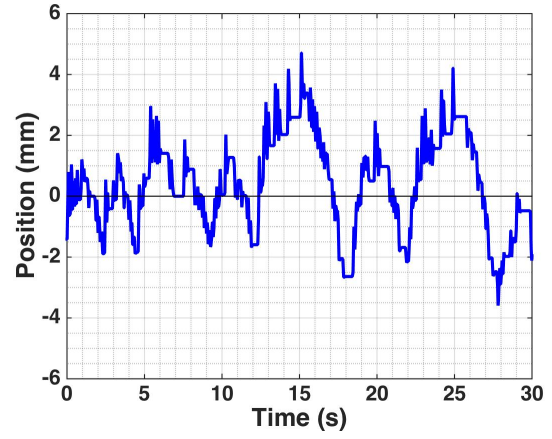
Q	R	Method	$ x _{\max}$ $ x _{\text{avg}}$	$ \alpha _{\max}$ $ \alpha _{\text{avg}}$	$ \dot{x} _{\max}$ $ \dot{x} _{\text{avg}}$	$ \dot{\alpha} _{\max}$ $ \dot{\alpha} _{\text{avg}}$
$\text{diag}(0.75, 4, 0, 0)$	0.0003	Power Series	2.25 mm	0.176°	47.43 mm/s	5.84 deg/s
			1.17 mm	5.82e-02°	4.97 mm/s	0.702 deg/s
		LQR	4.71 mm	0.264°	44.97 mm/s	6.63 deg/s
			1.26 mm	3.67e-02°	5.79 mm/s	0.931 deg/s
$\text{diag}(5, 50, 0, 0)$	0.002	Power Series	1.68 mm	8.79e-02°	24.4 mm/s	3.46 deg/s
			0.44 mm	2.24e-02°	4.31 mm/s	0.71 deg/s
		LQR	2.16 mm	0.176°	47.8 mm/s	5.43 deg/s
			0.697 mm	3.62e-02°	5.62 mm/s	0.83 deg/s
$\text{diag}(800, 150, 1, 1)$	0.1	Power Series	3.8 mm	0.35°	67.3 mm/s	10.73 deg/s
			0.775 mm	5.08e-02°	7.35 mm/s	1.1 deg/s
		LQR	3.19 mm	0.264°	60.6 mm/s	9.19 deg/s
			0.973 mm	6.68e-02°	6.82 mm/s	0.99 deg/s

Table 3.2: Summary of control effort with different weighting matrices.

Q	R	Method	V_{\max}	$ V_m _{\text{avg}}$	$\int_0^{30} V_m dt$
$\text{diag}(0.75, 4, 0, 0)$	0.0003	Power Series	1.9 Volts	0.328 Volts	9.85 Volts
		LQR	2.23 Volts	0.38	11.26
$\text{diag}(5, 50, 0, 0)$	0.002	Power Series	1.77 Volts	0.32 Volts	9.57 Volts
		LQR	2.11 Volts	0.37	11.2
$\text{diag}(800, 150, 1, 1)$	0.002	Power Series	2.9 Volts	0.41 Volts	12.33 Volts
		LQR	2.59 Volts	0.392	11.77

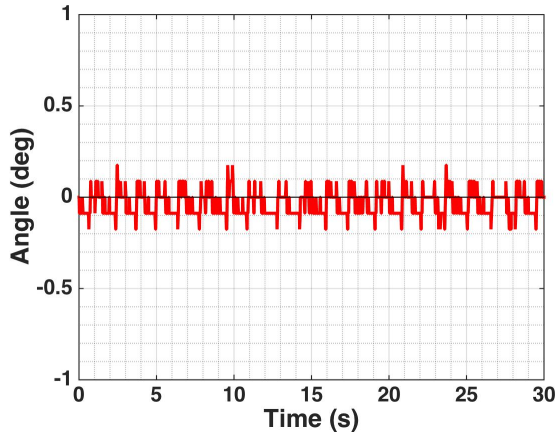


(a) Power Series Controller
 $|x| < 2.25 \text{ mm}$, $|x|_{\text{avg}} = 1.17 \text{ mm}$

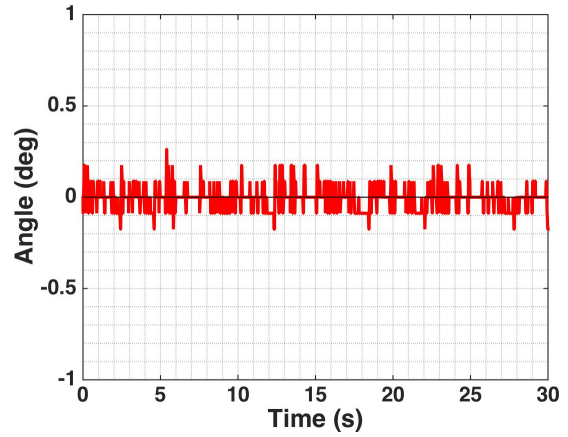


(b) LQR
 $|x| < 4.71 \text{ mm}$, $|x|_{\text{avg}} = 1.26 \text{ mm}$

Figure 3.13: Cart position with power series based controller vs. LQR:
 $Q = \text{diag}(0.75, 4, 0, 0)$ and $R = 0.0003$.

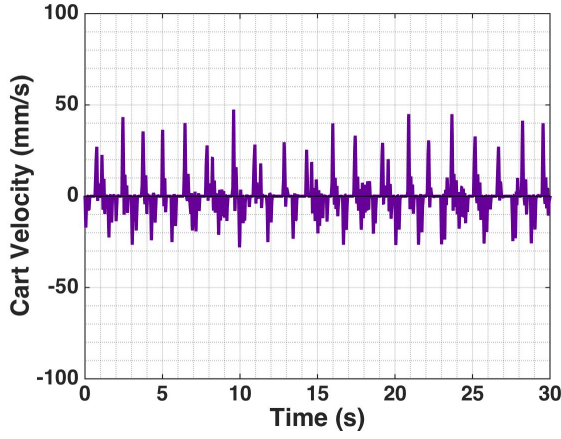


(a) Power Series Controller
 $|\alpha| < 0.176^\circ$, $|\alpha|_{\text{avg}} = 5.87\text{e-}02^\circ$

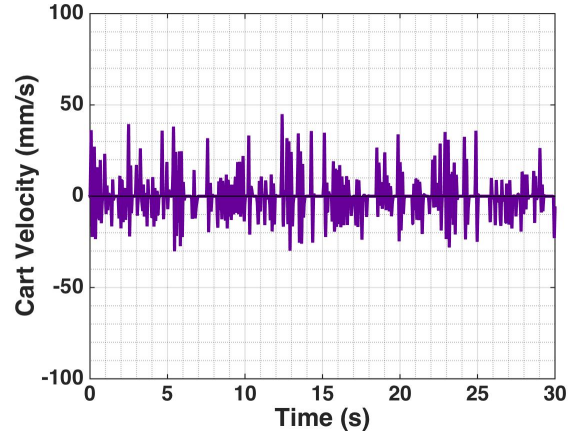


(b) LQR
 $|\alpha| < 0.264^\circ$, $|\alpha|_{\text{avg}} = 3.67\text{e-}02^\circ$

Figure 3.14: Pendulum's angle with power series based controller vs. LQR:
 $Q = \text{diag}(0.75, 4, 0, 0)$ and $R = 0.0003$.

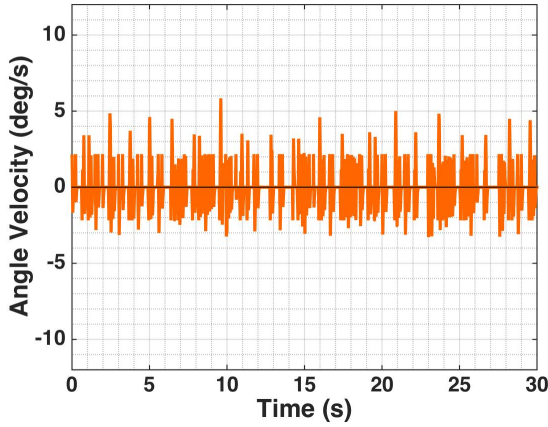


(a) Power Series Controller
 $|\dot{x}| < 47.43 \text{ mm/s}$, $|\dot{x}|_{\text{avg}} = 4.97 \text{ mm/s}$

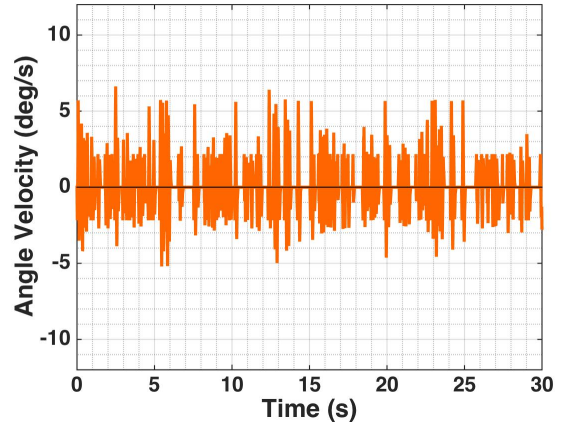


(b) LQR
 $|\dot{x}| < 44.97 \text{ mm/s}$, $|\dot{x}|_{\text{avg}} = 5.79 \text{ mm/s}$

Figure 3.15: Cart velocity with power series based controller vs. LQR:
 $Q = \text{diag}(0.75, 4, 0, 0)$ and $R = 0.0003$.

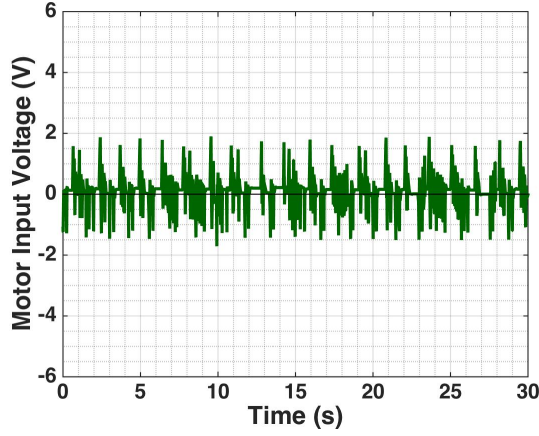


(a) Power Series Controller
 $|\dot{\alpha}| < 5.84 \text{ deg/s}$, $|\dot{\alpha}|_{\text{avg}} = 0.702 \text{ deg/s}$

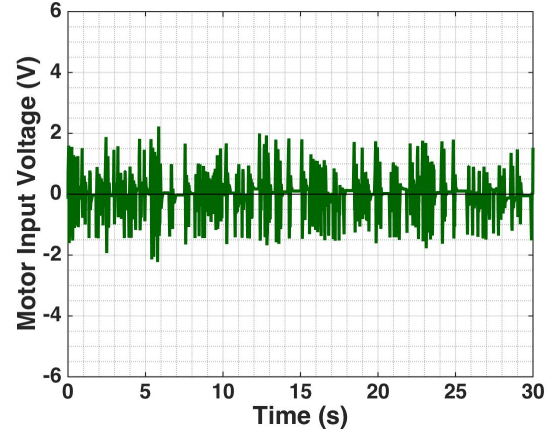


(b) LQR
 $|\dot{\alpha}| < 6.63 \text{ deg/s}$, $|\dot{\alpha}|_{\text{avg}} = 0.931 \text{ deg/s}$

Figure 3.16: Pendulum's angular velocity with power series based controller vs. LQR:
 $Q = \text{diag}(0.75, 4, 0, 0)$ and $R = 0.0003$.

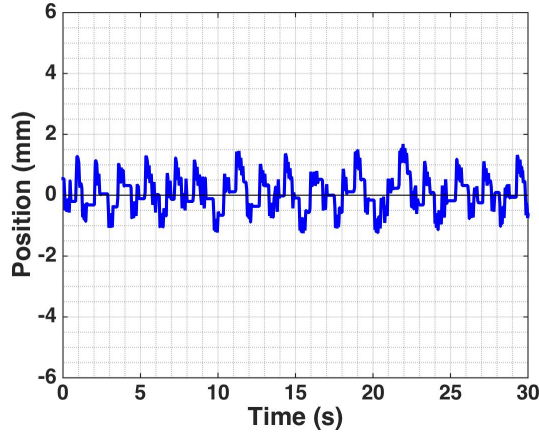


(a) Power Series Controller
 $|V_m| < 1.9$ Volts, $|V_m|_{\text{avg}} = 0.328$ Volts,
 $\int_0^{30} |V_m| dt = 9.85$

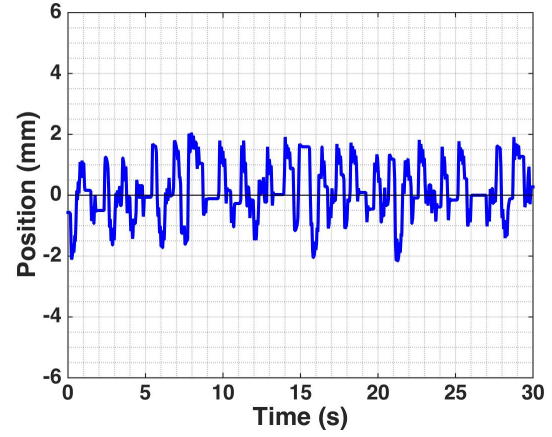


(b) LQR
 $|V_m| < 2.23$ Volts, $|V_m|_{\text{avg}} = 0.376$ Volts,
 $\int_0^{30} |V_m| dt = 11.26$

Figure 3.17: Control effort with power series based controller vs. LQR:
 $Q = \text{diag}(0.75, 4, 0, 0)$ and $R = 0.0003$.

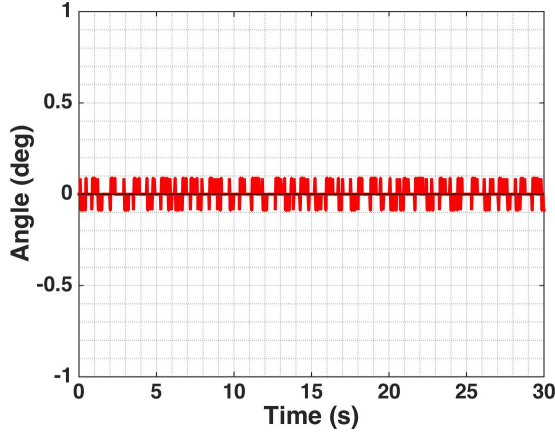


(a) Power Series Controller
 $|x| < 1.68$ mm, $|x|_{\text{avg}} = 0.44$ mm

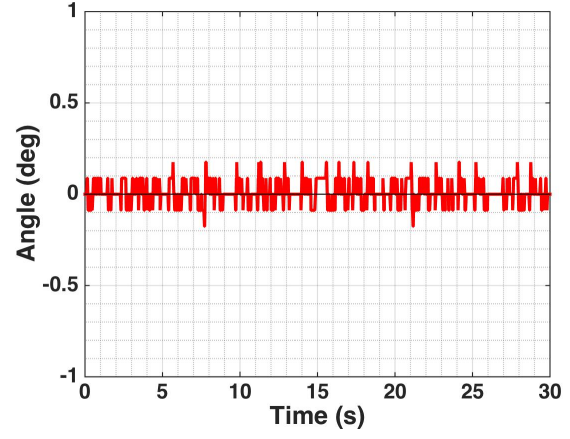


(b) LQR
 $|x| < 2.16$ mm, $|x|_{\text{avg}} = 0.697$ mm

Figure 3.18: Cart position with power series based controller vs. LQR:
 $Q = \text{diag}(5, 50, 0, 0)$ and $R = 0.002$.

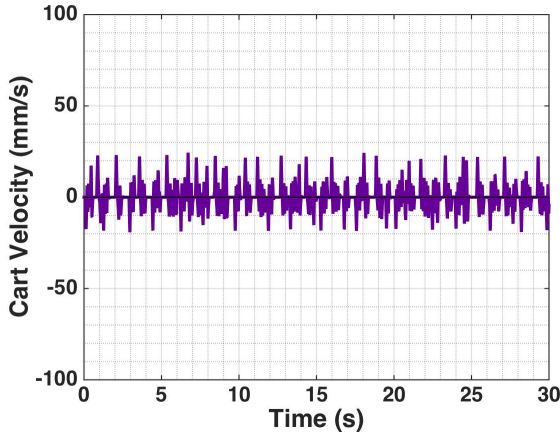


(a) Power Series Controller
 $|\alpha| < 8.79\text{e-}02^\circ$, $|\alpha|_{\text{avg}} = 2.24\text{e-}02^\circ$

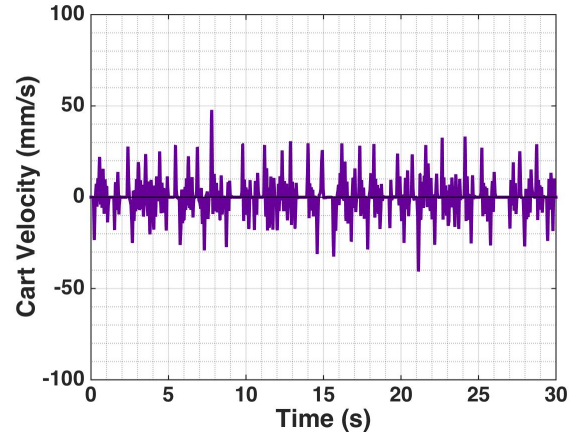


(b) LQR
 $|\alpha| < 0.176^\circ$, $|\alpha|_{\text{avg}} = 3.62\text{e-}02^\circ$

Figure 3.19: Pendulum's angle with power series based controller vs. LQR:
 $Q = \text{diag}(5, 50, 0, 0)$ and $R = 0.002$.

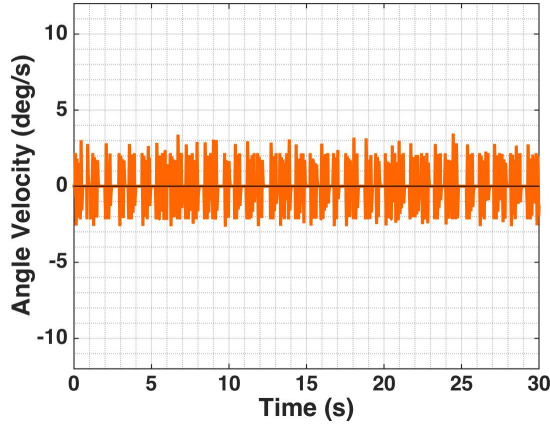


(a) Power Series Controller
 $|\dot{x}| < 24.4 \text{ mm/s}$, $|\dot{x}|_{\text{avg}} = 4.31 \text{ mm/s}$

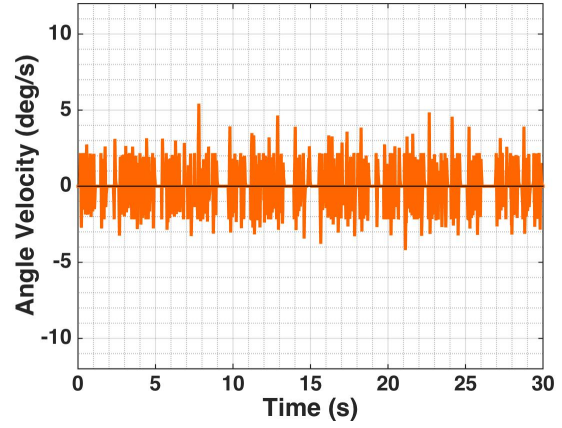


(b) LQR
 $|\dot{x}| < 47.8 \text{ mm/s}$, $|\dot{x}|_{\text{avg}} = 5.62 \text{ mm/s}$

Figure 3.20: Cart velocity with power series based controller vs. LQR:
 $Q = \text{diag}(5, 50, 0, 0)$ and $R = 0.002$.

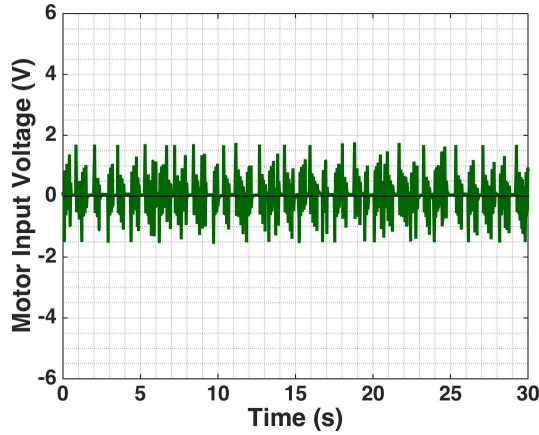


(a) Power Series Controller
 $|\dot{\alpha}| < 3.46 \text{ deg/s}$, $|\dot{\alpha}|_{\text{avg}} = 0.71 \text{ deg/s}$

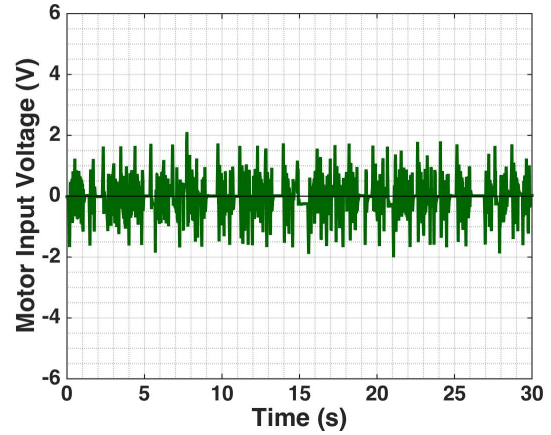


(b) LQR
 $|\dot{\alpha}| < 5.43 \text{ deg/s}$, $|\dot{\alpha}|_{\text{avg}} = 0.83 \text{ deg/s}$

Figure 3.21: Pendulum's angular velocity with power series based controller vs. LQR:
 $Q = \text{diag}(5, 50, 0, 0)$ and $R = 0.002$.

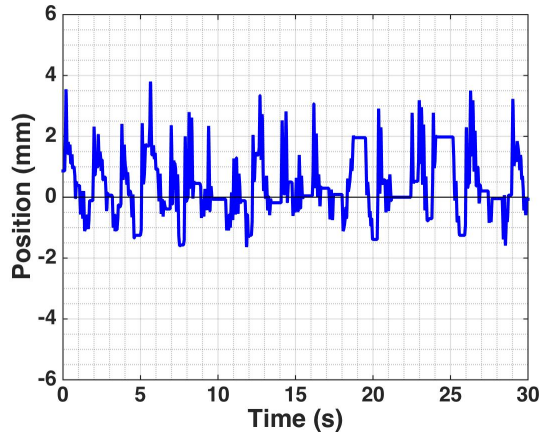


(a) Power Series Controller
 $|V_m| < 1.77 \text{ Volts}$, $|V_m|_{\text{avg}} = 0.32 \text{ Volts}$
 $\int_0^{30} |V_m| dt = 9.57$

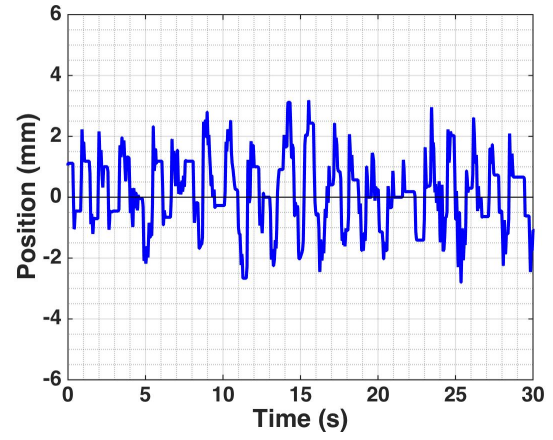


(b) LQR
 $|V_m| < 2.11 \text{ Volts}$, $|V_m|_{\text{avg}} = 0.37 \text{ Volts}$
 $\int_0^{30} |V_m| dt = 11.2$

Figure 3.22: Control effort with power series based controller vs. LQR:
 $Q = \text{diag}(5, 50, 0, 0)$ and $R = 0.002$.

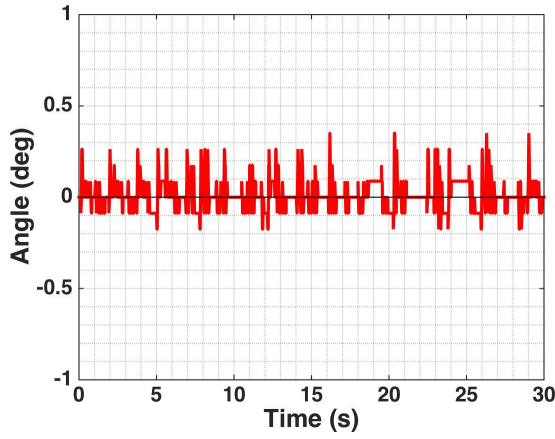


(a) Power Series Controller
 $|x| < 3.8 \text{ mm}$, $|x|_{\text{avg}} = 0.775 \text{ mm}$

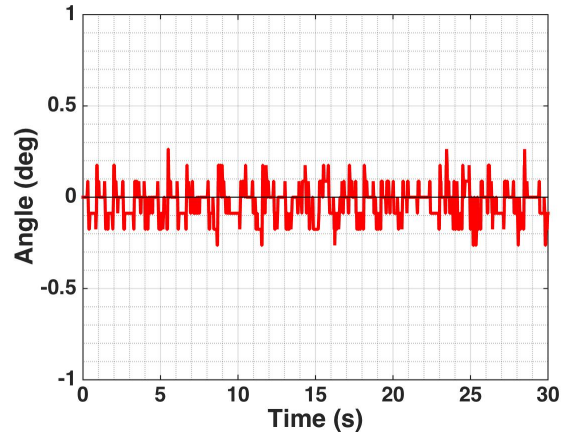


(b) LQR
 $|x| < 3.19 \text{ mm}$, $|x|_{\text{avg}} = 0.973 \text{ mm}$

Figure 3.23: Cart position with power series based controller vs. LQR:
 $Q = \text{diag}(800, 150, 1, 1)$ and $R = 0.1$.

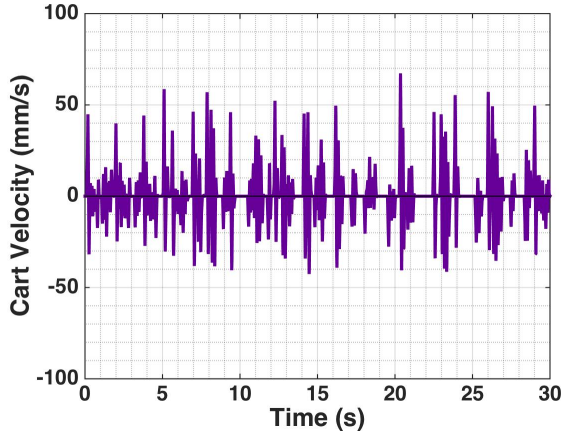


(a) Power Series Controller
 $|\alpha| < 0.35^\circ$, $|\alpha|_{\text{avg}} = 5.08\text{e-}02^\circ$

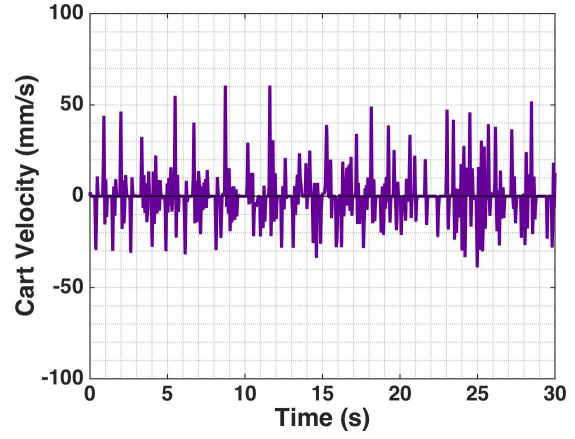


(b) LQR
 $|\alpha| < 0.264^\circ$, $\alpha_{\text{avg}} = 6.68\text{e-}02^\circ$

Figure 3.24: Pendulum's angle with power series based controller vs. LQR:
 $Q = \text{diag}(800, 150, 1, 1)$ and $R = 0.1$.

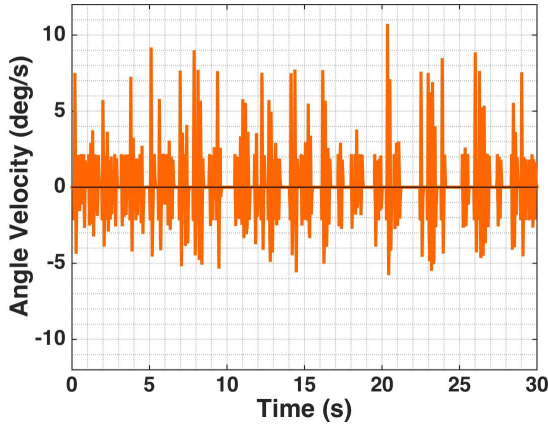


(a) Power Series Controller
 $|\dot{x}| < 67.3 \text{ mm/s}$, $|\dot{x}|_{\text{avg}} = 7.35 \text{ mm/s}$

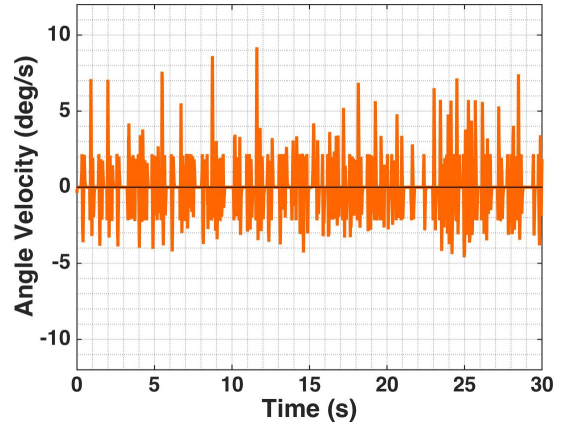


(b) LQR
 $|\dot{x}| < 60.6 \text{ mm/s}$, $|\dot{x}|_{\text{avg}} = 6.82 \text{ mm/s}$

Figure 3.25: Cart velocity with power series based controller vs. LQR:
 $Q = \text{diag}(800, 150, 1, 1)$ and $R = 0.1$.



(a) Power Series Controller
 $|\dot{\alpha}| < 10.73 \text{ deg/s}$, $|\dot{\alpha}|_{\text{avg}} = 1.1 \text{ deg/s}$



(b) LQR
 $|\dot{\alpha}| < 9.19 \text{ deg/s}$, $|\dot{\alpha}|_{\text{avg}} = 0.99 \text{ deg/s}$

Figure 3.26: Pendulum's angular velocity with power series based controller vs. LQR:
 $Q = \text{diag}(800, 150, 1, 1)$ and $R = 0.1$.

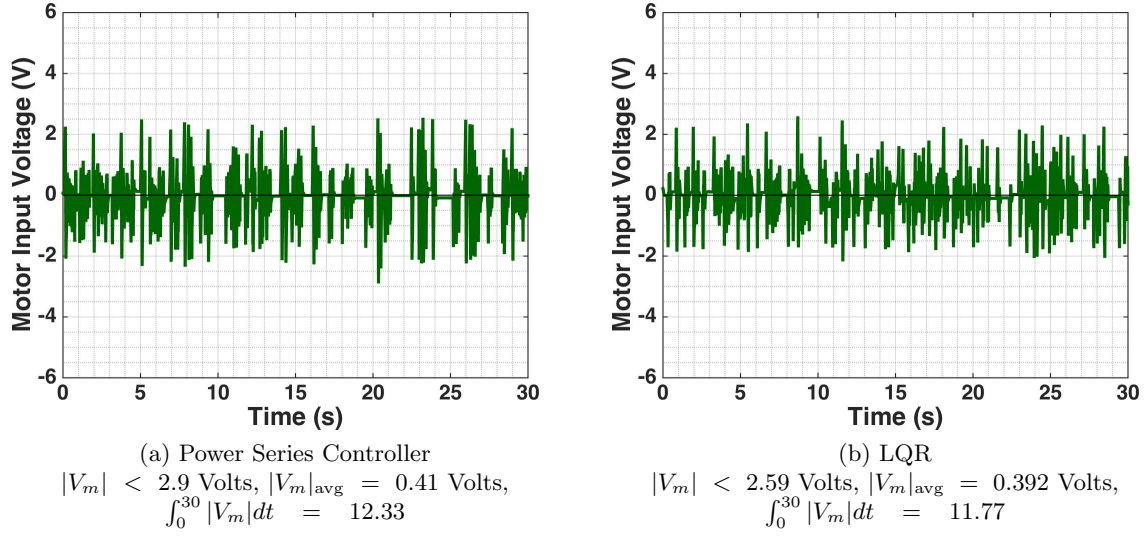


Figure 3.27: Control effort with power series based controller vs. LQR:
 $Q = \text{diag}(800, 150, 1, 1)$ and $R = 0.1$.

3.5.2 State-Dependent Weighting Matrix

The amount of time required for tuning the performance of the power series controller can be significantly reduced by using a state-dependent values in the weighting matrix Q . The choice of $Q(X) = \text{diag}(800 + 5x^2, 150 + 2\alpha^2, 1 + \dot{x}^2, 1 + \dot{\alpha}^2)$ and $R = 0.1$ greatly improves the performance of the controller when compared to the performance of the other two control methods that just use the constant part of $Q(X)$, namely $Q = \text{diag}(800, 150, 1, 1)$. The corresponding control effort and state responses are provided in Figures 3.28 and 3.29. A summary of the analysis of the state responses and the control effort for the three methods is provided in Table 3.3.

Table 3.3: Summary of stabilization state response and control effort for the power series based controller with state-dependent Q vs. controllers with $Q = \text{diag}(800, 150, 1, 1)$.

Method	$ x _{\max}$ $ x _{\text{avg}}$	$ \alpha _{\max}$ $ \alpha _{\text{avg}}$	$ \dot{x} _{\max}$ $ \dot{x} _{\text{avg}}$	$ \dot{\alpha} _{\max}$ $ \dot{\alpha} _{\text{avg}}$	V_{\max}	$ V_m _{\text{avg}}$	$\int_0^{30} V_m dt$
Power Series with state-dependent Q	3.05 mm 0.579 mm	0.176° 2.67e-02°	28.64 mm/s 4.53 mm/s	3.53 deg/s 0.765 deg/s	1.82 V	0.358 V	10.73 V
Power Series with constant Q	3.8 mm 0.775 mm	0.35° 5.08e-02°	67.3 mm/s 7.35 mm/s	10.73 deg/s 1.1 deg/s	2.9 V	0.41 V	12.33 V
LQR	3.19 mm 0.973 mm	0.264° 6.68e-02°	60.6 mm/s 6.82 mm/s	9.19 deg/s 0.99 deg/s	2.59 V	0.392 V	11.77 V

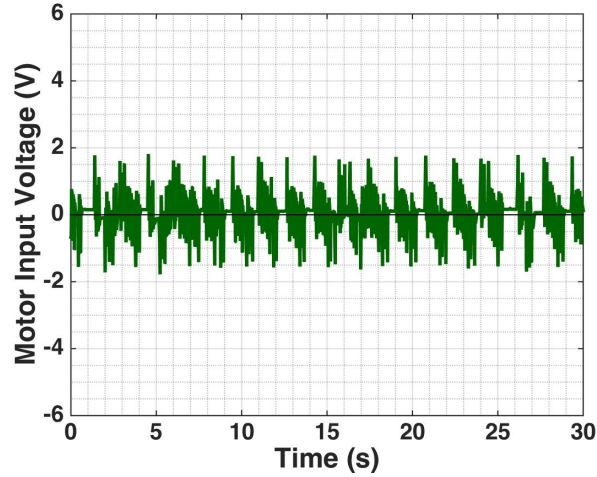
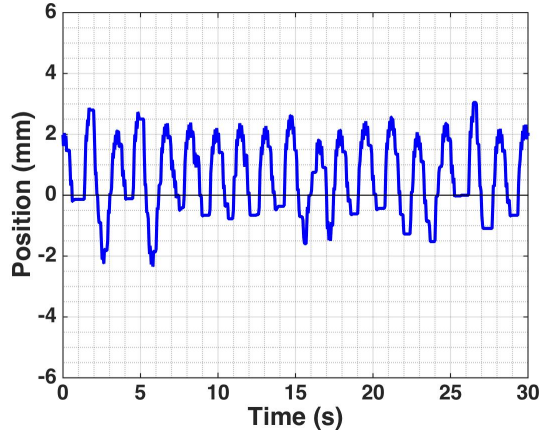
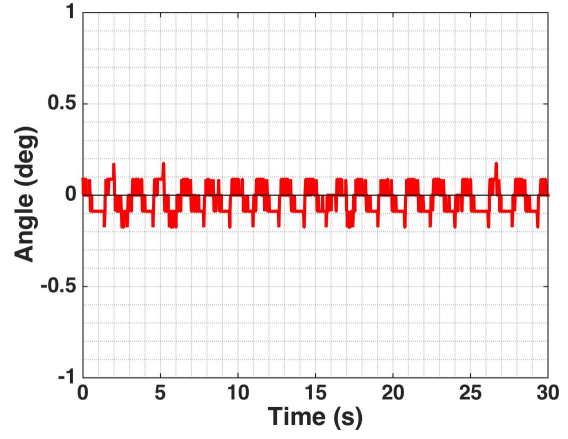


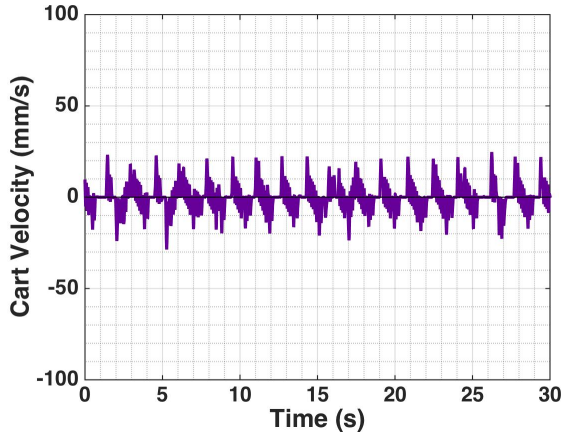
Figure 3.28: Control Effort with power series based controller: $Q(X) = \text{diag}(800 + 5x^2, 150 + 2\alpha^2, 1 + \dot{x}^2, 1 + \dot{\alpha}^2)$ and $R = 0.1$
 $|V_m| < 1.82$ Volts, $|V_m|_{\text{avg}} = 0.358$ Volts, $\int_0^{30} |V_m| = 10.73$.



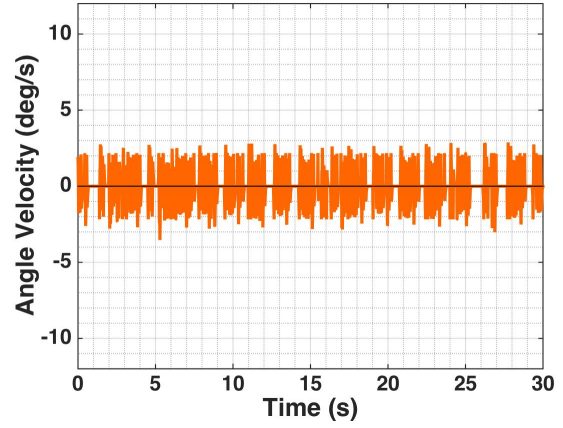
(a) Cart Position
 $|x| < 3.05 \text{ mm}$, $x_{\text{avg}} = 0.579 \text{ mm}$



(b) Pendulum Angle
 $|\alpha| < 0.176^\circ$, $\alpha_{\text{avg}} = 2.67\text{e-}02^\circ$



(c) Cart Velocity
 $|\dot{x}| < 28.64 \text{ mm/s}$, $|\dot{x}|_{\text{avg}} = 4.53 \text{ mm/s}$



(d) Pendulum's Angular Velocity
 $|\dot{\alpha}| < 3.53 \text{ deg/s}$, $|\alpha|_{\text{avg}} = 0.765 \text{ deg/s}$

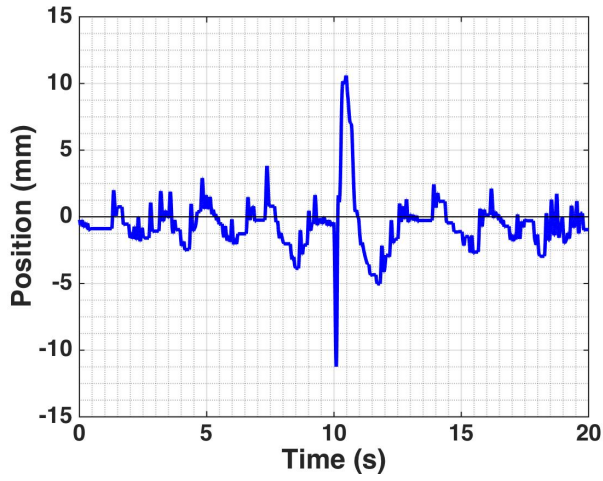
Figure 3.29: State response with power series based controller:
 $Q(X) = \text{diag}(800 + 5x^2, 150 + 2\alpha^2, 1 + \dot{x}^2, 1 + \dot{\alpha}^2)$ and $R = 0.1$.

3.5.3 Disturbance Rejection

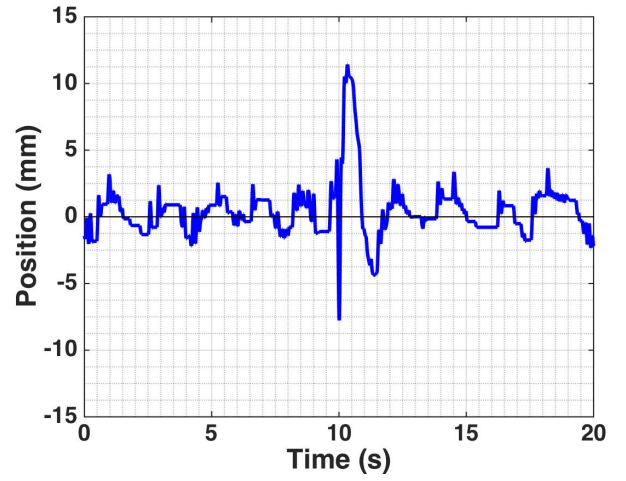
The performance of the power series based controller with both constant and state-dependent Q was compared to the performance of the LQR controller in response to a 1.5° angular pulse disturbance. The three controllers performed very similarly, but the power series controller with state-dependent Q required less voltage than the other two methods. Also notice, that for the power series method with state dependent Q the maximum angular displacement was the same as the introduced disturbance, while the disturbance for the other two methods caused an overcompensated angular displacement in the opposite direction. The corresponding state responses and control effort are provided in Figures 3.30-3.34. A summary of the analysis of the state responses and the control effort in response to a 1.5° angular disturbance for the three methods is provided in Table 3.4.

Table 3.4: Summary of stabilization state response and control effort with 1.5° pulse disturbance.

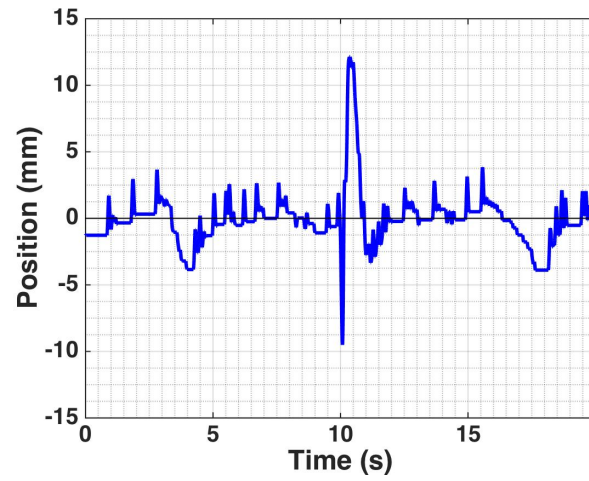
Method	$ x _{\max}$	$ \alpha _{\max}$	$ \dot{x} _{\max}$	$ \dot{\alpha} _{\max}$	V_{\max}
Power Series with state-dependent Q	12.1 mm	1.5°	183.7 mm/s	25.4 deg/s	7.65 Volts
Power Series with constant Q	11.24 mm	1.76°	197.4 mm/s	28 deg/s	8.81 Volts
LQR	11.43 mm	1.85°	181.3 mm/s	26.1 deg/s	8.82 Volts



(a) Power Series with Constant Q , $|x|_{\max} = 11.24$ mm

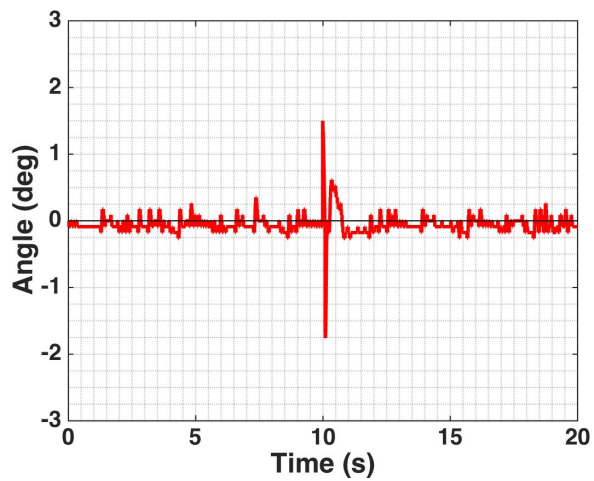


(b) LQR, $|x|_{\max} = 11.43$ mm

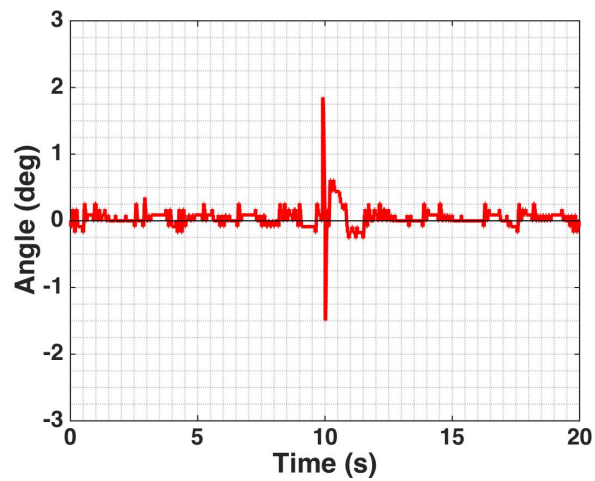


(c) Power Series with State-Dependent Q , $|x|_{\max} = 12.1$ mm

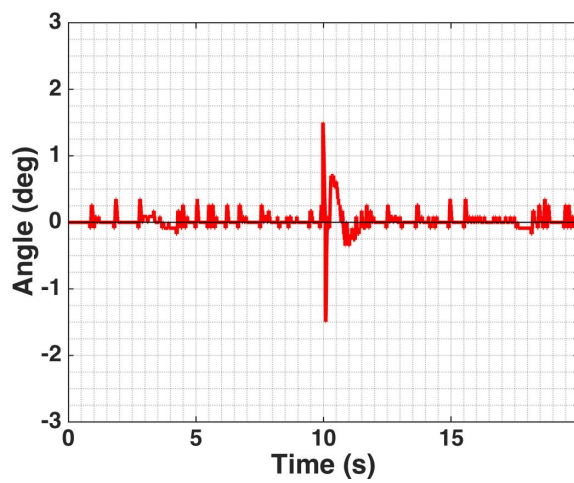
Figure 3.30: Cart position response to 1.5° disturbance.



(a) Power Series with Constant Q , $|\alpha|_{\max} = 1.76^\circ$

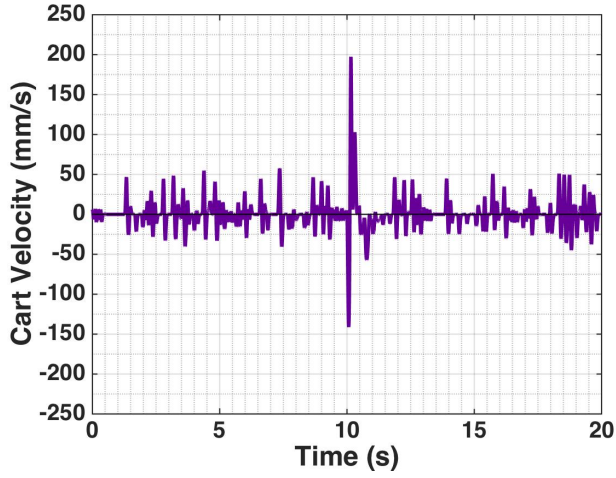


(b) LQR, $|\alpha|_{\max} = 1.85^\circ$

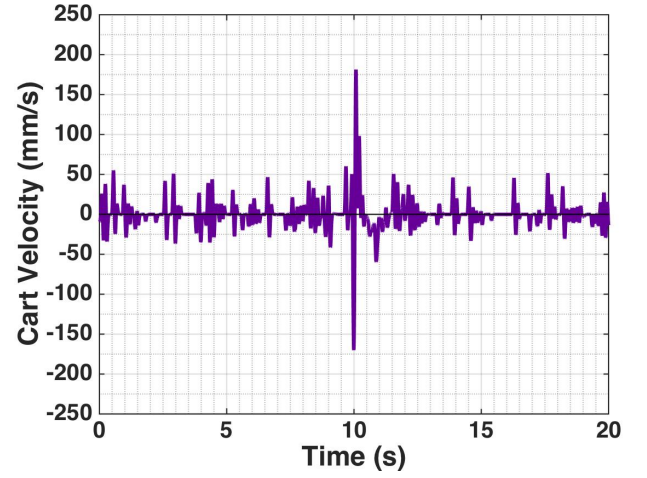


(c) Power Series with State-Dependent Q , $|\alpha|_{\max} = 1.5^\circ$

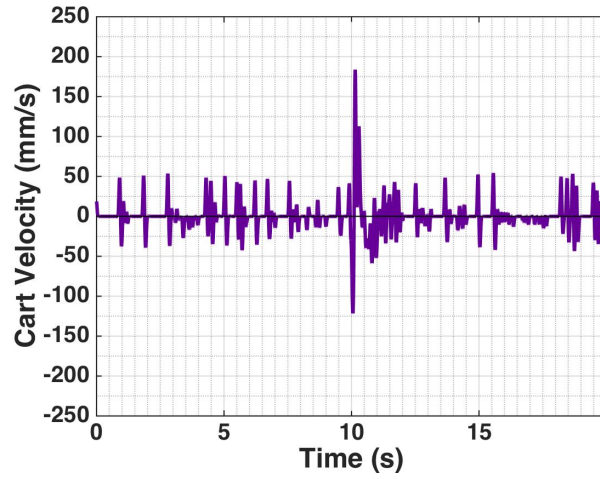
Figure 3.31: Pendulum's angle response to 1.5° disturbance.



(a) Power Series with Constant Q , $|\dot{x}|_{\max} = 197.4$ mm/s

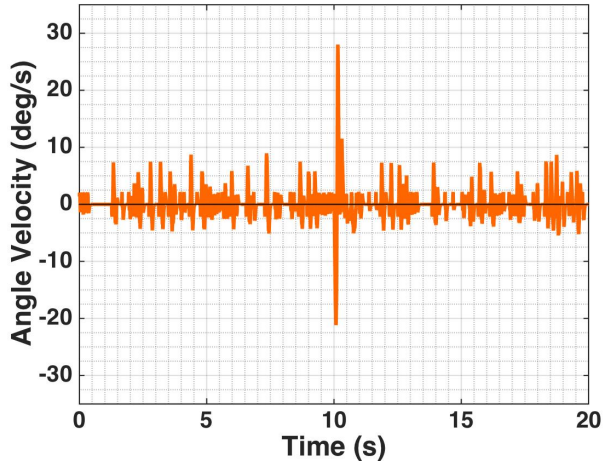


(b) LQR, $|\dot{x}|_{\max} = 181.3$ mm/s

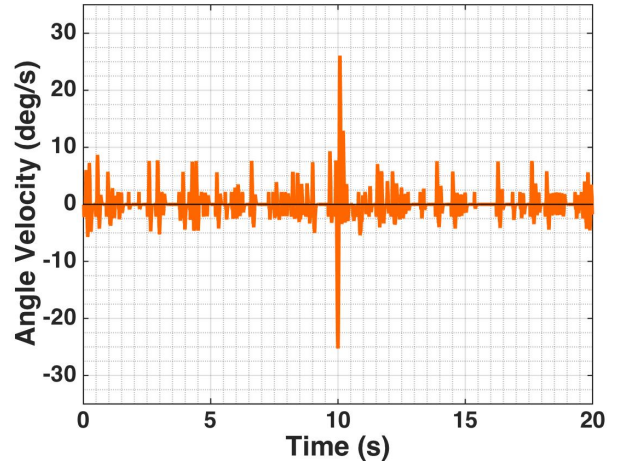


(c) Power Series with State-Dependent Q ,
 $|\dot{x}|_{\max} = 183.7$ mm/s

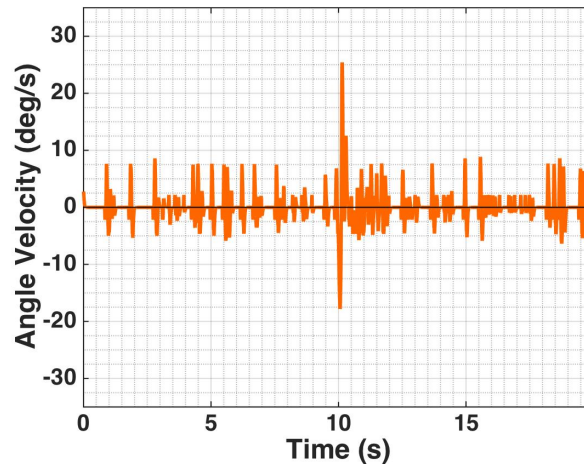
Figure 3.32: Cart velocity response to 1.5° disturbance.



(a) Power Series with Constant Q , $|\dot{\alpha}|_{\max} = 28$ deg/s

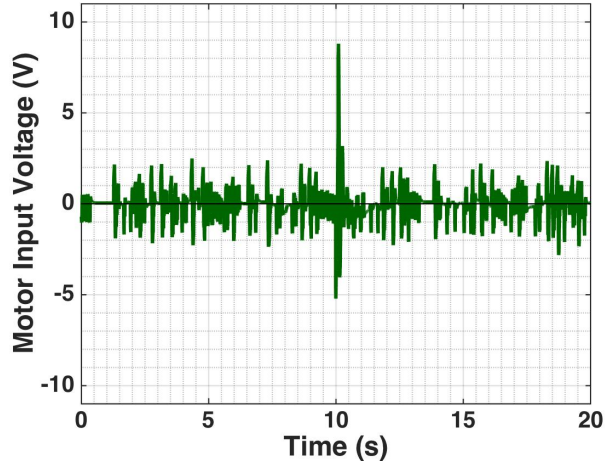


(b) LQR, $|\dot{\alpha}|_{\max} = 26.1$ deg/s

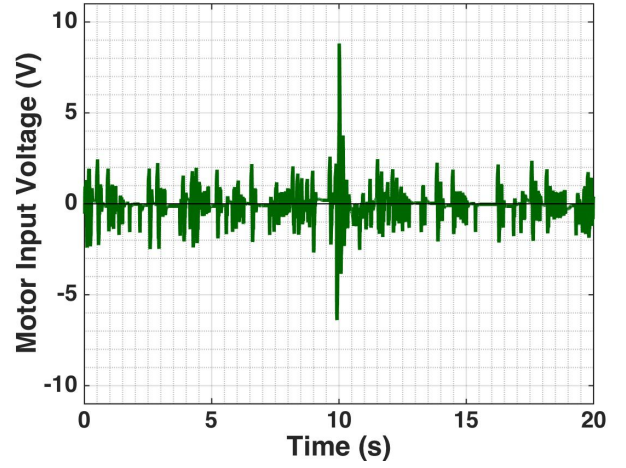


(c) Power Series with State-Dependent Q ,
 $|\dot{\alpha}|_{\max} = 25.4$ deg/s

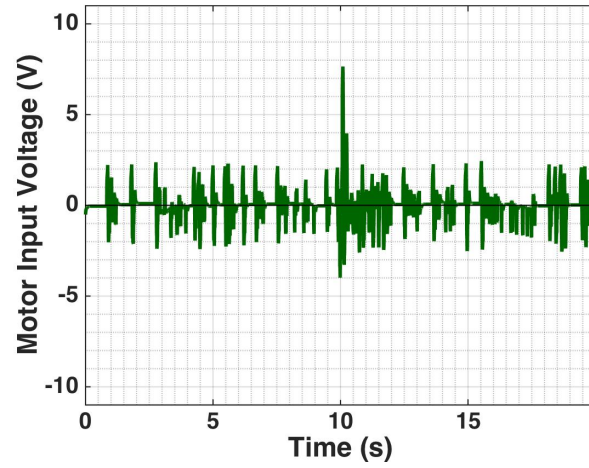
Figure 3.33: Pendulum angular velocity response to 1.5° disturbance.



(a) Power Series with Constant Q , $|V_m|_{\max} = 8.81$ Volts



(b) LQR, $|V_m|_{\max} = 8.82$ Volts



(c) Power Series Controller, $|V_m|_{\max} = 7.65$ Volts

Figure 3.34: Control effort with 1.5° disturbance.

Chapter 4

Swing-up Control

4.1 Energy-based Controller

4.1.1 Pendulum's Energy

One of the most popular control methods for swinging up the pendulum is where the control law is chosen such that the energy of the pendulum builds until reaching the upright equilibrium. This technique was first proposed and implemented by Astrom and Furuta [8, 9]. Here, we present a modified approach using a more complex dynamical model for the SIP system than the simplified model that is most commonly used. We also consider the electrodynamics of the DC motor that drives the cart, incorporate viscous damping friction as seen at the motor pinion, and account for the limitation of having a cart-pendulum system with a finite track length.

The total energy, \mathcal{E}_p , of the pendulum at it's hinge is given by the sum of it's rotational kinetic energy and it's potential energy, so

$$\mathcal{E}_p = \frac{1}{2}J_p\dot{\alpha}^2 + M_p\ell_pg(\cos(\alpha) - 1), \quad (4.1)$$

where J_p , the pendulum's moment of inertia at it's hinge is defined as

$$J_p = \int_0^{2\ell_p} r^2 \frac{M_p}{2\ell_p} dr = \frac{4}{3}M_p\ell_p^2. \quad (4.2)$$

Note that equation (4.1) differs from the energy derived in Section 2.2.1 where we expressed the pendulum's energy at it's center of gravity and not at it's hinge. Since our goal is to increase the energy of the pendulum until the upright position is reach, we must design a controller so that the condition

$$\frac{d\mathcal{E}_p}{dt} \geq 0 \quad (4.3)$$

is guaranteed. By differentiating (4.1) we have

$$\frac{d\mathcal{E}_p}{dt} = J_p\dot{\alpha}\ddot{\alpha} - M_p\ell_pg\sin(\alpha)\dot{\alpha} = \frac{4}{3}M_p\ell_p^2\dot{\alpha}\ddot{\alpha} - M_p\ell_pg\sin(\alpha)\dot{\alpha}. \quad (4.4)$$

Then, using the Lagrange's equation (2.23) we derived earlier, we can rewrite (4.4) as

$$\frac{d\mathcal{E}_p}{dt} = M_p\ell_p\dot{\alpha}\cos(\alpha)\ddot{x}. \quad (4.5)$$

It should be noted, that as is commonly done in swing-up control derivation, the effects of viscous damping at the pendulum axis have been ignored (i.e. set $B_p = 0$). This is acceptable because B_p is very small and its effect is minor.

4.1.2 Converting to Voltage Input

In most swing-up derivations, the control input is taken to be the acceleration of the cart, \ddot{x} , but for our real-time implementation the control input is defined to be the voltage applied to the cart V_m . Thus, we need to express \ddot{x} in terms of V_m . We will do this by considering Newton's second law of motion together with D'Alembert's principle¹,

$$M\ddot{x} + F_{ai} = F_c - B_{eq}\dot{x}, \quad (4.6)$$

where F_{ai} is the armature rotational inertial force acting on the cart [65]. As seen at the motor pinion, F_{ai} can be expressed as a function of the armature inertial torque, T_{ai} , thus

$$F_{ai} = \frac{K_g T_{ai}}{r_{mp}}. \quad (4.7)$$

Now, applying Newton's second law of motion to the shaft of the cart's DC motor yields

$$J_m\ddot{\theta}_m = T_{ai}, \quad (4.8)$$

where θ_m is the rotational angle of the motor shaft. Using the mechanical configuration of the cart's rack-pinion system and the technical specifications from the Quanser IP02 User Manual [63], as well as the study of the electrodynamics of a DC motor in [61] we have

$$\theta_m = \frac{K_g x}{r_{mp}}. \quad (4.9)$$

¹The sum of differences between the forces acting on a system of mass particles and the time derivatives of the moment of inertia of the system itself along any virtual displacement consistent with constraints of the system, is zero.

Then, we can substitute equations (4.9) and (4.8) into (4.7) to obtain

$$F_{ai} = \frac{K_g^2 J_m \ddot{x}}{r_{mp}}. \quad (4.10)$$

With the use of equations (2.32) and (4.10), we can express (4.6) as

$$\left(M + \frac{K_g^2 J_m}{r_{mp}^2} \right) \ddot{x} = - \left(B_{eq} + \frac{K_g^2 K_t K_m}{R_m r_{mp}^2} \right) \dot{x} + \frac{K_g K_t V_m}{R_m r_{mp}}. \quad (4.11)$$

Solving for \ddot{x} results in

$$\ddot{x} = \frac{K_g K_t r_{mp} V_m - (K_g^2 K_t K_m + B_{eq} R_m r_{mp}^2) \dot{x}}{R_m (M r_{mp}^2 + K_g^2 J_m)}. \quad (4.12)$$

Therefore, by substituting (4.12) into (4.5) and imposing the condition in (4.3), we obtain that our control input, V_m , must satisfy

$$\frac{d\mathcal{E}_p}{dt} = M_p \ell_p \dot{\alpha} \cos(\alpha) \left(\frac{K_g K_t r_{mp} V_m - (K_g^2 K_t K_m + B_{eq} R_m r_{mp}^2) \dot{x}}{R_m (M r_{mp}^2 + K_g^2 J_m)} \right) \geq 0. \quad (4.13)$$

4.1.3 Lyapunov Stability Condition

Consider the Lyapunov function

$$L(X) = \frac{1}{2} (\mathcal{E}_p)^2, \quad (4.14)$$

which is defined to be zero when the pendulum is in its upright position, and positive everywhere else. Then, based on Lyapunov's theorem, we must have

$$\frac{dL}{dt} = \mathcal{E}_p \frac{d\mathcal{E}_p}{dt} = \mathcal{E}_p M_p \ell_p \dot{\alpha} \cos(\alpha) \left(\frac{K_g K_t r_{mp} V_m - (K_g^2 K_t K_m + B_{eq} R_m r_{mp}^2) \dot{x}}{R_m (M r_{mp}^2 + K_g^2 J_m)} \right) \leq 0. \quad (4.15)$$

Substituting the model parameter values provided in Appendix A.2 into (4.15) and simplifying yields the condition

$$\mathcal{E}_p \dot{\alpha} \cos(\alpha) (V_m - 7.614 \dot{x}) \leq 0. \quad (4.16)$$

Consider the control law of the form

$$V_m(X) = \beta |\dot{x}| (-\text{sign}(\mathcal{E}_p \dot{\alpha} \cos(\alpha)) + \text{sg}(X) e^{\eta |x|}), \quad (4.17)$$

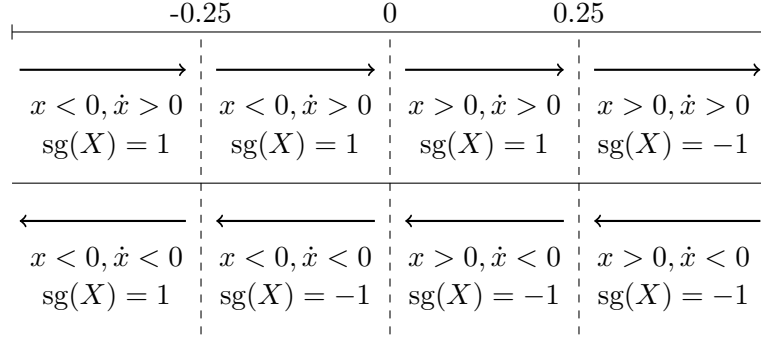


Figure 4.1: Diagram representing how $\text{sg}(X)$ is defined. The arrows indicate the direction of the cart's displacement, while the number line indicates the cart's position.

where β and η are positive constants, sign represents the signum function, and the function $\text{sg}(X)$ is defined as

$$\text{sg}(X) = 0.5(\text{sign}(\dot{x}) - \text{sign}(x) - \text{sign}(|x| - 0.25)(\text{sign}(\dot{x}) + \text{sign}(x))), \quad (4.18)$$

which will output ± 1 depending on the position of the cart and direction it is moving. Then, the sign of V_m will be the same as the sign of $\text{sg}(X)$ because of the exponential term in (4.17). The total length of the track that the cart can travel is 0.814 m, indicating that the cart's horizontal displacement in either direction must be less than 0.407 m (i.e. $|x| < 0.407$ m). For safety reasons, the cart should not get too close to the end of the track, thus $\text{sg}(X)$ was defined in such a way that it switches signs only when the cart's displacement from the center is more than 0.25 m and the direction of the cart's displacement is towards either track end. Figure 4.1 represents how $\text{sg}(X)$ is defined. Substituting (4.17) into (4.16) gives

$$\mathcal{E}_p \dot{\alpha} \cos(\alpha) \left(\beta |\dot{x}| \left(-\text{sign}(\mathcal{E}_p \dot{\alpha} \cos(\alpha)) + \text{sg}(X) e^{\eta|x|} \right) - 7.614 \dot{x} \right) \leq 0, \quad (4.19)$$

which can be rewritten as

$$\beta |\dot{x}| (\text{sg}(X) \mathcal{E}_p \dot{\alpha} \cos(\alpha) e^{\eta|x|} - |\mathcal{E}_p \dot{\alpha} \cos(\alpha)|) \leq 7.614 \dot{x} \mathcal{E}_p \dot{\alpha} \cos(\alpha). \quad (4.20)$$

Then, dividing by $|\dot{x}| |\mathcal{E}_p \dot{\alpha} \cos(\alpha)|$ yields

$$\beta \left(\text{sign}(\mathcal{E}_p \dot{\alpha} \cos(\alpha)) \text{sg}(X) e^{\eta|x|} - 1 \right) \leq 7.614 \text{sign}(\mathcal{E}_p \dot{\alpha} \cos(\alpha)) \text{sign}(\dot{x}). \quad (4.21)$$

Physically for our system, a positive input voltage means positive cart displacement, therefore V_m and \dot{x} have the same sign. Furthermore, since we defined $\text{sg}(X)$ to have the same sign as V_m , this also means that $\text{sg}(X)$ and \dot{x} must also have the same sign. Now, consider the possible

sign combinations for $\mathcal{E}_p \dot{\alpha} \cos(\alpha)$ and sg :

- Case 1: $\mathcal{E}_p \dot{\alpha} \cos(\alpha) > 0$ and $\text{sg}(X) = 1$ ($\dot{x} > 0$)

$$\beta \left(e^{\eta|x|} - 1 \right) \leq 7.614 \Rightarrow \beta \leq \frac{7.614}{e^{\eta|x|} - 1}.$$

- Case 2: $\mathcal{E}_p \dot{\alpha} \cos(\alpha) > 0$ and $\text{sg}(X) = -1$ ($\dot{x} < 0$)

$$\beta \left(-e^{\eta|x|} - 1 \right) \leq -7.614 \Rightarrow \beta \geq \frac{7.614}{e^{\eta|x|} + 1}.$$

- Case 3: $\mathcal{E}_p \dot{\alpha} \cos(\alpha) < 0$ and $\text{sg}(X) = 1$ ($\dot{x} > 0$)

$$\beta \left(-e^{\eta|x|} - 1 \right) \leq -7.614 \Rightarrow \beta \geq \frac{7.614}{e^{\eta|x|} + 1}.$$

- Case 4: $\mathcal{E}_p \dot{\alpha} \cos(\alpha) < 0$ and $\text{sg}(X) = -1$ ($\dot{x} < 0$)

$$\beta \left(e^{\eta|x|} - 1 \right) \leq 7.614 \Rightarrow \beta \leq \frac{7.614}{e^{\eta|x|} - 1}.$$

Based on the above cases, we obtain that β and η must satisfy the condition

$$\frac{7.614}{e^{\eta|x|} + 1} \leq \beta \leq \frac{7.614}{e^{\eta|x|} - 1}. \quad (4.22)$$

Moreover, we have to ensure that the commanded voltage does not make the power amplifier go into saturation, so we must design our control in a way that $|V_m| < 10$ Volts. This means that β and η also have to satisfy

$$\left| \beta |\dot{x}| \left(-\text{sign}(\mathcal{E}_p \dot{\alpha} \cos(\alpha)) + \text{sg}(X) e^{\eta|x|} \right) \right| \leq 10. \quad (4.23)$$

We can easily find a bound for (4.23) only in terms of β and η since we can calculate that maximum velocity of the cart based on technical specifications provided in [63]. The maximum speed of the DC motor is $\omega_{\max} = 628.3$ rad/s. Substituting this value into equations (2.4) and (2.5) we obtain that the maximum velocity of the cart is 1.075 m/s. One particular choice for β and η that satisfies all of the above conditions is $\beta = 4$ and $\eta = 0.9$.

4.1.4 Simulation Results

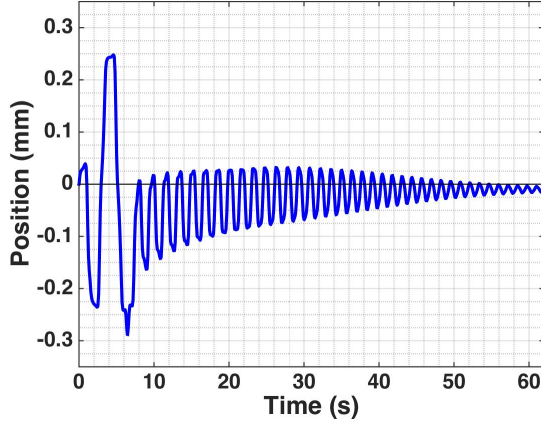
The presented controller given by (4.17) was tested in simulation with $\beta = 4$ and $\eta = 0.9$ using the Simulink diagrams provided in B.5 with the IP02 + SESIP Actual Plant subsystem

block replaced by the SIP EOM with Friction subsystem block from the diagram in Figure B.6. The state responses and the corresponding control effort are graphed in Figure 4.2. The dashed blue lines in 4.2b indicate the region where the stabilization control can take over (i.e. where $|\alpha| < 15^\circ$). The simulation indicates that the controller swings the pendulum up into the upright position in less than one minute. More importantly, all the values of the states and the required control effort stayed within the possible ranges deliverable by the apparatus we will use for real time experiments.

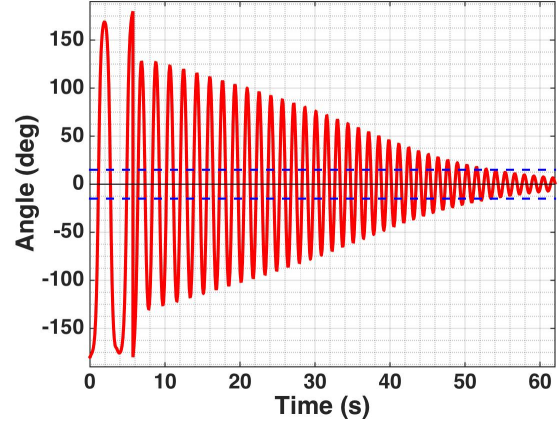
4.1.5 Experimental Results

The swing-up controller given by (4.17) was successfully implemented in real-time $\beta = 4$ and $\eta = 0.9$ using the MATLAB Simulink model provided in Appendix B.5. Since the starting downward position of the pendulum is a stable equilibrium we must input a small amount of initial voltage to get the experiment started. The state responses and the corresponding control effort are graphed in Figure 4.3. Figure 4.3b indicates that the controller swung up the pendulum in approximately 45 seconds. On one occasion the required control effort reached the upper limit of 10 Volts and had to be saturated. However, the average amount of voltage used during the experiment was only about 1.35 Volts. Once the pendulum reached within 15° of the upright position, the power series based stabilization controller successfully took over. The switching was achieved by the Mode Switching Simulink block provided by Quanser.

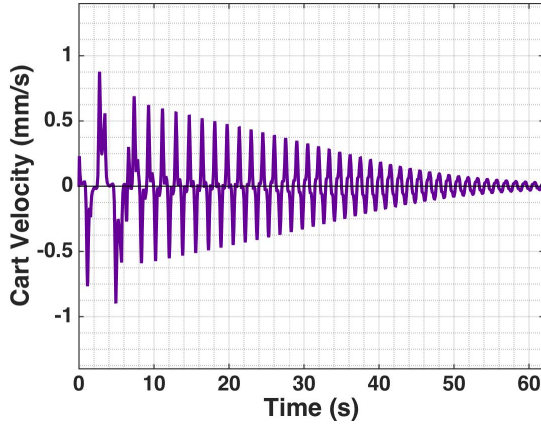
Even though we have been able to achieve successful swing-up using the controller derived in Section 4.1.3, this has not been the case for every experimental run. There have been some instances when instead of swinging up to the upright position, the pendulum ended up swinging back and forth at a constant rate without building up more energy. In the next section, we discuss a possible reasons for this phenomena and propose a modifications to the presented swing-up controller in (4.17).



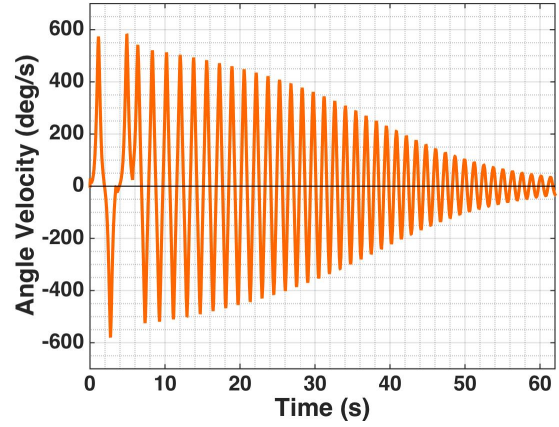
(a) Cart Position, $|x| < 0.29$ m



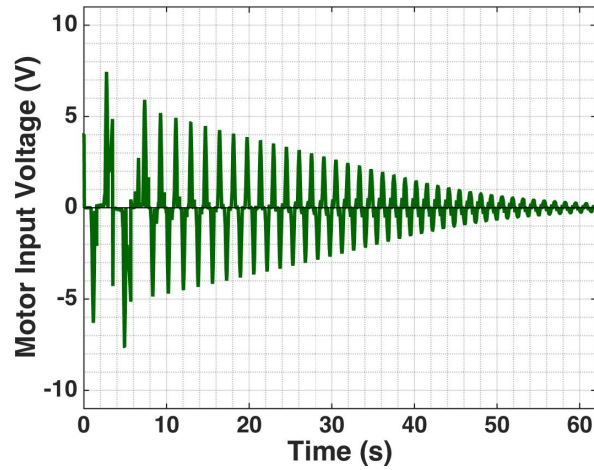
(b) Pendulum Angle



(c) Cart Velocity, $|\dot{x}| < 0.897$ m/s

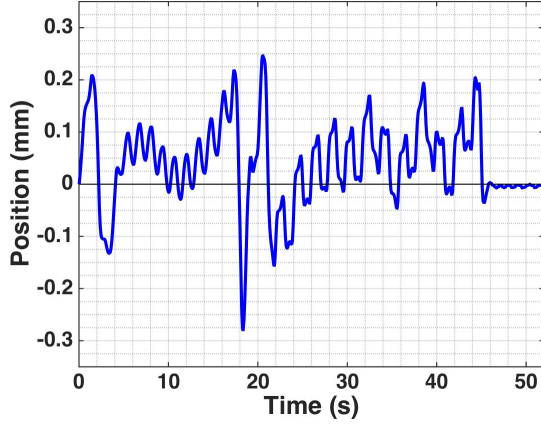


(d) Pendulum's Angular Velocity, $|\dot{\alpha}| < 583$ deg/s

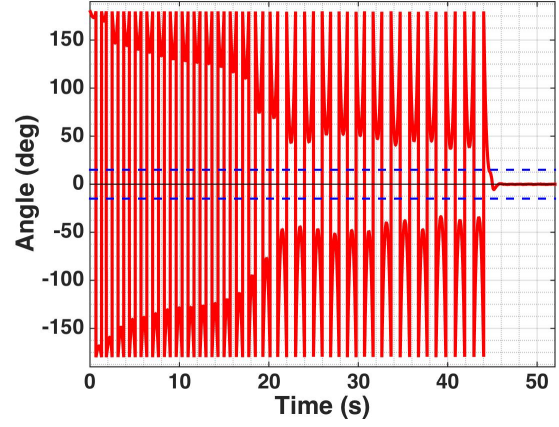


(e) Control Effort, $|V_m| < 7.64$, $|V_m|_{\text{avg}} = 0.83$ Volts

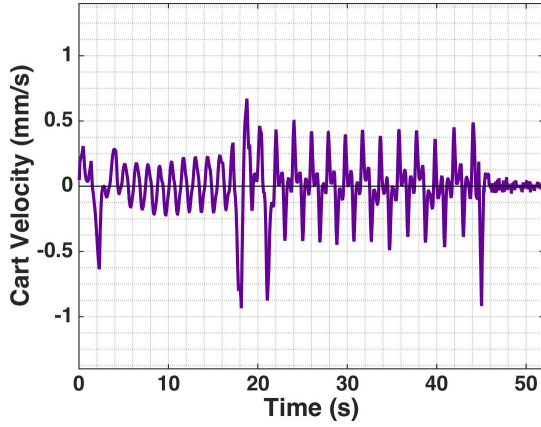
Figure 4.2: Simulated state response and control effort for the energy based swing up controller given by equation (4.17) with $\beta = 4$ and $\eta = 0.9$.



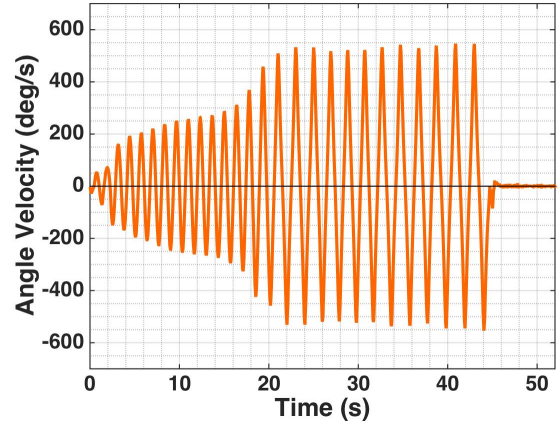
(a) Cart Position, $|x| < 0.281$ m



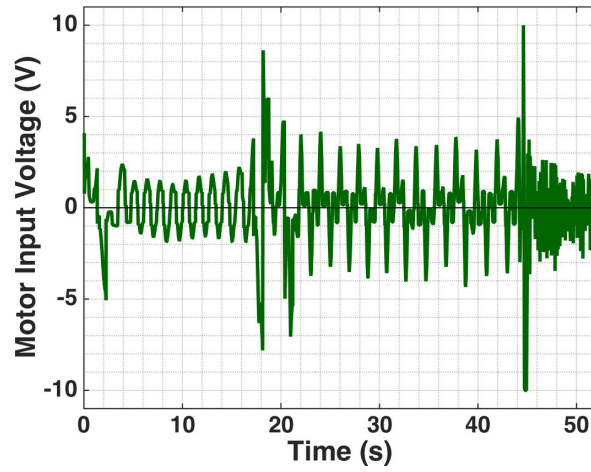
(b) Pendulum Angle



(c) Cart Velocity, $|\dot{x}| < 0.936$ m/s



(d) Pendulum's Angular Velocity, $|\dot{\alpha}| < 554$ deg/s



(e) Control Effort, $|V_m| \leq 10$ Volts, $|V_m|_{\text{avg}} = 1.35$ Volts

Figure 4.3: Experimental state response and control effort for the energy based swing up controller given in equation (4.17) with $\beta = 4$ and $\eta = 0.9$.

4.2 More Robust Swing-up Controller

4.2.1 Modified Lyapunov Function

Even though most publications on energy-based control methods for the swing-up of the pendulum use the same Lyapunov function we used in equation (4.14) for their derivation, in [50] Maeba et al. point out that this function has several zeros aside from the upright position. In fact, the pendulum's energy (4.1), and thus the Lyapunov function in (4.14), is zero every time the pendulum's angle and angular velocity satisfy

$$\dot{\alpha} = \pm \sqrt{\frac{3g(1 - \cos(\alpha))}{2\ell_p}}. \quad (4.24)$$

This means that the presented controller is not guaranteed to swing the pendulum up since the energy will stop building once the desired zero energy is achieved. To fix this problem, consider the Lyapunov function

$$L_2(X) = \frac{1}{2}\mathcal{E}_p^2 + k(1 - \cos^3(\alpha)), \quad (4.25)$$

where k is a positive constant. Equation (4.25) only has one zero, namely the upright position with zero angular velocity (i.e. $\alpha = 0, \dot{\alpha} = 0$), and is strictly positive everywhere else. Differentiating (4.25) and utilizing (4.15) we obtain the new Lyapunov condition

$$\frac{dL_2}{dt} = \mathcal{E}_p M_p \ell_p \dot{\alpha} \cos(\alpha) \left(\frac{K_g K_t r_{mp} V_m - (K_g^2 K_t K_m + B_{eq} R_m r_{mp}^2) \dot{x}}{R_m (M r_{mp}^2 + K_g^2 J_m)} \right) + \frac{3}{2} k \cos(\alpha) \sin(2\alpha) \dot{\alpha} \leq 0. \quad (4.26)$$

Substituting the model parameter values provided in Appendix A.2 into (4.26) yields the new condition

$$\mathcal{E}_p \dot{\alpha} \cos(\alpha) (V_m - 7.614 \dot{x}) + 12.28 k \dot{\alpha} \cos(\alpha) \sin(2\alpha) \leq 0, \quad (4.27)$$

that the control input, V_m must satisfy. Consider the control law of the form

$$V_m(X) = \beta_1 |\dot{x}| \left(-\beta_2 \text{sign}(\mathcal{E}_p \dot{\alpha} \cos(\alpha)) + \text{sg}(X) e^{\eta|x|} \right) - \frac{\beta_3 \text{sign}(\dot{\alpha} \cos(\alpha)) |\sin(2\alpha)|}{\mathcal{E}_p}, \quad (4.28)$$

where β_1, β_3 , and η are positive constants, $1 > \beta_2 > 0$, and sg is the same function defined in (4.18). Note that equation (4.28) is a modification of the previously presented control law in

(4.17). Substituting (4.28) into (4.27) gives

$$\begin{aligned} & \mathcal{E}_p \dot{\alpha} \cos(\alpha) \left(\beta_1 |\dot{x}| \left(-\beta_2 \text{sign}(\mathcal{E}_p \dot{\alpha} \cos(\alpha)) + \text{sg}(X) e^{\eta|x|} \right) - 7.614 \dot{x} \right) \\ & - \beta_3 |\dot{\alpha} \cos(\alpha)| |\sin(2\alpha)| + 12.28k \dot{\alpha} \cos(\alpha) \sin(2\alpha) \\ & \leq 0. \end{aligned} \quad (4.29)$$

The above inequality is satisfied when

$$\mathcal{E}_p \dot{\alpha} \cos(\alpha) \left(\beta_1 |\dot{x}| \left(-\beta_2 \text{sign}(\mathcal{E}_p \dot{\alpha} \cos(\alpha)) + \text{sg}(X) e^{\eta|x|} \right) - 7.614 \dot{x} \right) \leq 0, \quad (4.30)$$

and

$$- \beta_3 |\dot{\alpha} \cos(\alpha)| |\sin(2\alpha)| + 12.28k \dot{\alpha} \cos(\alpha) \sin(2\alpha) \leq 0 \quad (4.31)$$

are both satisfied. Based on our earlier conditions in (4.21) and (4.22), we can obtain that (4.30) holds when

$$\frac{7.614}{e^{\eta|x|} + \beta_2} \leq \beta_1 \leq \frac{7.614}{e^{\eta|x|} - \beta_2}. \quad (4.32)$$

Furthermore, inequality (4.31) is satisfied when

$$\beta_3 \geq 12.28k. \quad (4.33)$$

In addition to the conditions (4.32) and (4.33), the sign of V_m should be given by the value of $\text{sg}(X)$ to make sure the cart avoids the edges of the track. Therefore, we must have

$$\text{sign} \left(\beta_1 |\dot{x}| \left(-\beta_2 \text{sign}(\mathcal{E}_p \dot{\alpha} \cos(\alpha)) + \text{sg}(X) e^{\eta|x|} \right) - \frac{\beta_3 \text{sign}(\dot{\alpha} \cos(\alpha)) |\sin(2\alpha)|}{\mathcal{E}_p} \right) = \text{sg}(X). \quad (4.34)$$

Now, consider the possible sign combinations for $\mathcal{E}_p \dot{\alpha} \cos(\alpha)$ and sg :

- Case 1: $\mathcal{E}_p \dot{\alpha} \cos(\alpha) > 0$ and $\text{sg}(X) = 1$ (i.e. want $V_m > 0$, $\dot{x} > 0$)

$$\beta_1 |\dot{x}| \left(-\beta_2 + e^{\eta|x|} \right) - \frac{\beta_3 |\sin(2\alpha)|}{|\mathcal{E}_p|} > 0 \Rightarrow \beta_1 > \frac{\beta_3 |\sin(2\alpha)|}{|\dot{x}| |\mathcal{E}_p| (e^{\eta|x|} - \beta_2)}.$$

- Case 2: $\mathcal{E}_p \dot{\alpha} \cos(\alpha) > 0$ and $\text{sg}(X) = -1$ (i.e. want $V_m < 0$, $\dot{x} < 0$)

$$\beta_1 |\dot{x}| \left(-\beta_2 - e^{\eta|x|} \right) - \frac{\beta_3 |\sin(2\alpha)|}{|\mathcal{E}_p|} < 0 \Rightarrow \beta_1 > -\frac{\beta_3 |\sin(2\alpha)|}{|\dot{x}| |\mathcal{E}_p| (e^{\eta|x|} + \beta_2)}.$$

- Case 3: $\mathcal{E}_p \dot{\alpha} \cos(\alpha) < 0$ and $\text{sg}(X) = 1$ (i.e. want $V_m > 0$, $\dot{x} > 0$)

$$\beta_1 |\dot{x}| \left(\beta_2 + e^{\eta|x|} \right) + \frac{\beta_3 |\sin(2\alpha)|}{|\mathcal{E}_p|} > 0 \Rightarrow \beta_1 > -\frac{\beta_3 |\sin(2\alpha)|}{|\dot{x}| |\mathcal{E}_p| (e^{\eta|x|} + \beta_2)}.$$

- Case 4: $\mathcal{E}_p \dot{\alpha} \cos(\alpha) < 0$ and $\text{sg}(X) = -1$ (i.e. want $V_m < 0$, $\dot{x} < 0$)

$$\beta_1 |\dot{x}| \left(\beta_2 - e^{\eta|x|} \right) + \frac{\beta_3 |\sin(2\alpha)|}{|\mathcal{E}_p|} < 0 \Rightarrow \beta_1 > \frac{\beta_3 |\sin(2\alpha)|}{|\dot{x}| |\mathcal{E}_p| (e^{\eta|x|} - \beta_2)}.$$

The above cases all hold when the constants $\beta_1, \beta_2, \beta_3$, and η satisfy

$$\beta_1 > \frac{\beta_3 |\sin(2\alpha)|}{|\dot{x}| |\mathcal{E}_p| (e^{\eta|x|} - \beta_2)}. \quad (4.35)$$

To avoid division by zero and bound the value of β_1 , we can saturate the signals of \mathcal{E}_p and \dot{x} so that $|\mathcal{E}_p| > \delta_1$ and $|\dot{x}| > \delta_2$ for some small positive constants δ_1 and δ_2 . Then, the condition (4.35) will be satisfied when

$$\beta_1 \geq \frac{\beta_3}{\delta_1 \delta_2 (1 - \beta_2)}. \quad (4.36)$$

Moreover, to avoid saturation of the power amplifier, the constants in (4.28) must be chosen so that

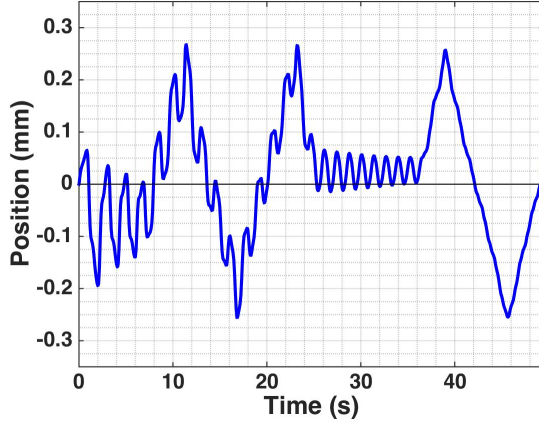
$$|V_m| = \left| \beta_1 |\dot{x}| \left(-\beta_2 \text{sign}(\mathcal{E}_p \dot{\alpha} \cos(\alpha)) + \text{sg}(X) e^{\eta|x|} \right) - \frac{\beta_3 \text{sign}(\dot{\alpha} \cos(\alpha)) |\sin(2\alpha)|}{\mathcal{E}_p} \right| \leq 10, \quad (4.37)$$

where the maximum possible value of \dot{x} , as previously calculated, is 1.075 m/s. The choice of the constants in the control law that satisfy all the restrictions is somewhat arbitrary. One possible choice that satisfies all conditions and yields satisfactory simulation results is $\beta_1 = 5.1$, $\beta_2 = 0.5$, $\beta_3 = 0.002$, and $\eta = 0.8$. These constants were calculated using $k = 10^{-4}$, $\delta_1 = 0.001$, and $\delta_2 = 0.1$.

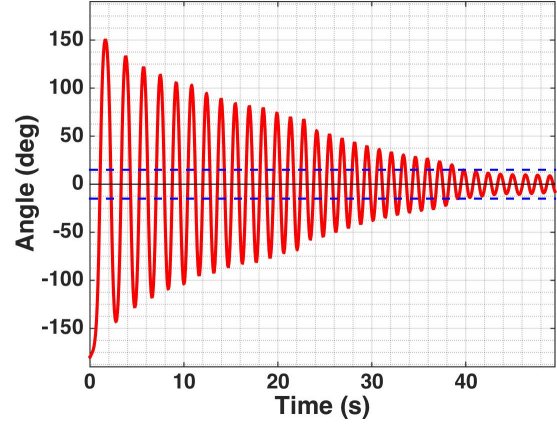
4.2.2 Simulation Results

The controller given by (4.28) was tested in simulation with $\beta_1 = 5.1$, $\beta_2 = 0.5$, $\beta_3 = 0.002$, $\eta = 0.8$, $\delta_1 = 0.001$, and $\delta_2 = 0.1$ using the Simulink diagrams given in Appendix B.5 with the IP02 + SESIP Actual Plant subsystem block replaced by the SIP EOM with Friction subsystem block from the diagram in Figure B.6. The state responses and the corresponding control effort are graphed in Figure 4.4. The dashed blue lines in 4.4b indicate the region where the stabilization control can take over (i.e. where $|\alpha| < 15^\circ$). The simulation indicates that the controller swings the pendulum up into the upright position in approximately 40 seconds,

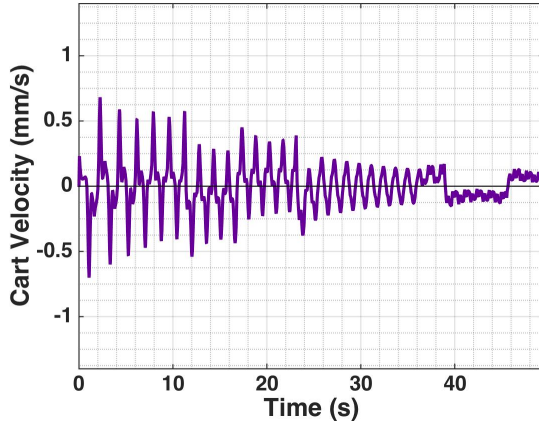
which is about 10 seconds faster than the previous method. More importantly, all the values of the states and the required control effort stayed within the possible ranges deliverable by the apparatus we use for real time experiments. Figure 4.4a also indicates that the cart did not go past the end of the track.



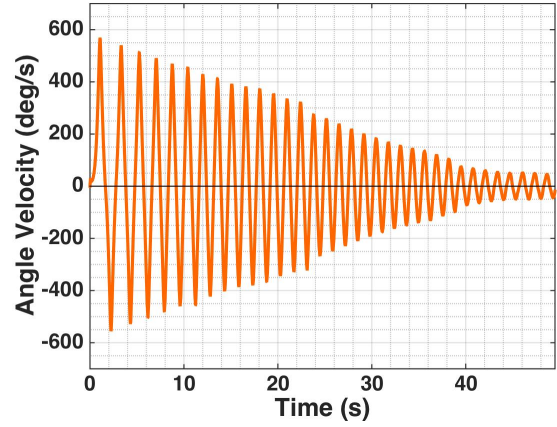
(a) Cart Position, $|x| < 0.269$ m



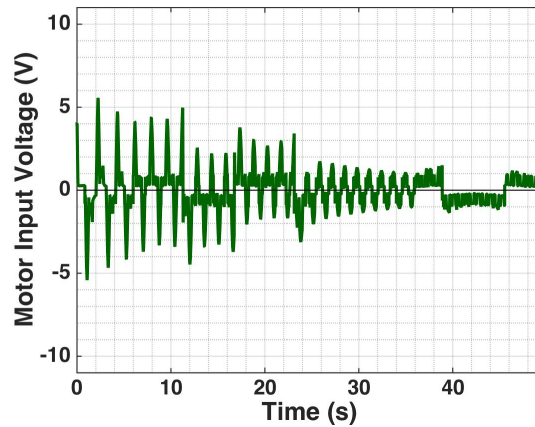
(b) Pendulum Angle



(c) Cart Velocity, $|\dot{x}| < 0.701$ m/s



(d) Pendulum's Angular Velocity, $|\dot{\alpha}| < 570$ deg/s



(e) Control Effort, $|V_m| < 5.57$
Volts, $|V_m|_{\text{avg}} = 0.978$ Volts

Figure 4.4: Simulated state response and control effort for the more robust swing up controller given by equation (4.28).

4.3 Incorporating Viscous Damping at the Pendulum Axis

The two swing-up methods presented so far in the previous sections have accounted for viscous damping friction as seen at the cart's motor pinion, but they have ignored the effects of viscous damping as seen at the pendulum axis. Though the effect of the viscous damping term, $B_p\dot{\alpha}$, in equation (2.23) is small, it is desirable for real-time experiments and some applications to use a more complete model. In this section, we present another modification for our previous swing-up controllers to include viscous damping at the pendulum axis. If we include the $B_p\dot{\alpha}$ from (2.23), then equation (4.5) becomes

$$\frac{d\mathcal{E}_p}{dt} = M_p\ell_p\dot{\alpha}\cos(\alpha)\ddot{x} - B_p\dot{\alpha}^2, \quad (4.38)$$

which can be rewritten as

$$\frac{d\mathcal{E}_p}{dt} = M_p\ell_p\dot{\alpha}\cos(\alpha) \left(\frac{K_g K_t r_{mp} V_m - (K_g^2 K_t K_m + B_{eq} R_m r_{mp}^2) \dot{x}}{R_m (M r_{mp}^2 + K_g^2 J_m)} \right) - B_p \dot{\alpha}^2 \quad (4.39)$$

using equation (4.12). Then, using the modified Lyapunov function given in (4.25), and adding the viscous term into the derivate, we can modify (4.26) to obtain the new condition

$$\begin{aligned} \frac{dL_2}{dt} &= \mathcal{E}_p M_p \ell_p \dot{\alpha} \cos(\alpha) \left(\frac{K_g K_t r_{mp} V_m - (K_g^2 K_t K_m + B_{eq} R_m r_{mp}^2) \dot{x}}{R_m (M r_{mp}^2 + K_g^2 J_m)} \right) \\ &\quad + \frac{3}{2} k \cos(\alpha) \sin(2\alpha) \dot{\alpha} - \mathcal{E}_p B_p \dot{\alpha}^2 \\ &\leq 0. \end{aligned} \quad (4.40)$$

Substituting the model parameter values provided in Appendix A.2 into (4.40), and simplifying yields the condition

$$\mathcal{E}_p \dot{\alpha} \cos(\alpha) (V_m - 7.614\dot{x}) + 12.28k\dot{\alpha} \cos(\alpha) \sin(2\alpha) - 0.0197\mathcal{E}_p \dot{\alpha}^2 \leq 0, \quad (4.41)$$

that our modified controller must satisfy to guarantee Lyapunov stability. To account for the effect of the damping term, consider the control law of the form

$$\begin{aligned} V_m(X) &= \beta_1 |\dot{x}| \left(-\beta_2 \text{sign}(\mathcal{E}_p \dot{\alpha} \cos(\alpha)) + \text{sg}(X) e^{\eta|x|} \right) - \frac{\beta_3 \text{sign}(\dot{\alpha} \cos(\alpha)) |\sin(2\alpha)|}{\mathcal{E}_p} \\ &\quad + 0.0197 \text{sign}(\mathcal{E}_p) \dot{\alpha} \cos \alpha, \end{aligned} \quad (4.42)$$

which is just a modification of (4.28) with positive constants, β_1 , β_3 , η , and $0 < \beta_2 < 1$. Substituting (4.42) into (4.41), and simplifying results in

$$\begin{aligned} & \mathcal{E}_p \dot{\alpha} \cos(\alpha) \left(\beta_1 |\dot{x}| \left(-\beta_2 \text{sign}(\mathcal{E}_p \dot{\alpha} \cos(\alpha)) + \text{sg}(X) e^{\eta|x|} \right) - 7.614 \dot{x} \right) \\ & - \beta_3 |\dot{\alpha} \cos(\alpha)| |\sin(2\alpha)| + 12.28 k \dot{\alpha} \cos(\alpha) \sin(2\alpha) \\ & - 0.0197 \sin^2(\alpha) |\mathcal{E}_p| \dot{\alpha}^2 \\ & \leq 0. \end{aligned} \tag{4.43}$$

As before, the inequality in (4.43) is satisfied when both (4.32) and (4.33) hold for the constants. Furthermore, to make sure that the sign of (4.42) is given by sg, we must have

$$\begin{aligned} & \text{sign} \left(\beta_1 |\dot{x}| \left(-\beta_2 \text{sign}(\mathcal{E}_p \dot{\alpha} \cos(\alpha)) + \text{sg}(X) e^{\eta|x|} \right) - \frac{\beta_3 \text{sign}(\dot{\alpha} \cos(\alpha)) |\sin(2\alpha)|}{\mathcal{E}_p} \right. \\ & \left. + 0.0197 \text{sign}(\mathcal{E}_p) \dot{\alpha} \cos \alpha \right) = \text{sg}(X). \end{aligned} \tag{4.44}$$

Now, consider the possible sign combinations for $\mathcal{E}_p \dot{\alpha} \cos(\alpha)$ and sg:

- Case 1: $\mathcal{E}_p \dot{\alpha} \cos(\alpha) > 0$ and $\text{sg}(X) = 1$ (i.e. want $V_m > 0$, $\dot{x} > 0$)

$$\begin{aligned} & \beta_1 |\dot{x}| \left(-\beta_2 + e^{\eta|x|} \right) - \frac{\beta_3 |\sin(2\alpha)|}{|\mathcal{E}_p|} + 0.0197 |\dot{\alpha} \cos \alpha| > 0 \\ \Rightarrow & \beta_1 > \frac{\beta_3 |\sin(2\alpha)|}{|\dot{x}| |\mathcal{E}_p| (e^{\eta|x|} - \beta_2)} - \frac{0.0197 |\dot{\alpha} \cos(\alpha)|}{|\dot{x}| (e^{\eta|x|} - \beta_2)} \end{aligned}$$

- Case 2: $\mathcal{E}_p \dot{\alpha} \cos(\alpha) > 0$ and $\text{sg}(X) = -1$ (i.e. want $V_m < 0$, $\dot{x} < 0$)

$$\begin{aligned} & \beta_1 |\dot{x}| \left(-\beta_2 - e^{\eta|x|} \right) - \frac{\beta_3 |\sin(2\alpha)|}{|\mathcal{E}_p|} + 0.0197 |\dot{\alpha} \cos \alpha| < 0 \\ \Rightarrow & \beta_1 > -\frac{\beta_3 |\sin(2\alpha)|}{|\dot{x}| |\mathcal{E}_p| (e^{\eta|x|} + \beta_2)} + \frac{0.0197 |\dot{\alpha} \cos(\alpha)|}{|\dot{x}| (e^{\eta|x|} + \beta_2)}. \end{aligned}$$

- Case 3: $\mathcal{E}_p \dot{\alpha} \cos(\alpha) < 0$ and $\text{sg}(X) = 1$ (i.e. want $V_m > 0$, $\dot{x} > 0$)

$$\begin{aligned} & \beta_1 |\dot{x}| \left(\beta_2 + e^{\eta|x|} \right) + \frac{\beta_3 |\sin(2\alpha)|}{|\mathcal{E}_p|} - 0.0197 \text{sign}(\mathcal{E}_p) \dot{\alpha} \cos \alpha > 0 \\ \Rightarrow & \beta_1 > \frac{0.0197 |\dot{\alpha} \cos(\alpha)|}{|\dot{x}| (\beta_2 + e^{\eta|x|})} - \frac{\beta_3 |\sin(2\alpha)|}{|\dot{x}| |\mathcal{E}_p| (\beta_2 + e^{\eta|x|})}. \end{aligned}$$

- Case 4: $\mathcal{E}_p \dot{\alpha} \cos(\alpha) < 0$ and $\text{sg}(X) = -1$ (i.e. want $V_m < 0$, $\dot{x} < 0$)

$$\beta_1 |\dot{x}| \left(\beta_2 - e^{\eta|x|} \right) + \frac{\beta_3 |\sin(2\alpha)|}{|\mathcal{E}_p|} - 0.0197 \text{sign}(\mathcal{E}_p) \dot{\alpha} \cos \alpha < 0$$

$$\Rightarrow \beta_1 > \frac{\beta_3 |\sin(2\alpha)|}{|\dot{x}| |\mathcal{E}_p| (e^{\eta|x|} - \beta_2)} - \frac{0.0197 |\dot{\alpha} \cos(\alpha)|}{|\dot{x}| (e^{\eta|x|} - \beta_2)}.$$

The above cases all hold when the constants $\beta_1, \beta_2, \beta_3$, and η satisfy

$$\beta_1 > \frac{\beta_3 |\sin(2\alpha)|}{|\dot{x}| |\mathcal{E}_p| (e^{\eta|x|} - \beta_2)} - \frac{0.0197 |\dot{\alpha} \cos(\alpha)|}{|\dot{x}| (e^{\eta|x|} - \beta_2)} \quad \text{and} \quad \beta_1 > \frac{0.0197 |\dot{\alpha} \cos(\alpha)|}{|\dot{x}| (\beta_2 + e^{\eta|x|})} - \frac{\beta_3 |\sin(2\alpha)|}{|\dot{x}| |\mathcal{E}_p| (\beta_2 + e^{\eta|x|})}. \quad (4.45)$$

Just as before, we must again choose $\beta_1, \beta_2, \beta_3$, and η in a way to ensure that the amplifier doesn't go into saturation (i.e. $|V_m| \leq 10$). A particular choice of constants that will satisfy all conditions for the new controller in (4.42) is $\beta_1 = 4.8$, $\beta_2 = 0.6$, $\beta_3 = 0.0115$, and $\eta = 0.6$.

4.4 Simulation Results

The controller given by (4.42) was tested in simulation with $\beta_1 = 4.8$, $\beta_2 = 0.6$, $\beta_3 = 0.0115$, and $\eta = 0.6$, using the Simulink diagrams provided in Appendix B.5 with the IP02 + SESIP Actual Plant subsystem block replaced by the SIP EOM with Friction subsystem block from the diagram in Figure B.6. Since the starting downward position of the pendulum is a stable equilibrium we must input some initial voltage to get the experiment started. The starting voltage for our simulation was 8 Volts that was applied for 0.1 second. The state responses and the corresponding control effort are graphed in Figure 4.5. The dashed blue lines in 4.5b indicate the region where the stabilization control can take over (i.e. where $|\alpha| < 15^\circ$). The simulation indicates that the controller swings the pendulum up into the upright position in approximately 30 seconds. Furthermore, all the values of the states and the required control effort stayed within the possible ranges deliverable by the apparatus we use for real time experiments. Figure 4.5a also indicates that the cart did not go past the end of the track.

4.5 Experimental Results

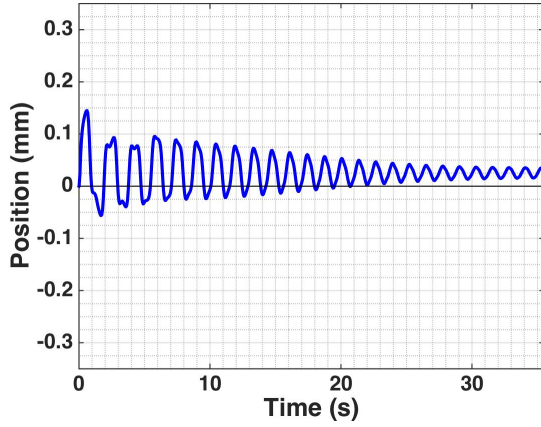
The swing-up controller given by (4.42) was successfully implemented in real-time with $\beta_1 = 4.8$, $\beta_2 = 0.6$, $\beta_3 = 0.0115$, and $\eta = 0.6$ using the MATLAB Simulink model provided in Appendix B.5. The state responses and the corresponding control effort are graphed in Figure 4.6. Figure 4.6b indicates that the controller swung up the pendulum in approximately 15 seconds. On one

occasion the required control effort reached the upper limit of 10 Volts and had to be saturated. The average amount of voltage used during the experiment was about 2.89 Volts, which is more than with the previous methods. Once the pendulum reached within 15° of the upright position, the power series based stabilization controller successfully took over. The switching was achieved by the Mode Switching Simulink block provided by Quanser.

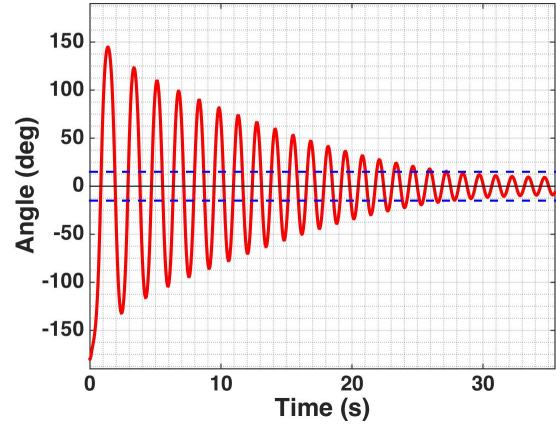
The experiment was repeated several times with swing-up times ranging between 15 and 40 seconds. During the swing-up procedure the cart makes very fast big moves because of how the function sg is defined. When the cart moves close to the end of the track, the controller successfully makes the cart move away from the edge, but this action results in a jerk of the cart. Unfortunately, sometimes when the pendulum is near the upright position, this fast jerk of the cart overpowers the movement of the pendulum and makes the pendulum loose momentum. When this happens, making up the loss of momentum increases the swing-up time.

4.6 Summary of Swing-up Controllers

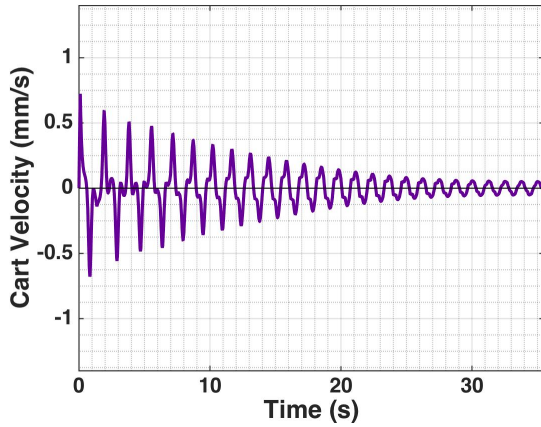
We have presented and successfully implemented a new energy-based swing-up controller that was derived using Lyapunov functions based on the method originally proposed by Astrom and Furuta [8, 9]. We've also provided two modifications to make the swing-up method more appropriate for real-time implementation. Our controller is based on a more complex dynamical model for the SIP system than the models that are most commonly used in the literature. In addition to considering the electrodynamics of the DC motor that drives the cart, we've also considered viscous damping friction as seen at the motor pinion, and our last modification also considered the viscous damping as seen at the pendulum axis. Furthermore, we have accounted for the limitation of having a cart-pendulum system with a finite track length. This was accomplished using a method that is different from other previously published methods. Our final swing-up controller, given in equation (4.42), was able to swing the pendulum up in approximately 15 seconds, which is comparable to the swing-up time of the proportional-velocity controller provided by Quanser with our apparatus [62]. However, the swing-up time of our controller is not consistent.



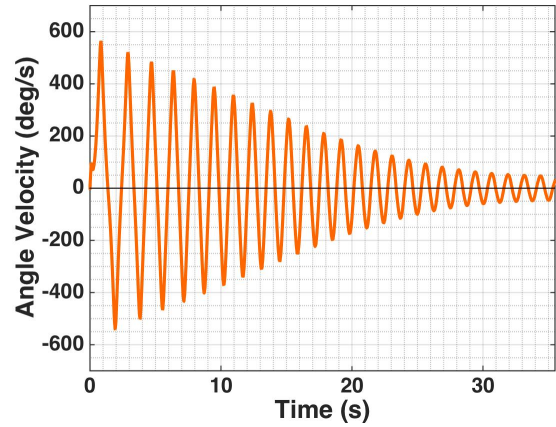
(a) Cart Position, $|x| < 0.146$ m



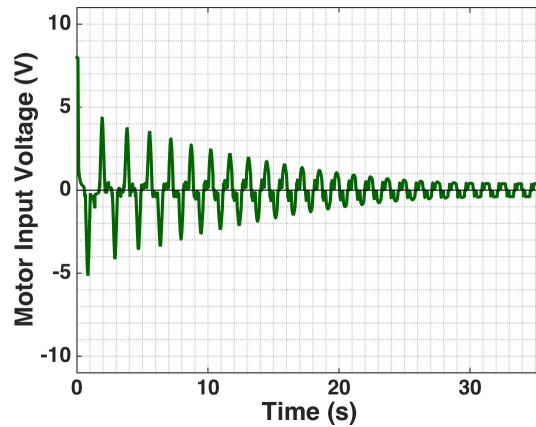
(b) Pendulum Angle



(c) Cart Velocity, $|\dot{x}| < 0.724$ m/s

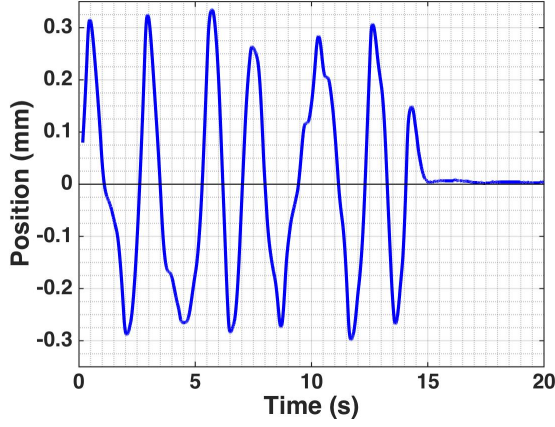


(d) Pendulum's Angular Velocity, $|\dot{\alpha}| < 564$ deg/s

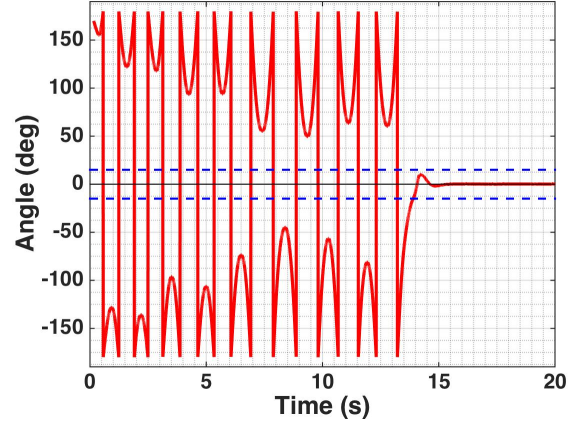


(e) Control Effort, $|V_m| \leq 8$ Volts, $|V_m|_{\text{avg}} = 0.68$ Volt

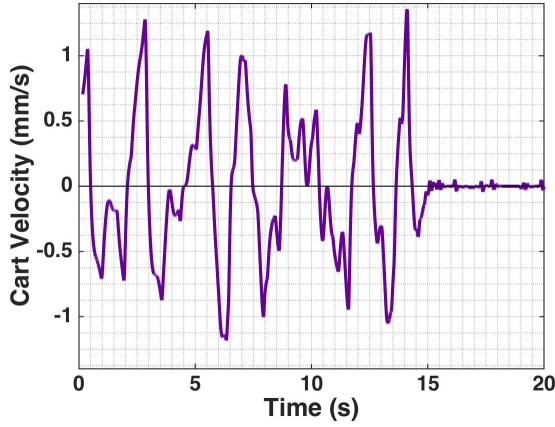
Figure 4.5: Simulated state response and control effort for the more robust swing up controller including viscous damping at the pendulum axis.



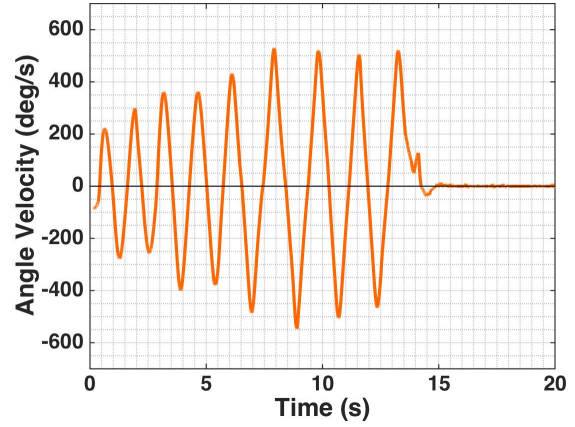
(a) Cart Position, $|x| < 0.335$ m



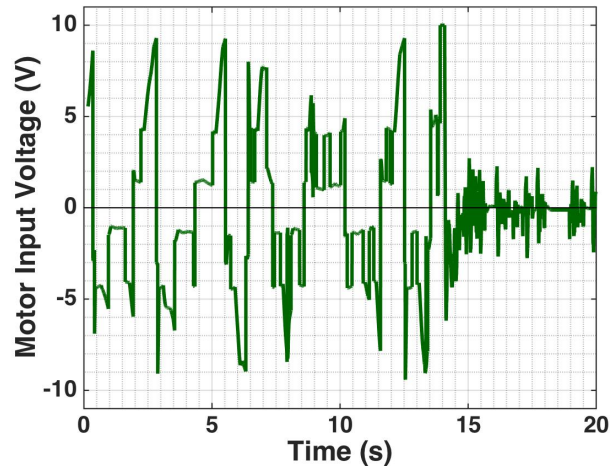
(b) Pendulum Angle



(c) Cart Velocity, $|\dot{x}| < 1.36$ m/s



(d) Pendulum's Angular Velocity, $|\dot{\alpha}| < 547$ deg/s



(e) Control Effort, $|V_m| \leq 10$ Volts, $|V_m|_{\text{avg}} = 2.89$ Volts

Figure 4.6: Experimental state response and control effort for the energy based swing up controller given in equation (4.42) with $\beta_1 = 4.8$, $\beta_2 = 0.6$, $\beta_3 = 0.0115$, and $\eta = 0.6$.

Chapter 5

Closing Remarks

5.1 General Conclusion

In the first part of this dissertation, we presented the successful real-time implementation of a power series based nonlinear control method for the stabilization of an inverted pendulum. This method has not been implemented for a SIP system before. Experimental results indicated that the controller performs slightly better than the traditional linear quadratic regulator that is commonly used for stabilization. Furthermore, the presented method has a larger stability region, and it can be used with state-dependent weighting matrices.

In the second part of this work, we modified the swing-up method of Astrom and Furuta [8, 9] to create a new energy-based swing-up controller that was derived using a more complex dynamical model for the SIP system than the simplified models that are commonly used. It is often the case, that a controller based on a simplified model works well in simulation, but not in real-time. For the purposes of real-time implementation and many applications, it is desirable to consider the effects of friction, and incorporate physical restrictions of the SIP system like the maximum deliverable voltage by the amplifier, the capacity of the DC motor that drives the cart, and the finite track length. The control method presented accounts for viscous damping friction, and it also takes many of the physical restrictions of the actual SIP system into account. Even though the controller can successfully swing-up the pendulum, the amount of time it takes for the pendulum to reach the upright position is inconsistent.

5.2 Future Work

Future work involves investigating ways to make the swing-up time of our swing-up controller more consistent. We would also like to complete further real-time testing and tuning of both the stabilizing and the swing-up controllers presented. Furthermore, we would like to consider

further modifications like incorporating the effects of both static friction and stick slip friction. Some work has been done in this direction already by Campbell et al. for the stabilization problem using a linear quadratic regulator [18, 17]. Our plan is to extend their work for both the power series based nonlinear stabilizing controller, and for the energy based swing-up controller that we presented. We would also like to implement our controls for a double inverted pendulum in real-time.

REFERENCES

- [1] ALVAREZ-ICAZA, L. Passivity-based swinging up of a pendulum. In *Preprints of the 18th IFAC World Congress* (2011), International Federation of Automatic Control, pp. 10667–10672.
- [2] ANDERSON, C. W. Learning to control an inverted pendulum using neural networks. *IEEE Control Systems Magazine* 9, 3 (1989), 31–37.
- [3] ANGELI, D. Almost global stabilization of the inverted pendulum via continuous state feedback. *Automatica* 37 (2001), 1103–1108.
- [4] ARACIL, J., AND GORDILLO, F. The inverted pendulum: A benchmark in nonlinear control theory. In *Proceedings of the Sixth Biannual World Automation Congress - Intelligent Automation and Control Trends, Principles, and Applications* (Seville, 2004), pp. 468–482.
- [5] ARACIL, J., GORDILLO, F., AND ASTROM, K. J. A family of pumping-damping smooth strategies for swinging up a pendulum. In *Lagrangian and Hamiltonian Methods for Nonlinear Control 2006*, F. Allgower, P. Fleming, P. Kokotovic, A. Kurzhanski, H. Kwakernaak, A. Rantzer, J. Tsitsiklis, F. Bullo, and K. Fujimoto, Eds., vol. 366 of *Lecture Notes in Control and Information Sciences*. Springer Berlin Heidelberg, 2007, pp. 341–352.
- [6] ASTROM, K. J. Hybrid control of inverted pendulums. In *Learning, control and hybrid systems*, Y. Yamamoto and S. Hara, Eds., vol. 241 of *Lecture Notes in Control and Information Sciences*. Springer, London, 1999, ch. Hybrid Control of Inverted Pendulums, pp. 150–163.
- [7] ASTROM, K. J., ARACIL, J., AND GORDILLO, F. A family of smooth controllers for swinging up a pendulum. *Automatica* 44, 7 (July 2008), 1841–1848.
- [8] ASTROM, K. J., AND FURUTA, K. Swinging up a pendulum by energy control. In *Preprints of the 13th IFAC World Congress* (San Francisco, CA, 1996), vol. E, pp. 37–42.
- [9] ASTROM, K. J., AND FURUTA, K. Swinging up a pendulum by energy control. *Automatica* 36 (2000), 287–295.
- [10] ASTROM, K. J., HAGGLUND, T., HANG, C. C., AND HO, W. K. Automatic tuning and adaptation for pid controllers - a survey. *Control Engineering Practice* 1, 4 (1993), 699–714.
- [11] BALAN, R., MATIES, V., AND STAN, S. A solution of the inverse pendulum on a cart problem using predictive control. In *Proceedings of the IEEE International Symposium on Industrial Electronic* (Dubrovnik, June 2005), pp. 63–68.
- [12] BANKS, H. T., LEWIS, B. M., AND TRAN, H. T. Nonlinear feedback controllers and compensators: a state-dependent riccati equation approach. *Computational Optimization and Applications* 37, 2 (June 2007), 177–218.

- [13] BANKS, H. T., SMITH, R. C., AND WANG, Y. *Smart Material Structures: Modeling, Estimation, and Control*. Wiley, Chichester, England, 1996.
- [14] BEELER, S. C., TRAN, H. T., AND BANKS, H. T. Feedback control methodologies for nonlinear systems nonlinear feedback. *Journal of Optimization Theory and Applications* 107, 1 (October 2000), 1–33.
- [15] BOUBAKER, O. The inverted pendulum benchmark in nonlinear control theory: A survey. *International Journal of Advanced Robotic Systems* 10 (2013), 1–9.
- [16] BUGEJA, M. Non-linear swing-up and stabilizing control of an inverted pendulum system. In *EUROCON 2003. Computer as a Tool. The IEEE Region 8* (September 2003), B. Zajc and M. Tkalcic, Eds., vol. 2, pp. 437–441.
- [17] CAMPBELL, S. A., CRAWFORD, S., AND MORRIS, K. Time delay and feedback control of an inverted pendulum with stick slip friction. In *Proceedings of ASME 2007 International Design Engineering Technical Conferences & Computers and Information in Engineering Conference* (Las Vegas, September 2007).
- [18] CAMPBELL, S. A., CRAWFORD, S., AND MORRIS, K. Friction and the inverted pendulum stabilization problem. *Journal of Dynamic Systems, Measurement and Control* 130, 5 (September 2008).
- [19] CHANG, W.-D., HWANG, R.-C., AND HSIEH, J.-G. A self-tuning pid control for a class of nonlinear systems based on the lyapunov approach. *Journal of Process Control* 12 (2002), 233–242.
- [20] CHATTERJEE, D., PATRA, A., AND JOGLEKAR, H. K. Swing-up and stabilization of a cart-pendulum system under restricted cart track length. *Systems & Control Letters* 47 (2002), 355–364.
- [21] CHUNG, C. C., AND HAUSER, J. Nonlinear control of a swinging pendulum. *Automatica* 31, 6 (1995), 851–862.
- [22] DANG, P., AND LEWIS, F. L. Controller for swing-up and balance of single inverted pendulum using sdre-based solution. In *Industrial Electronics Society, 2005. IECON 2005. 31st Annual Conference of IEEE* (November 2005), IEEE, pp. 304–309.
- [23] DAVISON, E. J. Benchmark problems for control system design. Tech. rep., International Federation of Automatic Control, May 1990.
- [24] DEWEY, J., AND BYERLY, P. The early history of seismometry (to 1900). *Bulletin of the Seismological Society of America* 59, 1 (February 1969), 183–227.
- [25] EIDE, R., EGELID, P. M., STAMSO, A., AND R., K. H. Lqg control design for balancing an inverted pendulum mobile robot. *Intelligent Control and Automation* 2 (2011), 160–166.
- [26] GARRARD, W. L. Suboptimal feedback control for nonlinear systems. *Automatica* 8 (1972), 219–221.

- [27] GARRARD, W. L., ENNS, D. F., AND SNELLS, S. A. Nonlinear feedback control of highly maneuverable aircraft. *International Journal of Control* 56 (1992), 799–812.
- [28] GARRARD, W. L., AND JORDAN, J. M. Design of nonlinear automatic flight control systems. *Automatica* 13 (1977), 497–505.
- [29] GAWTHROP, P. J., AND WANG, L. Intermittent predictive control of an inverted pendulum. *Control Engineering Practice* 14 (2006), 1347–1356.
- [30] GORDILLO, F., AND ARACIL, J. A new controller for the inverted pendulum on a cart. *International Journal of Robust and Nonlinear Control* 18 (January 2008), 1607–1621.
- [31] GUZELLA, L., AND ISIDORI, A. On approximate linearization of nonlinear control systems. *International Journal of Robust and Nonlinear Control* 3, 3 (1993), 261–276.
- [32] HAESSIG, JR., D. A., AND FRIEDLAND, B. Modeling and simulation of friction. In *Proceedings of SPIE, Acquisition, Tracking, and Pointing V* (August 1991), vol. 1482, pp. 383–396.
- [33] HAMZA, M., UR REHMAN, Z., ZAHID, Q., TAHIR, F., AND KHALID, Z. Real-time control of an inverted pendulum: A comparative study. In *Frontiers of Information Technology (FIT), 2011* (December 2011), pp. 183–188.
- [34] HASSANI, K., AND LEE, W.-S. Optimal tuning of linear quadratic regulators using quantum particle swarm optimization. In *Proceedings of the International Conference of Control, Dynamic Systems, and Robotics* (Ottawa, Ontario, Canada, May 2014).
- [35] HESPANHA, J. P. Lqg/lqr controller design. Undergraduate Lecture Notes, Department of Electrical and Computer Engineering, University of California, Santa Barbara, April 2007.
- [36] HOLZHUTER, T. Optimal regulator for the inverted pendulum via euler-lagrange backward integration. *Automatica* 40 (2004), 1613–1620.
- [37] HUIFENG, C., HONGXING, L., AND PEIPEI, Y. Swing-up and stabilization of the inverted pendulum by energy well and sdre. In *Control and Decision Conference, 2009. CCDC '09. Chinese* (June 2009), IEEE, pp. 2222–2226.
- [38] HUNT, L. R., AND TURI, J. A new algorithm for constructing approximate transformations for nonlinear systems. *IEEE Transactions on Automatic Control* 38, 10 (October 1993), 1553–1556.
- [39] INGRAM, D., WILLSON, S. S., MULLHAUPT, P., AND BONVIN, D. Stabilization of an experimental cart-pendulum system through approximate manifold decomposition. In *Preprints of the 18th IFAC World Congress* (Milano, Italy, 2011), International Federation of Automatic Control, pp. 10659–10666.
- [40] ISIDORI, A. *Nonlinear Control Systems*. Springer Verlag, New York, 1989.

- [41] KRENER, A. J. Approximate linearization by state feedback and coordinate change. *Systems & Control Letters* 5, 3 (December 1984), 181–185.
- [42] KRENER, A. J., AND ISIDORI, A. Linearization by output injection and nonlinear observers. *Systems & Control Letters* 3, 1 (June 1983), 47–52.
- [43] KRENER, A. J., KARAHAN, S., HUBBARD, M., AND FREZZA, R. Higher order linear approximations to nonlinear control systems. In *Proceedings of the 26th IEEE Conference on Decision and Control* (Los Angeles, CA, December 1987), vol. 26, IEEE, pp. 519–523.
- [44] KRISHNAN, T. R. On stabilization of cart-inverted pendulum system: An experimental study. Master’s thesis, National Institute of Technology, Rourkela-769008, India, July 2012.
- [45] KUMAR, R., SINGH, R. B., AND DAS, J. Modeling and simulation of inverted pendulum system using matlab: Overview. *International Journal of Mechanical and Production Engineering* 1, 4 (October 2013), 52–55.
- [46] KUMAR, V., AND JEROME, J. Stabilizing controller design for self erecting single inverted pendulum using robust lqr. *Australian Journal of Basic and Applied Sciences* 7, 7 (2013), 494–504.
- [47] LANDRY, M., CAMPBELL, S. A., MORRIS, K., AND AGUILAR, C. O. Dynamics of an inverted pendulum with delayed feedback control. *SIAM Journal on Applied Dynamical Systems* 4, 2 (2005), 333–351.
- [48] LASIECKA, I., AND TRIGGIANI, R. *Differential and Algebraic Riccati Equations with Application to Boundary/Point Control Problems*, vol. 164 of *Lecture Notes in Control and Information Sciences*. Springer, New York, 1991.
- [49] LOZANO, R., FANTONI, I., AND BLOCK, D. J. Stabilization of the inverted pendulum around its homoclinic orbit. *Systems & Control Letters* 40 (2000), 197–204.
- [50] MAEBA, T., DENG, M., YANOU, A., AND HENMI, T. Swing-up controller design for inverted pendulum using energy method based on lyapunov functions. In *Proceedings of the 2010 International Conference on Modelling, Identification and Control* (Okayama, Japan, July 2010), pp. 768–773.
- [51] MAGNI, L., SCATTOLINI, R., AND ASTROM, K. J. Global stabilization of the inverted pendulum using model predictive control. In *Proceedings of the 15th IFAC World Congress* (Barcelona, 2002).
- [52] MASON, P., BROUCKE, M., AND PICCOLI, B. Time optimal swing-up of the planar pendulum. *IEEE Transactions on Automatic Control* 53, 8 (2008), 1876–1886.
- [53] MAZENC, F., AND BOWONG, S. Tracking trajectories of the cart-pendulum system. *Automatica* 39 (2003), 677–684.
- [54] MAZENC, F., AND PRALY, L. Asymptotic tracking of a reference state for systems with feedforward structure. *Automatica* 36 (2000), 179–187.

- [55] MILLS, A., WILLS, A., AND NINNESS, B. Nonlinear model predictive control for an inverted pendulum. In *Proceedings of the American Control Conference* (St. Louis, June 2009), pp. 2335–2340.
- [56] MIRANDA, J. L. C. Applications of kalman filtering and pid control for direct inverted pendulum control. Master’s thesis, California State University, Chico, 2009.
- [57] OHSUMI, A., AND IZUMIKAWA, T. Nonlinear control of swing-up and stabilization of an inverted pendulum. In *Proceedings of the 34th IEEE Conference on Decision & Control* (New Orleans, LA, December 1995), IEEE, pp. 3873–3880.
- [58] OLSSON, H., AND ASTROM, K. J. Friction generated limit cycles. *IEEE Transactions on Control Systems Technology* 9, 4 (July 2001), 629–636.
- [59] ORTEGA, R., SCHAFT, A. V. D., MASCHKE, B., AND ESCOBAR, G. Interconnection and damping assignment passivity-based control of port-controlled hamiltonian systems. *Automatica* 38 (2002), 585–596.
- [60] PARK, M.-S., AND CHWA, D. Swing-up and stabilization control of inverted pendulum systems via coupled sliding-mode control method. *IEEE Transactions on Industrial Electronics* 56, 9 (2009), 3541–3555.
- [61] PAVLIC, T. P. Rotary electrodynamics of a dc motor: Motor as mechanical capacitor. ECE 758: Control System Implementation Laboratory Notes, Department of Electrical and Computer Engineering, The Ohio State University, 2007-2009.
- [62] QUANSER CONSULTING, INC. *Linear Motion Servo Plant: IP02 - Linear Experiment #6: PV and LQR Control - Student Handout*, 4.1 ed.
- [63] QUANSER CONSULTING, INC. *Linear Motion Servo Plants: IP01 or IP02 - IP01 and IP02 User Manual*, 5.0 ed.
- [64] QUANSER CONSULTING, INC. *Linear Motion Servo Plants: IP01 or IP02 - Linear Experiment #1: PV Position Control - Instructor Manual*, 4 ed.
- [65] QUANSER CONSULTING, INC. *Linear Motion Servo Plants: IP01 or IP02 - Linear Experiment #1: PV Position Control - Student Handout*, 4 ed.
- [66] QUANSER CONSULTING, INC. *Linear Motion Servo Plants: IP01 or IP02 - Linear Experiment #5: LQR Control - Instructor Manual*, 4.1 ed.
- [67] QUANSER CONSULTING, INC. *Linear Motion Servo Plants: IP01 or IP02 - Linear Experiment #5: LQR Control - Student Handout*, 4.1 ed.
- [68] QUANSER CONSULTING, INC. *Linear Motion Servo Plants: IP01 or IP02 - Single Inverted Pendulum (SIP) User Manual*, 3 ed.
- [69] RENOU, S., AND SAYDY, L. Real time control of an inverted pendulum based on approximate linearization. In *Canadian Conference on Electrical and Computer Engineering* (Calgary, Alta, May 1996), vol. 2, IEEE, pp. 502–504.

- [70] SAIFIZUL, A. A., ZAINON, Z., ABU OSMAN, N. A., AZLAN, C. A., AND UNGKU IBRAHIM, U. F. S. Intelligent control for self-erecting inverted pendulum via adaptive neuro-fuzzy inference system. *American Journal of Applied Sciences* 3, 4 (2006), 1795–1802.
- [71] SANTISTEBAN, R., FLOQUET, T., ORLOV, Y., RIACHY, S., AND RICHARD, J.-P. Second order sliding mode control of underactuated mechanical systems ii: Orbital stabilization of an inverted pendulum with applications to swing up / balancing control. *International Journal of Robust and Nonlinear Control* 18, 4-5 (2008), 544–556.
- [72] SINGH, N. M., DUBEY, J., AND LADDHA, G. Control of pendulum on a cart with state dependent riccati equations. *World Academy of Science, Engineering and Technology* 2, 5 (May 2008), 1283–1287.
- [73] SIUKA, A., AND SCHOBERL, M. Applications of energy based control methods for the inverted pendulum on a cart. *Robotics and Autonomous Systems* 57 (2009), 1012–1017.
- [74] SRINIVASAN, B., HUGUENIN, P., AND BONVIN, D. Global stabilization of an inverted pendulum - control strategy and experimental verification. *Automatica* 45 (2009), 265–269.
- [75] SUGIE, T., AND FUJIMOTO, K. Control of inverted pendulum system based on approximate linearization: design and experiment. In *Proceedings of the 33rd IEEE Conference on Decision & Control* (Lake Buena Vista, FL, December 1994), vol. 2, IEEE, pp. 1647–1648.
- [76] SULTAN, K. Inverted pendulum: Analysis, design and implementation. Tech. rep., Institute of Industrial Electronics Engineering, Karachi, Pakistan, 2003.
- [77] TRIMPE, S., MILLANE, A., DOESSEGGER, S., AND D’ANDREA, R. A self-tuning lqr approach demonstrated on an inverted pendulum. In *Preprints of the 19th World Congress* (Cape Town, South Africa, August 2014), The International Federation of Automatic Control.
- [78] WANG, H. O., TANAKA, K., AND GRIFFIN, M. F. An approach to fuzzy control of nonlinear systems: Stability and design issues. *IEEE Transactions on Fuzzy Systems* 4, 1 (February 1996).
- [79] XU, Y., IWASE, M., AND FURUTA, K. Time optimal swing-up control of single pendulum. *Journal of Dynamic Systems, Measurement and Control* 123, 3 (2001), 518–527.
- [80] YI, J., YUBAZAKI, N., AND HIROTA, K. Upswing and stabilization control of inverted pendulum system based on the sirms dynamically connected fuzzy inference model. *Fuzzy Sets and Systems* 122 (2001), 139–152.
- [81] YUCELEN, T., SADAHALLI, A. S., AND POURBOGHRAT, F. Online solution of state dependent riccati equation for nonlinear system stabilization. In *American Control Conference (ACC), 2010* (June 2010), IEEE, pp. 6336–6341.
- [82] ZAISER, M. Dynamics 4 lecture notes. Lecture Notes, School of Engineering, University of Edinburgh.

- [83] ZHAO, J., AND SPONG, M. W. Hybrid control for global stabilization of the cart-pendulum system. *Automatica* *37* (2001), 1941–1951.

APPENDICES

Appendix A

Model Parameters

A.1 Nomenclature

Symbol	Description	Matlab/Simulink Notation
α	Pendulum Angle From the Upright Position	alpha
$\dot{\alpha}$	Pendulum Angular Velocity	alpha_dot
$\ddot{\alpha}$	Pendulum Angular Acceleration	alpha_ddot
$A0, B0$	Linearized State-Space Matrices of the SIP-plus-IP02 System	A0, B
B_p	Viscous Damping Coefficient as Seen at the Pendulum Axis	Bp
B_{eq}	Equivalent Viscous Damping Coefficient as seen at the Motor Pinion	Beq
E_{emf}	Back-EMF Voltage	Eemf
\mathcal{E}_p	Total Energy of the Pendulum	Ep
F_{ai}	Armature Rotational Inertial Force acting on the Cart	
F_c	Cart Driving Force generated by the DC Motor	
g	Gravitational Constant	

Symbol	Description	Matlab/Simulink Notation
I_m	Motor Armature Current	Im
I_p	Pendulum's Moment of Inertia at its Center of Gravity	Ip
J_p	Pendulum's Moment of Inertia at its Hinge	Jp
J_m	Rotational Moment of Inertia of the DC Motor's Output Shaft	Jm
\mathcal{K}_T	System's Total Kinetic Energy	
K_g	Planetary Gearbox Gear Ratio	Kg
\mathcal{K}_{ct}	Translational Kinetic Energy of the Motorized Cart	
\mathcal{K}_{cr}	Rotational Kinetic Energy Due to the Cart's DC Motor	
\mathcal{K}_{pt}	The Pendulum's Translational Kinetic Energy	
\mathcal{K}_{pr}	The Pendulum's Rotational Kinetic Energy	
K_m	Back-ElectroMotive-Force (EMF) Constant	Km
K_t	Motor Torque Constant	Kt
K	Optimal LQR Feedback Gain Vector	K
\mathcal{L}	Lagrangian	
L, L_2	Lyapunov Functions	
L_m	Motor Armature Inductance	
ℓ_p	Pendulum Length from Pivot to Center Of Gravity	lp
M_p	Pendulum Mass (with T-fitting)	Mp
M_w	Cart Weight Mass	Mw
M	Cart Mass with Extra Weight	
P	Positive-Definite Matrix Solution to the ARE	P

Symbol	Description	Matlab/Simulink Notation
Q	Symmetric Positive-Semidefinite Weighting Matrix	Q
R	Positive Weighting Scalar	R
R_m	Motor Armature Resistance	Rm
r_{mp}	Motor Pinion Radius	r_mp
S	Solution to the HJB equation	
T_{ai}	Armature Inertial Torque	
T_m	Torque Generated by the Motor	
t	Continuous Time	
\mathcal{V}_T	System's Total Potential Energy	
V_m	Motor Armature Voltage	Vm
v_{COG}	Velocity of the Pendulum's Center of Gravity	
X	State Vector	X
x	Cart Linear Position	x
\dot{x}	Cart Velocity	x.dot
\ddot{x}	Cart Acceleration	x.ddot
x_p	Absolute x-coordinate of the Pendulum Center Of Gravity	
y_p	Absolute y-coordinate of the Pendulum Center Of Gravity	
θ_m	Motor Shaft Rotational Angle	
ω	Motor Pinion Angular Velocity	
ω_m	Motor Shaft Angular Velocity	

A.2 Model Parameter Values

Parameter	Description	Value
B_p	Viscous Damping Coefficient, as seen at the Pendulum Axis	0.0024 N.m.s/rad
B_{eq}	Equivalent Viscous Damping Coefficient as seen at the Motor Pinion	5.4 N.m.s/rad
g	Gravitational Constant	9.81 m/s ²
I_p	Pendulum Moment of Inertia, about its Center of Gravity	8.359E-003 kg.m ²
J_p	Pendulum's Moment of Inertia at its Hinge	3.344E-002kg.m ²
J_m	Rotor Moment of Inertia	3.90E-007 kg.m ²
K_g	Planetary Gearbox Gear Ratio	3.71
K_t	Motor Torque Constant	0.00767 N.m/A
K_m	Back-ElectroMotive-Force (EMF) Constant	0.00767 V.s/rad
ℓ_p	Pendulum Length from Pivot to Center Of Gravity	0.3302 m
M_w	Cart Weight Mass	0.37 kg
M	Cart Mass with Extra Weight	$0.57 + M_w$ kg
M_p	Pendulum Mass	0.230 kg
R_m	Motor Armature Resistance	2.6 Ω
r_{mp}	Motor Pinion Radius	6.35E-003 m

Appendix B

MATLAB Code

B.1 Code to Setup Parameters for the Simulink Diagrams

```
% Code to setup the SIP system's model parameters.
% The below code is a modification of the setup code provided by Quanser

clear all
global IC_ALPHA0 %initial angle (used in simulation)
IC_ALPHA0 = 0;
% conversion to radians
IC_ALPHA0 = IC_ALPHA0 / 180 * pi;

%%% Calculate useful conversion constants %%%
% from radians to degrees
K_R2D = 180 / pi;
% from degrees to radians
K_D2R = 1 / K_R2D;
% from Inch to Meter
K_IN2M = 0.0254;
% from Meter to Inch
K_M2IN = 1 / K_IN2M;
% from rad/s to RPM
K_RDPS2RPM = 60 / ( 2 * pi );
% from RPM to rad/s
```

```

K_RPM2RDPS = 1 / K_RDPS2RPM;
% from oz-force to N
K_OZ2N = 0.2780139;
% from N to oz-force
K_N2OZ = 1 / K_OZ2N;

%%%%%%%%%%%%%%%%%%%%%%%%%%%%%%%%%%%%%%%%%%%%%%%%%%%%%%%%%%%%%%%%%%%%%%%%
% Motor Armature Resistance (Ohm)
Rm = 2.6;
% Motor Armature Inductance (H)
Lm = 180e-6;
% Motor Torque Constant (N.m/A)
Kt = 1.088 * K_OZ2N * K_IN2M; % = .00767
% Motor Back-EMF Constant (V.s/rad)
Km = 0.804e-3 * K_RDPS2RPM; % = .00767
% Rotor Inertia (kg.m^2)
Jm = 5.523e-5 * K_OZ2N * K_IN2M; % = 3.9e-7
% Cart Weight Mass (kg)
Mw = 0.37;
% IP02 Cart Mass, with 3 cable connectors (kg)
M = 0.57+Mw;
% Planetary Gearbox (a.k.a. Internal) Gear Ratio
Kg = 3.71;
% Cart Motor Pinion number of teeth
N_mp = 24;
% Motor Pinion Radius (m)
r_mp = 0.5 / 2 * K_IN2M; % = 6.35e-3
% Cart Position Pinion number of teeth
N_pp = 56;
% Position Pinion Radius (m)
r_pp = 1.167 / 2 * K_IN2M; % = 14.8e-3
% Rack Pitch (m/teeth)
Pr = 1e-2 / 6.01; % = 0.0017
% Cart Travel (m)
Tc = 0.814;

```

```

% Equivalent Viscous Damping Coefficient as seen at the Motor Pinion
Beq = 5.4;
% Gravity Constant
g = 9.81;
% Pendulum Mass (with T-fitting)
Mp = 0.230;
% Distance from Pivot to Centre Of Gravity (COG)
lp = 13 * K_IN2M; % = 0.3302
% Pendulum Moment of Inertia (kg.m^2) at COG
Ip = Mp * lp^2 / 3; % = 8.359e-3
% Pendulum Moment of Inertia (kg.m^2) at Hinge
Jp = 4*Ip; % = 3.344e-2
% Equivalent Viscous Damping Coefficient at the Pendulum Axis (N.m.s/rad)
Bp = 0.0024;

%%% Initialize the State-Space Representation of SIP System %%%
x1=sym('x1'); x2=sym('x2'); x3=sym('x3'); x4=sym('x4');
x=[x1;x2;x3;x4];

d=4*M*r_mp^2+Mp*r_mp^2+4*Jm*Kg^2; %used in denominator
f31=((-4*(Rm*r_mp^2*Beq+Kg^2*Kt*Km))...
/(Rm*(d+3*r_mp^2*Mp*sin(x(2))^2))*x(3)...
+((-3*Bp*r_mp^2*cos(x(2))))...
/(lp*(d+3*r_mp^2*Mp*sin(x(2))^2))*x(4)...
+((-4*Mp*lp*r_mp^2*sin(x(2))))...
/(d+3*r_mp^2*Mp*sin(x(2))^2))*x(4)^2 ...
+((3*Mp*g*r_mp^2*cos(x(2))*sin(x(2))))...
/(d+3*r_mp^2*Mp*sin(x(2))^2));
f41=((-3*(Rm*r_mp^2*Beq+Kg^2*Kt*Km)*cos(x(2)))...
/(lp*Rm*(d+3*r_mp^2*Mp*sin(x(2))^2))*x(3)...
+((-3*(M*r_mp^2+Mp*r_mp^2+Jm*Kg^2)*Bp))...
/(Mp*lp^2*(d+3*r_mp^2*Mp*sin(x(2))^2))*x(4)...
+((-3*Mp*r_mp^2*sin(x(2))*cos(x(2))))...
/(d+3*r_mp^2*Mp*sin(x(2))^2))*x(4)^2 ...
+((3*(M*r_mp^2+Mp*r_mp^2+Jm*Kg^2)*g*sin(x(2))))...

```

```

/(lp*(d+3*r_mp^2*Mp*sin(x(2))^2));

F=[x(3);x(4);f31;f41];

A0=zeros(4);
A0(1,3)=1; A0(2,4)=1;
A0(:,2)=vpa(subs(taylor(F,x,'Order',2),x,[0;1;0;0]));
A0(:,3)=vpa(subs(taylor(F,x,'Order',2),x,[0;0;1;0]));
A0(:,4)=vpa(subs(taylor(F,x,'Order',2),x,[0;0;0;1]));

b3=(4*r_mp*Kg*Kt)/(Rm*(d+3*r_mp^2*Mp*sin(x(2))^2));
b4=(3*r_mp*Kg*Kt*cos(x(2)))/(lp*Rm*(d+3*r_mp^2*Mp*sin(x(2))^2));

B=zeros(4,1);
B(3,1)=vpa(subs(taylor(b3,x,'Order',1),x,[0;0;1;0]));
B(4,1)=vpa(subs(taylor(b4,x,'Order',1),x,[0;0;0;1]));

F3=taylor(F,x,'Order',4)-taylor(F,x,'Order',2);

f3=matlabFunction(F3,'vars',x);

%%% Setup Weighting Matrices for Stabilization
Q = diag( [ 800 150 1 1 ] );
R(1,1) = [ 0.1 ];
%Q = diag( [ 5 50 0 0 ] );
%R(1,1) = [ 0.002 ];
% Solve the Algebraic Riccati Equation
P=care(A0,B,Q,R);

%%%%% Setup Parameters for SIP Plant block provided by Quanser %%%%%%
% Turn on or off the safety watchdog on the cart position:
% set it to 1 , or 0
X_LIM_ENABLE = 1; % safety watchdog turned ON
%X_LIM_ENABLE = 0; % safety watchdog turned OFF
% Safety Limits on the cart displacement (m)

```

```

XMAX = 0.35;           % cart displacement maximum safety position (m)
XMIN = - XMAX;        % cart displacement minimum safety position (m)
% Turn on or off the safety watchdog on the pendulum angle:
% set it to 1 , or 0
ALPHA_LIM_ENABLE = 1;   % safety watchdog turned ON
%ALPHA_LIM_ENABLE = 0;   % safety watchdog turned OFF
% Safety Limits on the pendulum angle (deg)
global ALPHA_MAX ALPHA_MIN
ALPHA_MAX = 20;         % pendulum angle maximum safety position (deg)
ALPHA_MIN = - ALPHA_MAX; % pendulum angle minimum safety position (deg)
% Digital-to-Analog Maximum Voltage (V);
VMAX_DAC = 10;
% Amplifier Gain: set VoltPAQ amplifier gain to 1
K_AMP = 1;
% Set the Amplifier Maximum Output Voltage (V) and Output Current (A)
% rm: for low values of K_CABLE, VMAX_AMP is limited by VMAX_DAC
VMAX_AMP = 24;
IMAX_AMP = 4;
% Cart Encoder Resolution (m/count)
K_EC = Pr * N_pp / ( 4 * 1024 ); % = 22.7485 um/count
% Pendulum Encoder Resolution (rad/count)
% K_EP is positive , since CCW is the positive sense of rotation
K_EP = 2 * pi / ( 4 * 1024 ); % = 0.0015
% Specifications of a second-order low-pass filter
wcf = 2 * pi * 10.0; % filter cutting frequency
zeta_f = 0.9;         % filter damping ratio

```

B.2 Simulink Diagrams for Model Calibration

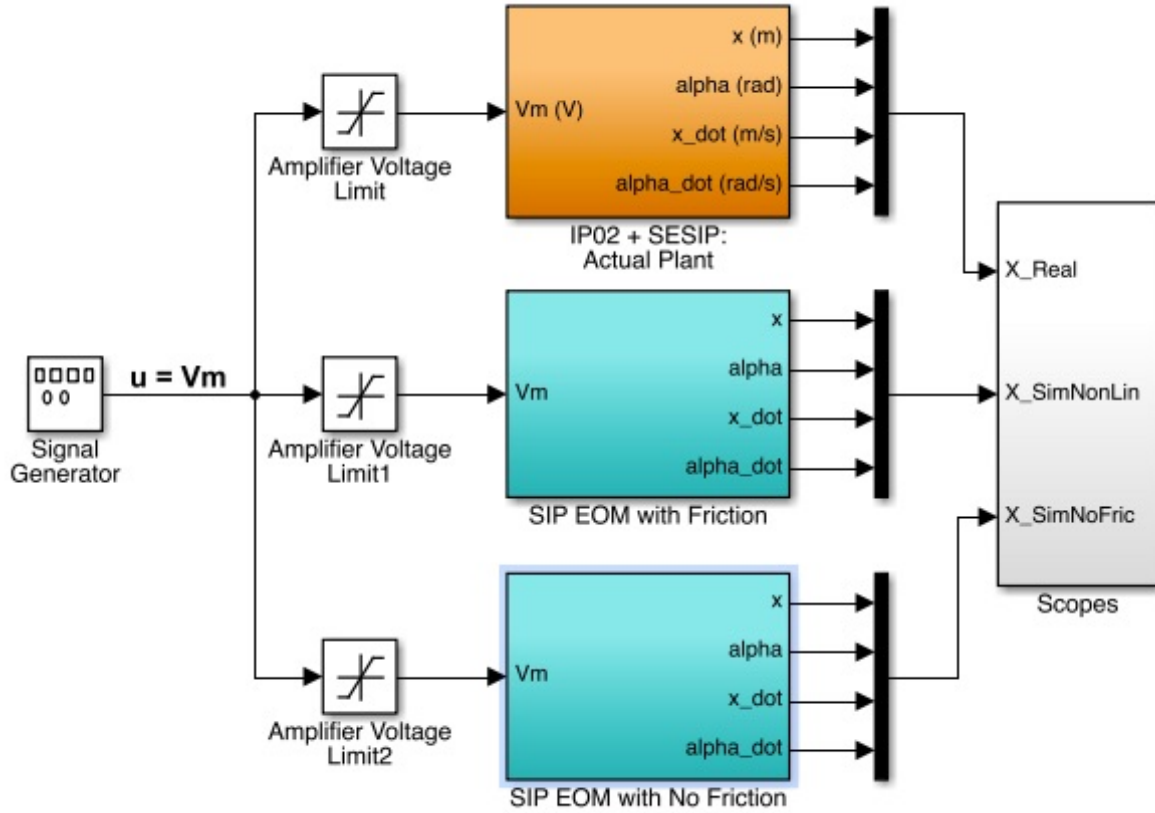


Figure B.1: Main Simulink diagram used for model calibration. The SIP + IP02: Actual Plant block that communicates with the apparatus and captures the value of the states in real-time was provided by Quanser. The SIP EOM with Friction subsystem computes the simulated state response based on the nonlinear equations of motion with friction given by equations (2.33) and (2.34). The details of the subsystem are given in Figures B.2-B.4. The SIP EOM with No Friction subsystem is the same as the subsystem with friction, but the friction coefficients are ignored (i.e. $B_{eq} = 0$ and $B_p = 0$).

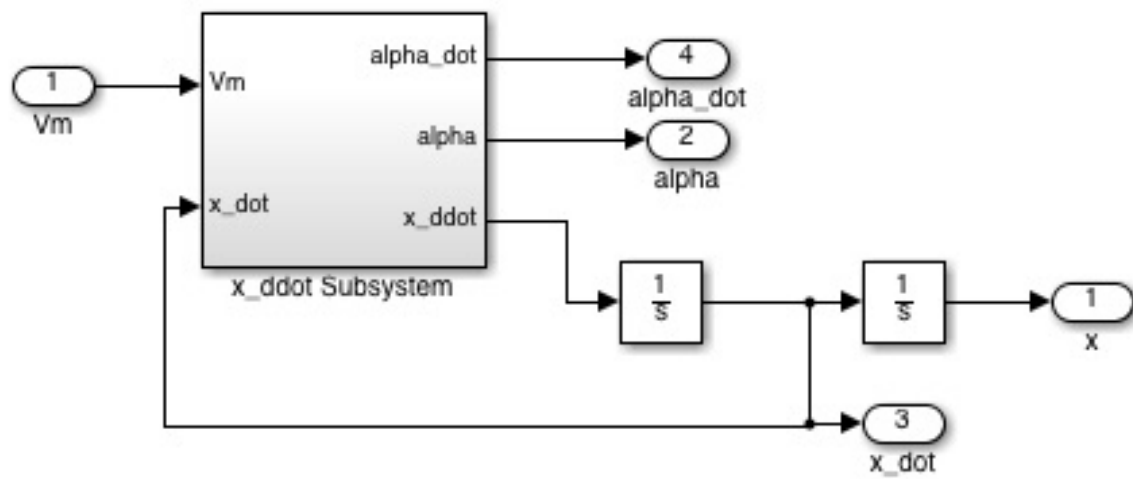


Figure B.2: SIP EOM Simulink subsystem used in the Simulink diagram given in B.1.

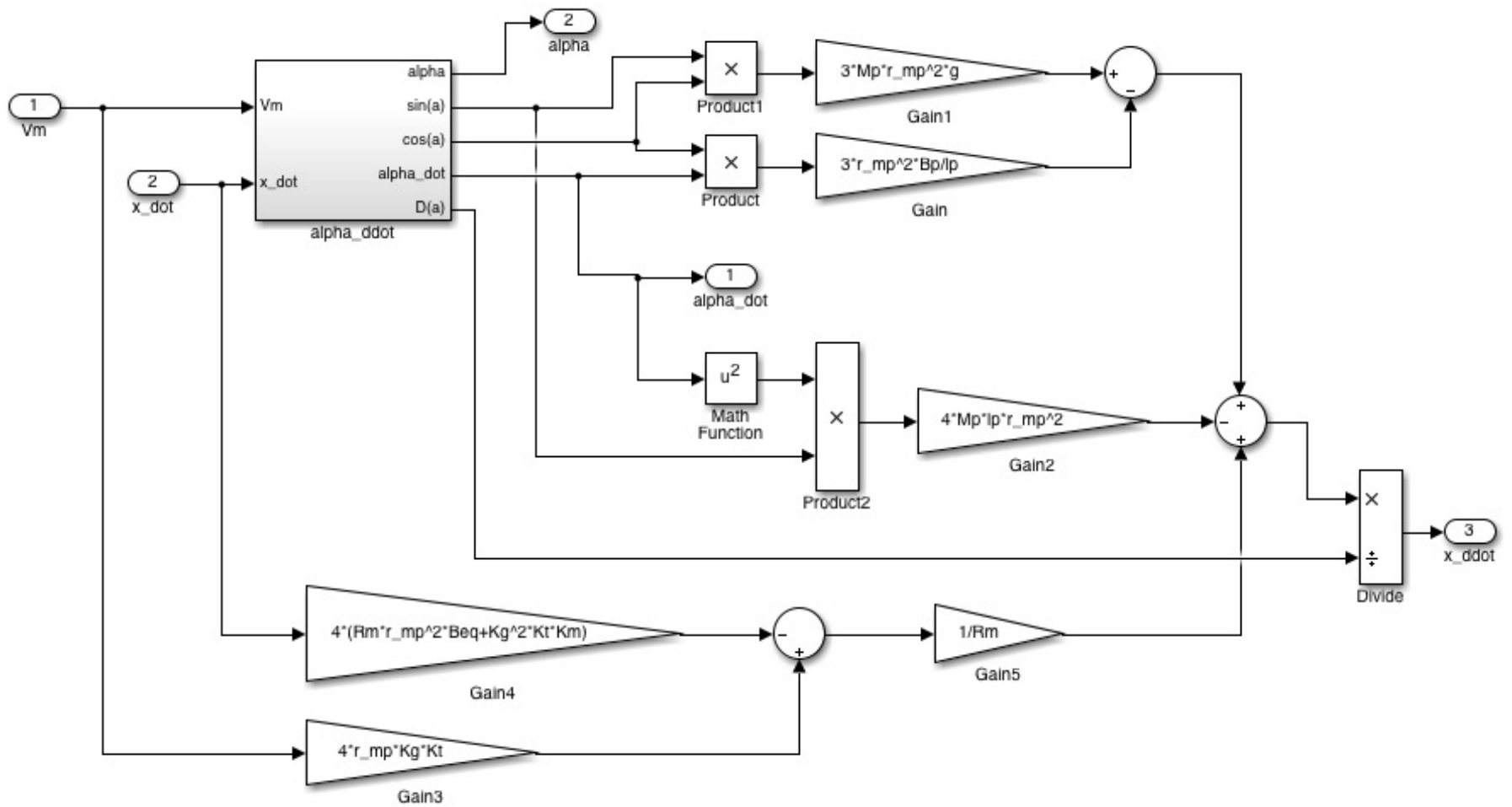


Figure B.3: \ddot{x} EOM subsystem used in the Simulink diagram given in B.2.

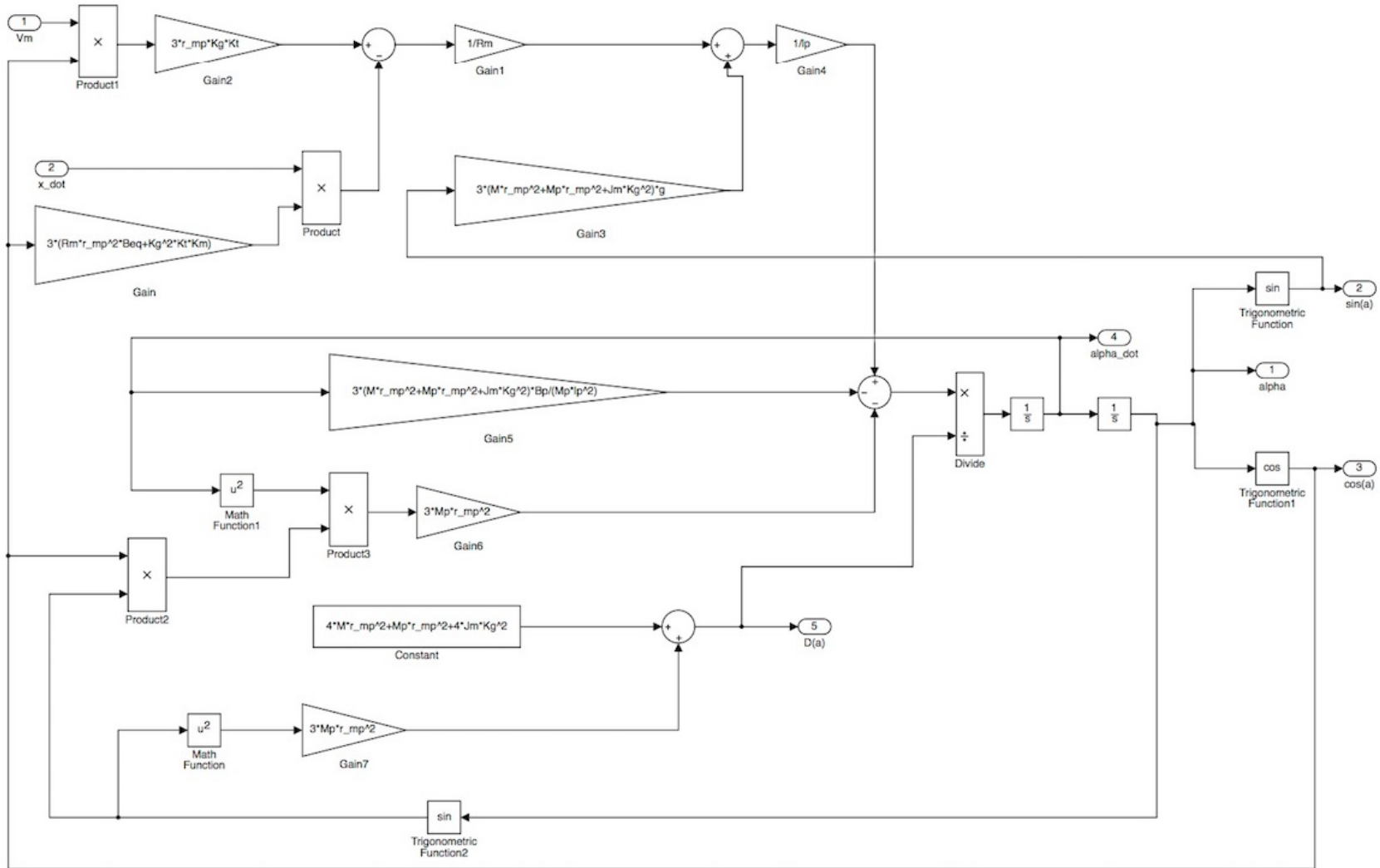


Figure B.4: α_{ddot} EOM subsystem used in the Simulink diagram given in B.3.

B.3 Simulink Diagrams for Stabilization Simulation

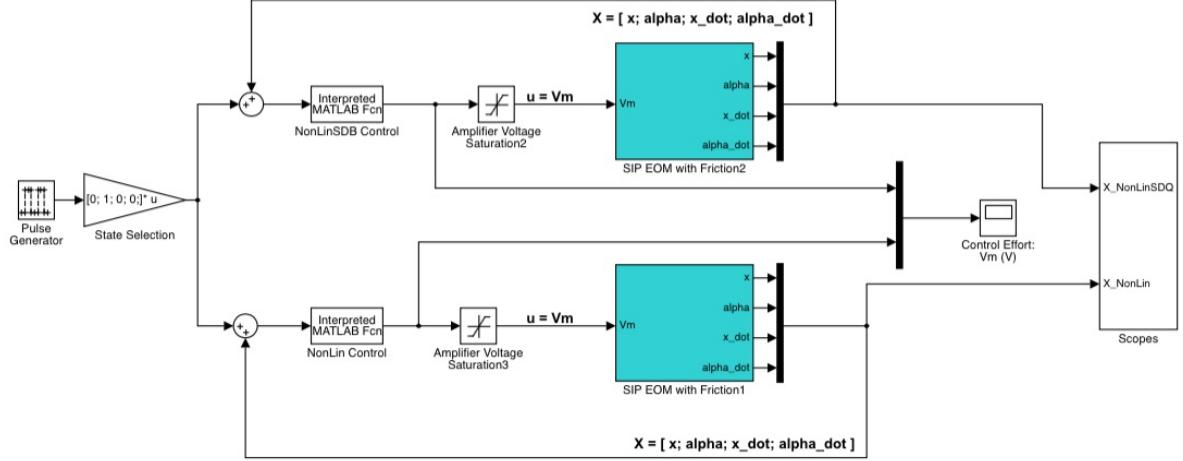


Figure B.5: Main Simulink diagram used for stabilization simulation to compare the performance of the control laws given by (3.24) and (3.32). The stabilizing control is computed inside a Matlab function with the command $-inv(R) * BX(u(1), u(2), u(3), u(4))' * (P * u + inv(A0' - P * B * inv(R) * B') * (0.5 * P * B2(u(1), u(2), u(3), u(4)) * inv(R) * B' * P * u + 0.5 * P * B * inv(R) * B2(u(1), u(2), u(3), u(4))' * P * u - P * f3(u(1), u(2), u(3), u(4))))$ (state-dependent B) or $-inv(R) * B' * P * u + inv(R) * B' * inv(A0' - P * B * inv(R) * B') * P * f3(u(1), u(2), u(3), u(4))$ (constant B). The input, u , for the block is the state vector, X . The SIP EOM with Friction subsystem computes the simulated state response based on the nonlinear equations of motion with friction given by equations (2.33) and (2.34). The details of the subsystem are given in Figures B.2-B.4

SIP System Simulation: Power Series Vs. LQR

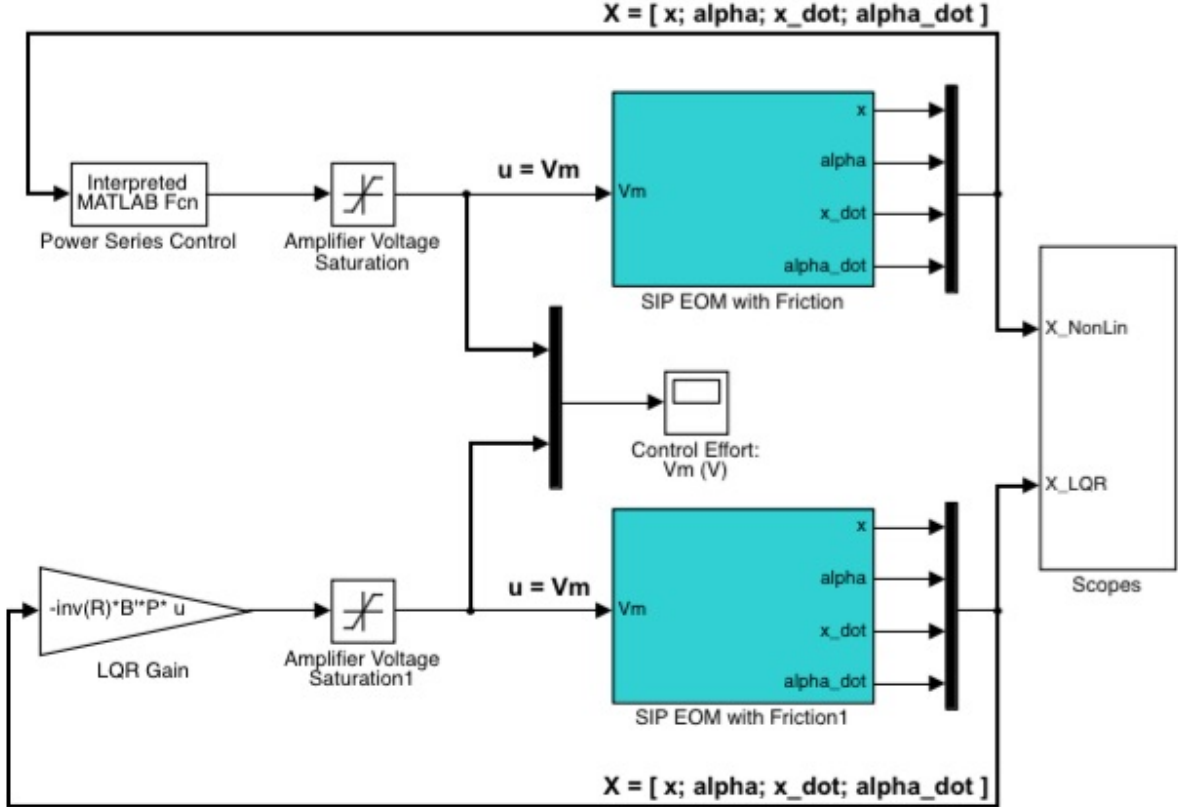


Figure B.6: Main Simulink diagram used for stabilization simulation. The stabilizing control is computed inside a Matlab function with the command $-inv(R)*B'*P*u + inv(R)*B'*inv(A0' - P*B*inv(R)*B')*P*f3(u(1), u(2), u(3), u(4))$ (constant Q) or $-inv(R)*B0'*P*u + inv(R)*B'*inv(A0' - P*B*inv(R)*B')*(P*f3(u(1), u(2), u(3), u(4)) + 0.5*[5*u(1)^2, 0, 0, 0; 0, 2*u(2)^2, 0, 0; 0, 0, u(3)^2, 0; 0, 0, 0, u(4)^2]*u)$ (state-dependent Q). The input, u , for the block is the state vector, X . The SIP EOM with Friction subsystem computes the simulated state response based on the nonlinear equations of motion with friction given by equations (2.33) and (2.34). The details of the subsystem are given in Figures B.2-B.4

B.4 Simulink Diagrams and Code for Stabilizing Control

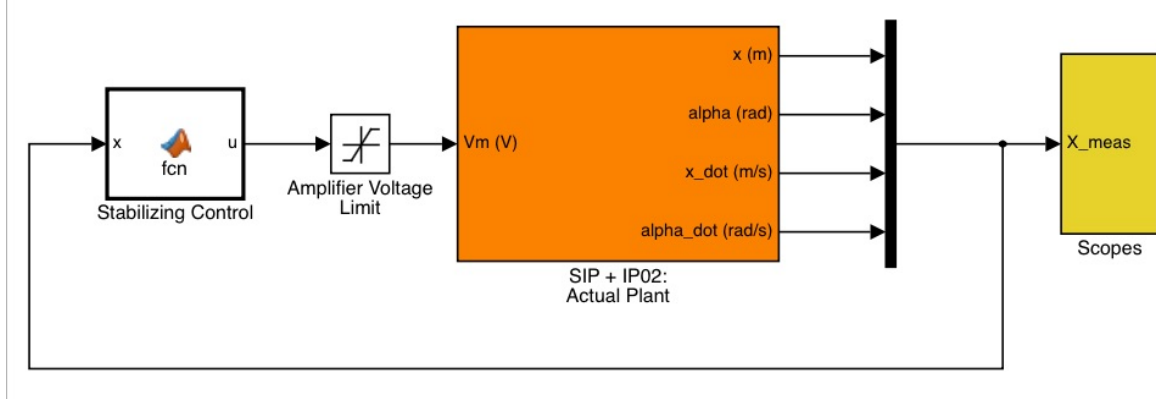


Figure B.7: Main Simulink diagram to run real-time stabilization. The SIP + IP02: Actual Plant block that communicates with the apparatus was provided by Quanser. The stabilizing control is computed inside an Embedded Matlab function block. The code inside the block is provided in Figures B.8 (constant Q) and B.9 (state-dependent Q).

```

function u = fcn(x,B,A0,P,R)
%%eml
Fn=zeros(4,1);

%Series Expansion Terms were computed outside of the program
Fn(3)=x(2)^2*(1.7737256624360185237606321648345*x(3) ...
+ 0.0031463131798169911765783738170848*x(4));
Fn(4)=x(2)^2*(17.231734651743796048251210107947*x(3) ...
+ 0.01262194848103311701018254482729*x(4));

%Balancing Control with Constant Q
u=-inv(R)*B'*P*x+inv(R)*B'*inv(A0'-P*B*inv(R)*B')*P*Fn;

```

Figure B.8: Code inside Embedded Matlab function block in the Simulink diagram to compute stabilizing control with constant Q based on power series expansion.

```

function u = fcn(x,B,A0,P,R)
%%eml
Fn=zeros(4,1);

%Series Expansion Terms were computed outside of the program
Fn(3)=x(2)^2*(1.7737256624360185237606321648345*x(3) ...
+ 0.0031463131798169911765783738170848*x(4));
Fn(4)=x(2)^2*(17.231734651743796048251210107947*x(3) ...
+ 0.01262194848103311701018254482729*x(4));

%Balancing Control with State-Dependent Q
u=-inv(R)*B'*P*x+inv(R)*B'*inv(A0'-P*B*inv(R)*B')*(P*Fn+0.5*...
[5*x(1)^2,0,0,0;0,2*x(2)^2,0,0;0,0,x(3)^2,0;0,0,0,x(4)^2]*x);

```

Figure B.9: Code inside Embedded Matlab function block in the Simulink diagram to compute stabilizing control with state-dependent Q based on power series expansion.

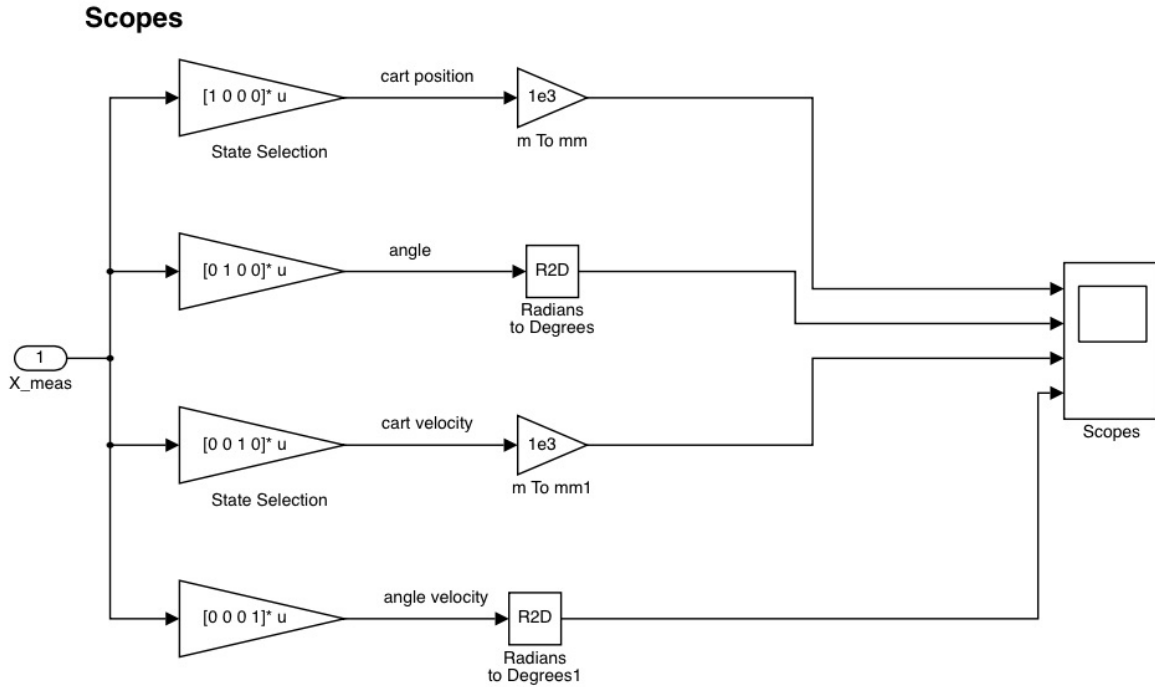


Figure B.10: Scopes subsystem to record and plot states.

B.5 Simulink Diagrams for Swing-up Control

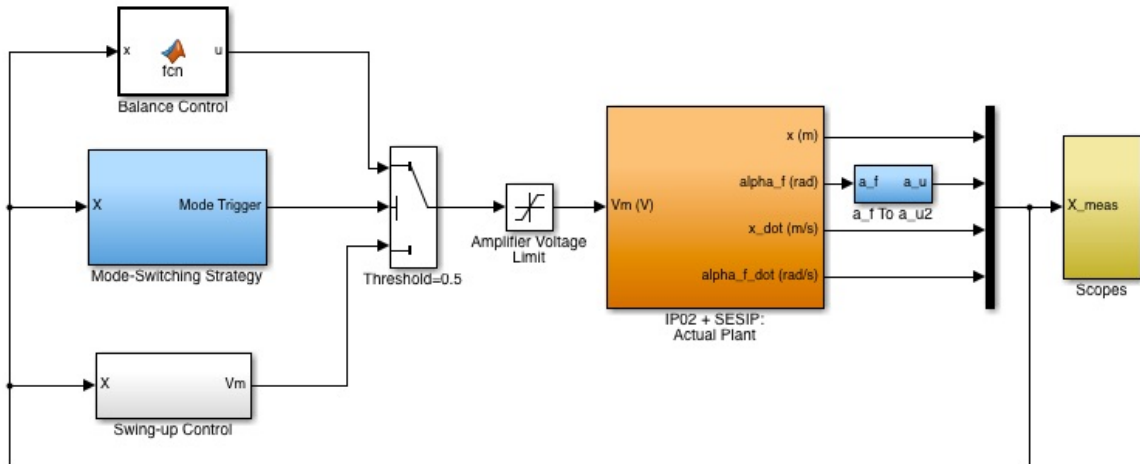


Figure B.11: Main Simulink diagram to run real-time swing-up. The SIP + IP02: Actual Plant block that communicates with the apparatus was provided by Quanser. The Mode Switching Strategy block that checks the angle of the pendulum and switches from the swing-up controller to the stabilizing controller, was also provided by Quanser. The details of the Swing-up Control subsystem block are given in Figure B.12 for the controller in (4.17), Figure B.15 for the controller in (4.28), and Figure B.16 for the controller in (4.42)

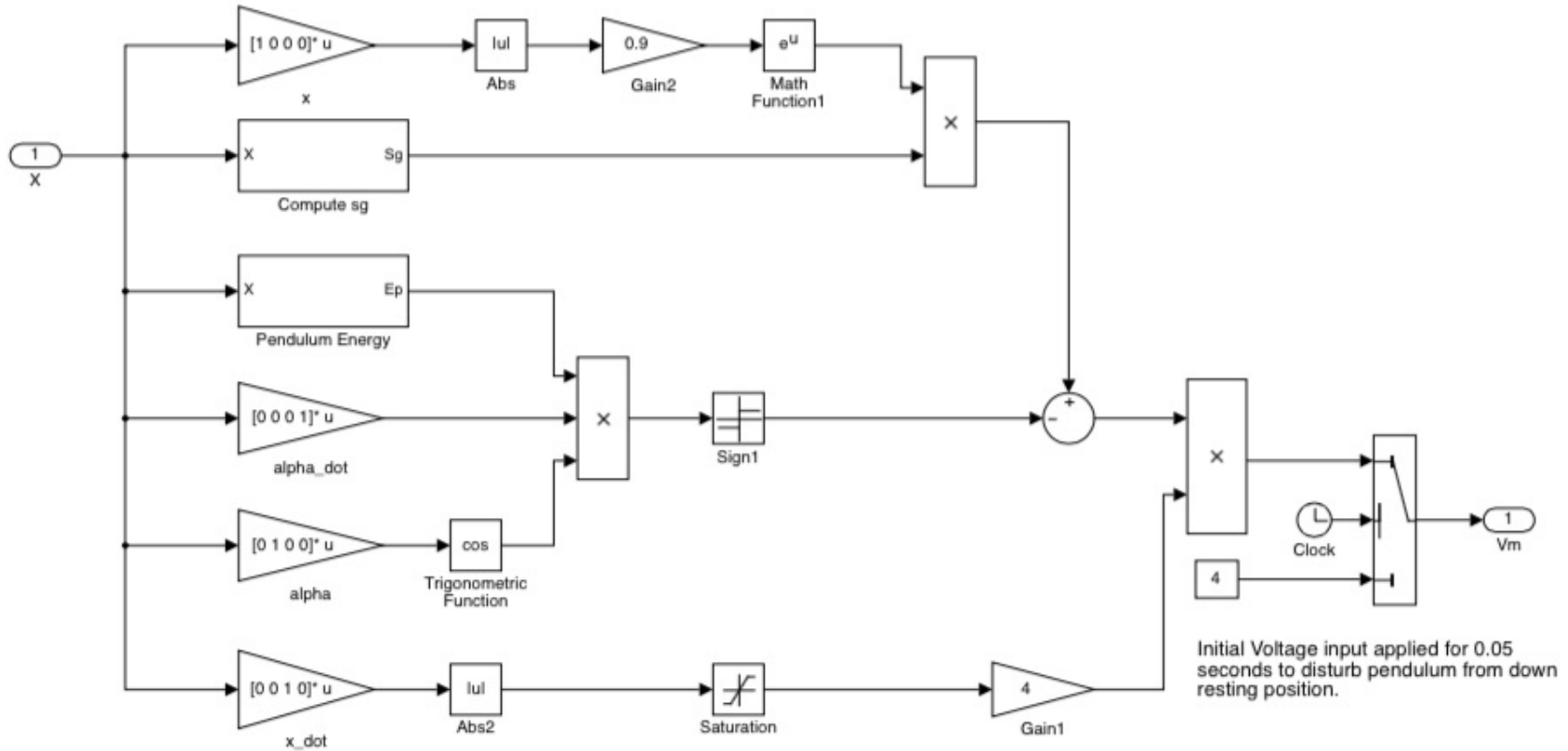


Figure B.12: Simulink subsystem used to compute energy based swing-up controller in (4.17). The details of the Compute sg subsystem block are given in Figure B.13, and the details of the Pendulum Energy subsystem block are given in Figure B.14.

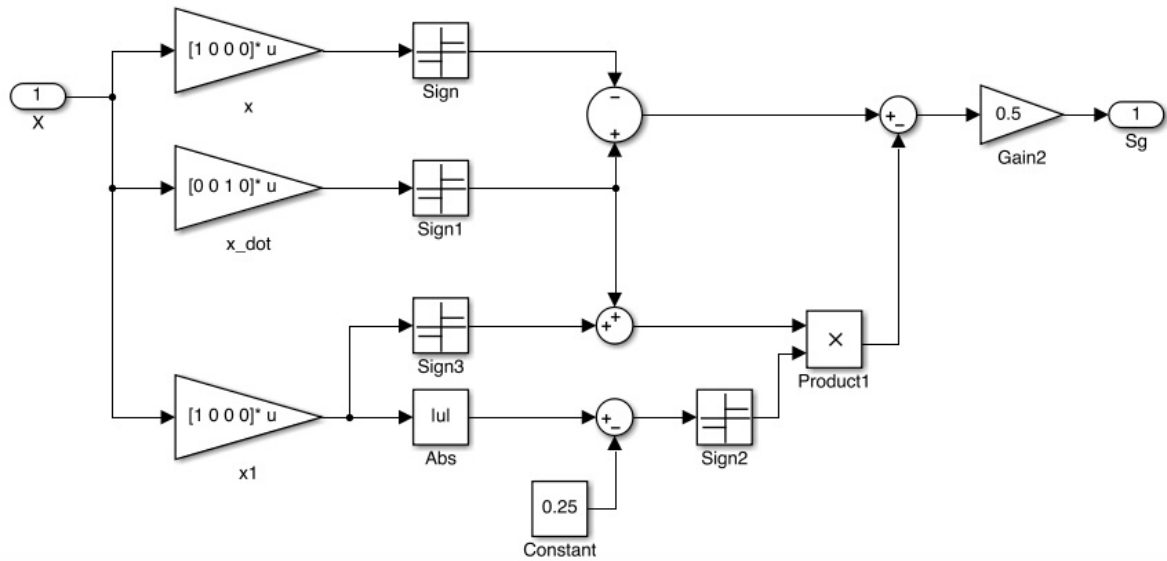


Figure B.13: Simulink subsystem that computes sg.

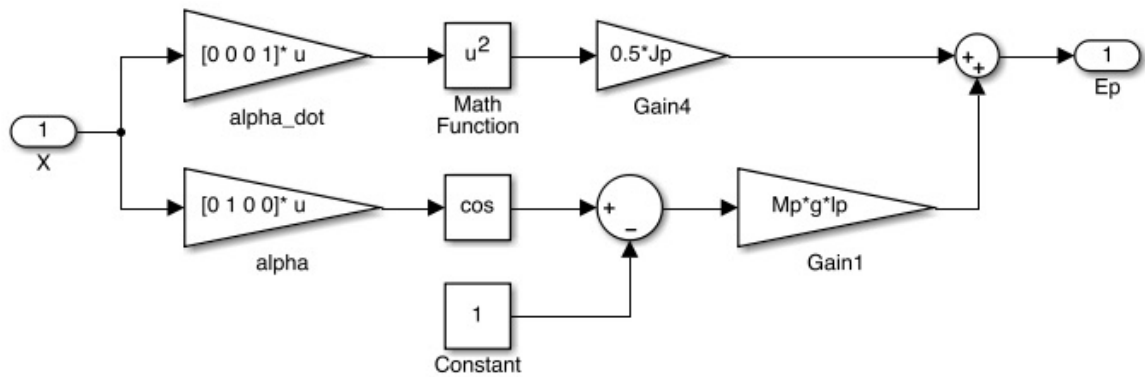


Figure B.14: Simulink subsystem that computes the pendulum's energy.

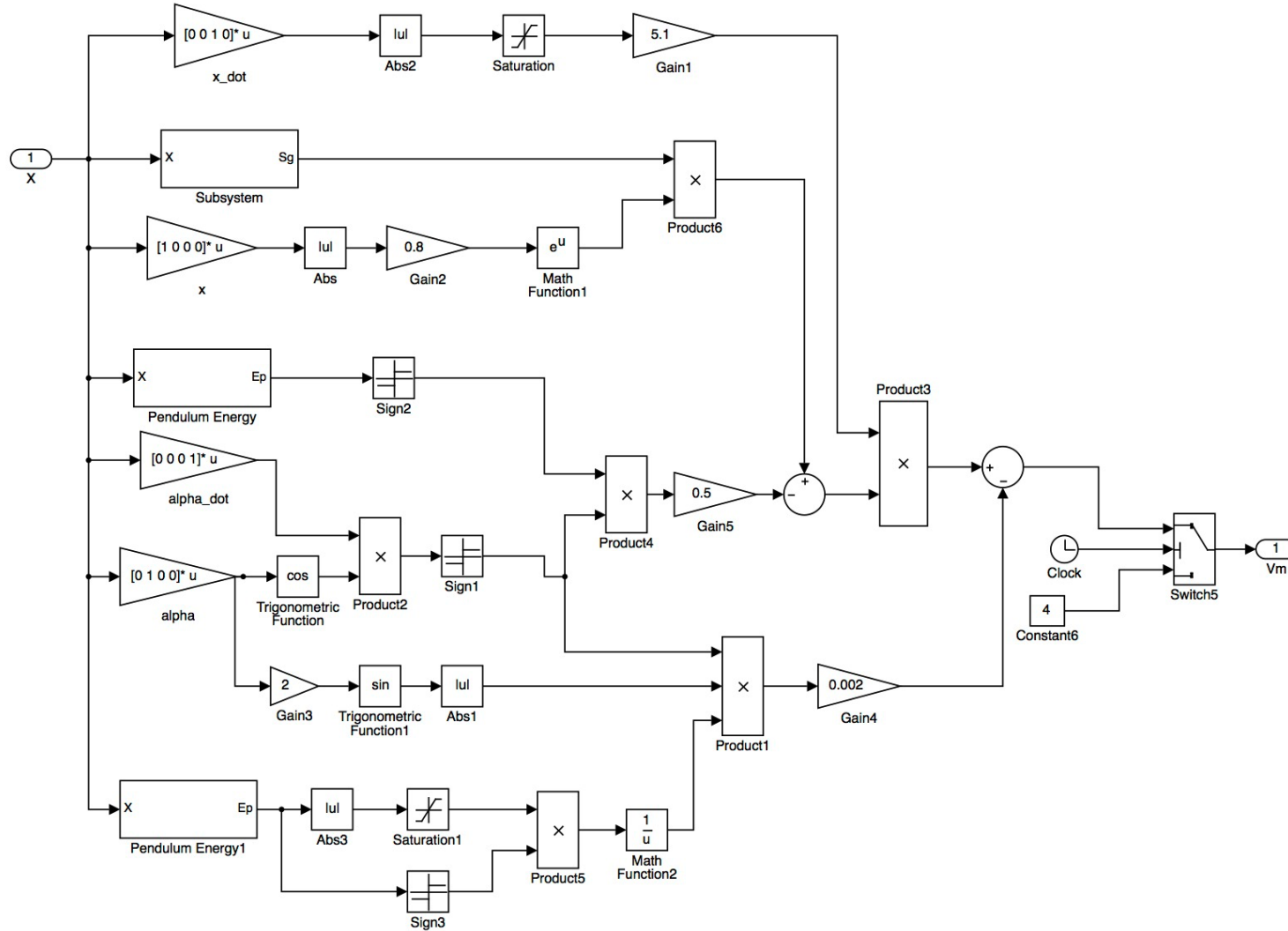


Figure B.15: Simulink subsystem used to compute more robust swing-up controller in (4.28). The details of the Compute sg subsystem block are given in Figure B.13, and the details of the Pendulum Energy subsystem block are given in Figure B.14.

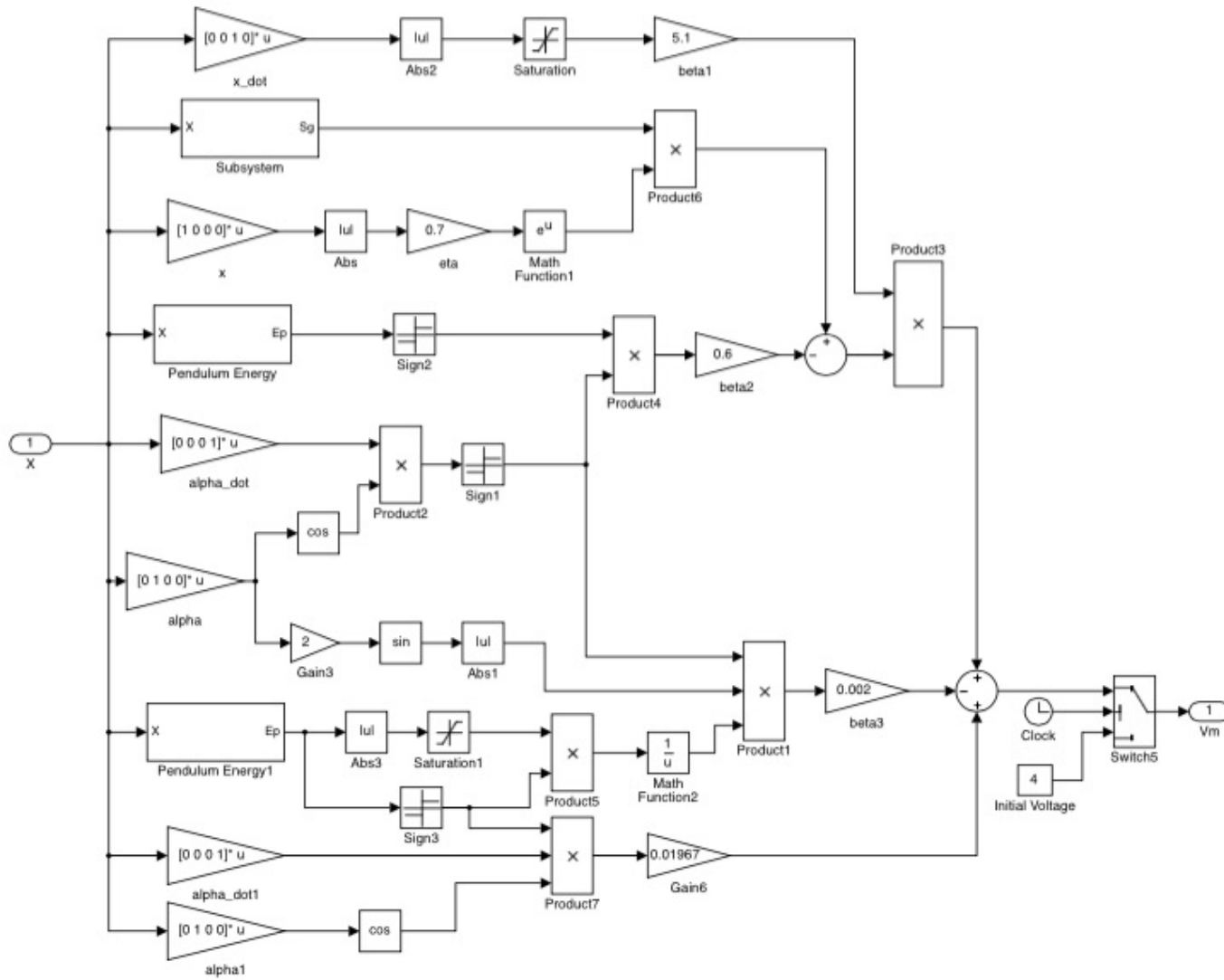


Figure B.16: Simulink subsystem used to compute swing-up controller with viscous damping term in (4.42). The details of the Compute sg subsystem block are given in Figure B.13, and the details of the Pendulum Energy subsystem block are given in Figure B.14.